



University of
Stavanger

Faculty of Science and Technology

MASTER'S THESIS

Study program/ Specialization: Structures and Materials	Spring semester, 2010 Open
Writer: Knut Inge Edvardsen (Writer's signature)
Faculty supervisors: Professor Jasna Bogunovic Jakobsen Professor Jonas Thor Snaebjornsson	
Title of thesis: Numerical analysis of vortex shedding	
Credits (ECTS):	
Key words: Vortex shedding Aeroelasticity Turbulence Computational Fluid Dynamics Fluid Structure Interaction	Pages: 74 + enclosure: 46 Stavanger, 14.06.2010

Abstract

This report deals with structural vibrations of wind exposed structures caused by the vortex shedding phenomena. The theory of vortex shedding and the field of study called aeroelasticity are presented.

A case study of a light mast structure has been used as a study of the vortex shedding phenomena. Numerical simulations of vortex shedding have been performed through the use of Computational Fluid Dynamics (CFD). The aerodynamic flow around an U-section susceptible to vortex-induced vibrations has been evaluated. Three different aerodynamic suppression devices for vortex-induced vibrations have been presented and discussed.

An attempt was also made to perform Fluid-Structure Interaction (FSI) analysis. But as computational stability problems were encountered, these attempts were not successful.

Acknowledgements

This report was made under the supervision of Professor Jasna Bogunovic Jakobsen and Professor Jonas Thor Snaebjornsson at the University of Stavanger. Their help and advices throughout the master's thesis period have been very valuable and enlightening.

The interest and contribution from Mikael Pålsson and Henning Oppedal at Aibel have also been very important. A special thanks is sent to Abaqus-expert Mikael for his support and guidance during the Abaqus analyses.

I would also like to thank Jan Granlund at Abaqus Scandinavia for providing me with the license of Abaqus 6.10 Pre-release.

Finally, I want to thank my wife Marit and my son Olav for the valuable vortex shedding conversations during the last months.

Contents

1	Introduction	5
2	Vortex Induced Vibrations	6
2.1	The vortex-shedding phenomena	6
2.2	Aeroelasticity	7
2.3	Eurocode 1 - Part 1-4 - Wind actions	11
2.4	Countermeasures	12
3	Case study of a light supporting mast at Reykjavik Airport	14
4	Modal analysis	16
4.1	General	16
4.2	Models	16
4.3	Conclusion	22
5	Computational Fluid Dynamics	23
5.1	General	23
5.2	Governing equations	23
5.3	Numerical calculation methods used in CFD	28
5.4	Turbulence	29
5.5	Errors and uncertainty in CFD modelling	30
6	CFD Model	34
6.1	Software	34
6.2	Modelling	34
6.3	Post-processing in Abaqus and Matlab	38
6.4	Z-direction meshing	40
6.5	Boundary layer meshing	45
7	CFD Results	51
7.1	CFD model of original U-section	51
7.2	CFD model of U-section with installed countermeasure	54
7.3	Alternative No.1 - Flat plate flap	58
7.4	Alternative No.2 - Square flap	62

8 Fluid Structure Interaction	65
8.1 General	65
8.2 FSI modelling	65
8.3 FSI analysis failure	67
8.4 Conclusion	67
9 Conclusions	68
Bibliography	70
List of Figures	72
List of Tables	74
A Plots - U-section model	75
B Plots - Installed countermeasure model	80
C Plots - Flat plate model	86
D Plots - Square flap model	92
E Matlab program	97
F Drawings	112

Chapter 1

Introduction

Vortex-induced vibrations (VIV) is a wind-structure interaction phenomena often encountered in slender structures exposed to wind. In this report, vortex-induced vibrations caused by wind is the main topic of concern, and a case study of vortex shedding using Computational Fluid Dynamics (CFD) is done.

A light mast at the airport of Reykjavik has been used as a case study in this report. Violent vortex-induced vibrations were observed at the light mast after installation. The light mast was later equipped with aerodynamic devices to prevent the vibrations. Measurements were taken both before and after the devices were installed. The available measurements have been used for a comparison to the results found by computer analysis.

The analyses presented in this report consist of a modal analysis of the light mast structure, a CFD model of the original light mast cross-section, a CFD model of the light mast cross-section with the installed devices and CFD models of two alternative VIV countermeasuring devices. Finally, the Fluid-Structure Interaction (FSI) capabilities of Abaqus 6.10 (Pre-release) have been investigated and reported.

Chapter 2

Vortex Induced Vibrations

2.1 The vortex-shedding phenomena

Vortex induced vibrations (VIV) occur when vortices are shed from alternating sides of a body. The process can be recognized by the characteristic vortex trail also known as the von Kármán vortex street, named after the engineer and fluid dynamicist, Theodore von Kármán. The effect can be observed in different scales and mediums, from microscopical to galactical.

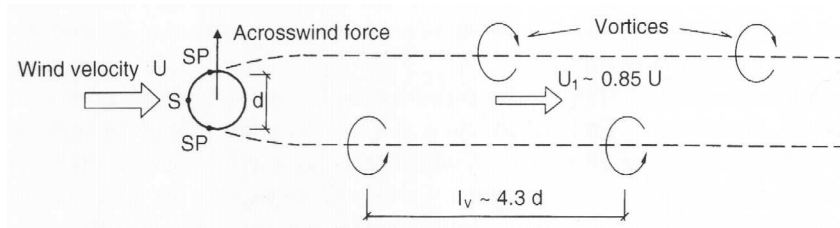


Figure 2.1: The vortex street behind a cylinder [Dyrbye and Hansen, 1999].

The vibrations generated by vortex shedding usually occur in slender structures with low damping. The vibrations occur if the vortex shedding frequency coincide with or come close to the natural frequency of the structure. The vortex shedding frequency f_s of a non-vibrating body can be derived from figure 2.1. The time between the vortices at each side is equal to the distance l_v divided by the velocity of the vortices, U_1 . The frequency is the inverse of the period, giving that $f_s = U_1/l_v$. The distance between the vortices, l_v , must be proportional to the structure width d , since this is the only relevant length. The proportionality factor between U_1/l_v and U/d is called the Strouhal number S_t . The vortex shedding frequency can thereby be written

$$f_s = S_t \frac{U}{d} \quad (2.1)$$

The Strouhal number is mostly dependent on the shape of the cross section and the Reynolds number. The Reynolds number is defined as the ratio between the inertial and the frictional forces and is written

$$Re = \frac{Ud}{\nu} \quad (2.2)$$

where ν is the kinematic viscosity.

For circular cross section, the Reynolds number is the most important parameter together with surface roughness, while for sharp-edged cross sections, the cross section shape is the most important. The Strouhal number is also dependent on turbulence and aeroelasticity.

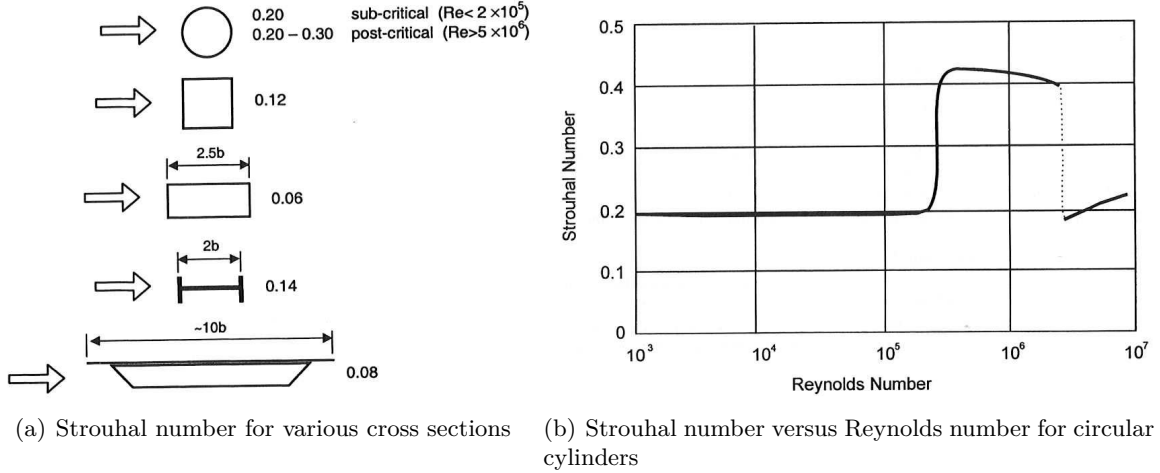


Figure 2.2: The variation of the Strouhal number for various cross sections and Reynolds numbers [Holmes, 2001].

In addition to the force variations seen in the cross flow direction at frequency f_s , vortex shedding also induces force variations in the in-line force with a frequency of $2f_s$. The variation in the in-line direction is less intense than the cross flow variation, but may also cause vibrations.

Resonance between structure and the vortex induced force will occur if the frequency of the loading, f_s is equal or close to the natural frequency of the structure, f_e . If $f_e = f_s$ is inserted in equation (2.1), and the equation is solved for the wind speed U , the critical wind speed for the mode frequency inserted is found.

$$U_{crit} = \frac{1}{S_t} f_e d \quad (2.3)$$

2.2 Aeroelasticity

2.2.1 General

Aeroelasticity is the name of the discipline concerning the interaction between the aerodynamic forces and the structural motions. In terms of general fluids the topic is also referred to as the study of Fluid-Structure Interaction (FSI).

2.2.2 Lock-in

When the wind speed is sufficiently close to U_{crit} , the structure will start to oscillate. A phenomena called lock-in occurs when the wind speed is in the the critical wind speed region.

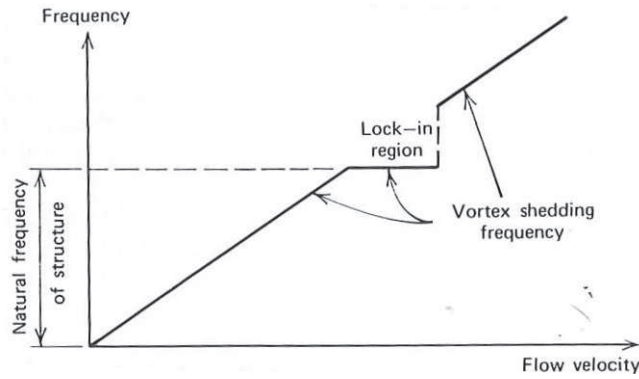


Figure 2.3: Evolution of vortex-shedding frequency with wind velocity over an elastic structure [Simiu and Scanlan, 1996].

The vortex shedding frequency locks on to the structural frequency in a region of wind speeds, and not only at the exact U_{crit} . This is due to the interaction between the structural motion and the wind. Figure 2.3 shows how the vortex-shedding frequency is constant in the lock-in region.

2.2.3 Correlation length

The aeroelasticity also causes the loading on the structure to be imperfectly correlated along the structure span. Experiments have shown that the correlation length is varying according to the motion amplitude. As shown in figure 2.4, the loading across the span is correlated for a longer distance if the amplitude is bigger.

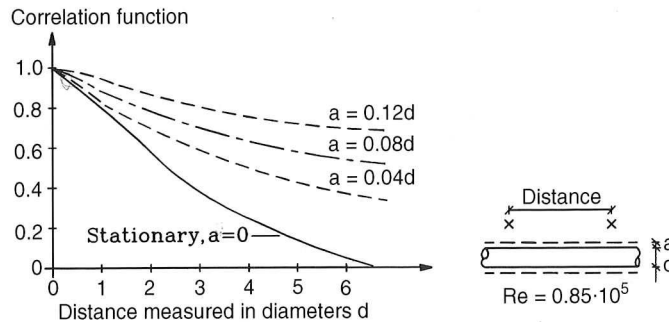


Figure 2.4: Influence of the amplitude of motion upon the correlation length [Dyrbye and Hansen, 1999].

2.2.4 Frequency bandwidth

Because of turbulence the vortex shedding frequency of a structure exposed to wind is varying over a band of frequencies, and not just at the exact frequency expected from eq. 2.3. When having a range of vortex shedding frequencies, the response spectrum is said to be broad

banded. When having only one or a small range of frequencies the response is said to be narrow banded.

A broadbanded response can also be induced by e.g. varying section geometry and devices causing irregular vortex shedding.

The frequency bandwidth is a common avoidance criteria for vortex shedding as e.g. “the Oppen criteria” which is much used by Statoil at the Norwegian shelf. [Oppen, 1995] When having a broadbanded response, the fluctuating force will vary randomly along the length of the beam and the probability of violent vibrations will be reduced.

2.2.5 Aeroelasticity equation of motion

The equation of motion of a single-DOF across-flow motion can be written [Simiu and Scanlan, 1996]:

$$m\ddot{y} + c\dot{y} + ky = F(y, \dot{y}, \ddot{y}, t) \quad (2.4)$$

where y is the deflection in the across flow direction, and F is the loading on the structure.

This loading can generally be classified in three classes [Dyrbye and Hansen, 1999]:

- Net gust load caused by lateral wind fluctuations, F_t
- Loads caused by vortex shedding, F_v
- Motion-induced forces, F_m . The most important motion induced force is the negative aerodynamic damping.

The motion induced force, F_m , of the loading, can in it’s most simple form be written [Dyrbye and Hansen, 1999]

$$F_m = -h_a\ddot{y} - c_a\dot{y} \quad (2.5)$$

where h_a is the added mass of air and c_a is the aerodynamic damping. For most structures the added mass of air is small relative to the structural mass and may be disregarded.

The linear model in equation 2.5 is accurat for small vibration amplitudes of up to 10-20% of the structural width [Dyrbye and Hansen, 1999]. For large vibration amplitudes the aerodynamic damping becomes non-linear. A model for nonlinear aerodynamic damping force can be found in Vickery and Basu [1983], but this will not be further presented.

2.2.6 Aerodynamic damping

The aerodynamic damping may be characterized by a dimensionless parameter S_a [Dyrbye and Hansen, 1999].

$$S_a = \frac{2\delta_a m_e}{\rho d^2} \quad (2.6)$$

where δ_a is the logarithmic decrement of damping, ρ is the fluid density, d is the relevant dimension and m_e is the equivalent mass per unit length of the structure for the mode considered. This is defined as

$$m_e = \frac{\int_0^L m(x)(\xi(x))^2 dx}{\int_0^L (\xi(x))^2 dx} \quad (2.7)$$

where $\xi(x)$ is the mode shape.

The aerodynamic parameter S_a is negative for negative aerodynamic damping. It is the negative aerodynamic damping that leads to significant vortex-induced vibrations. The aerodynamic damping is strongly related to the turbulence intensity. When the flow is turbulent, the risk of negative aerodynamic damping is reduced, as seen in figure 2.5.

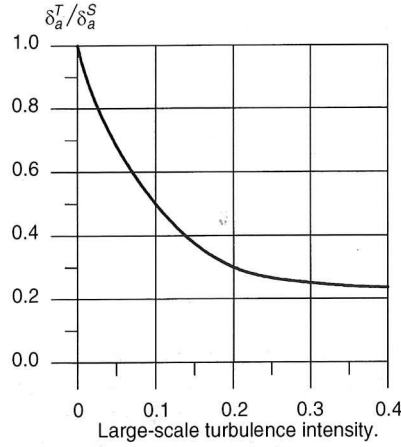


Figure 2.5: The ratio between the aerodynamic damping in turbulent flow, δ_a^T , and smooth flow, δ_a^S , as a function of the large-scale turbulence intensity for a circular cylinder [Dyrbye and Hansen, 1999]

2.2.7 Scruton number

The Scruton number is a parameter combining the structural damping and the equivalent mass of the structure m_e . It is often referred to as a stability parameter. The Scruton number is defined as [Dyrbye and Hansen, 1999]:

$$S_c = \frac{2\delta_s m_e}{\rho d^2} \quad (2.8)$$

The effective damping is proportional to the sum between the Scruton number S_c and the aerodynamical damping S_a . The risk of violent vortex-induced vibration depends on these two parameters in combination [Dyrbye and Hansen, 1999]. The aerodynamic damping is dependent on the turbulence intensity, so the risk of VIV can therefore be evaluated in a risk grid based on a combination of turbulence intensity and Scruton number as shown in figure 2.6.

Experience shows that there is no risk of lock-in if $S_c > 20$. For $S_c < 10$ the risk of lock-in is very high [Dyrbye and Hansen, 1999]. In the lock-in region, the structure oscillates with an amplitude of some fractions of the across-wind dimensions of the body. The maximum of

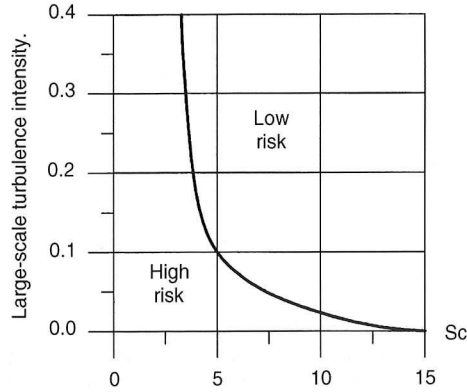


Figure 2.6: The risk of violent vortex-induced vibrations increases with low turbulence intensity and low Scruton numbers [Dyrbye and Hansen, 1999].

the oscillation is rarely exceeding half the across-wind dimension [Simiu and Scanlan, 1996]. Vortex shedding is therefore not causing immediate breakdown of structures, but is mainly a fatigue and serviceability problem. The self-limiting behaviour of the amplitude can be explained by the variation in the negative aerodynamic damping. At small amplitudes the negative aerodynamic damping is large, while at large amplitudes the aerodynamic damping is small. The maximum amplitude of the across-flow oscillation is therefore mostly dependent on the Scruton number, since the negative aerodynamic damping is not significantly contributing to the force on the structure at large amplitudes.

2.3 Eurocode 1 - Part 1-4 - Wind actions

Eurocode 1 - Part 1-4 annex E provides rules for “Vortex shedding and aeroelastic instabilities”. This is a summary of the rules stated there.

The effect of vortex shedding need not to be investigated if $V_{crit,i} > 1.25 \cdot V_m$, where $V_{crit,i}$ is the critical wind velocity as defined in equation 2.3, and V_m is the characteristic 10 minutes mean wind velocity.

The across wind force is given by the expression:

$$F_w(s) = m(s) \cdot (2 \cdot \pi \cdot n_{i,y})^2 \cdot \Phi_{i,y}(s) \cdot y_{F,max} \quad (2.9)$$

- $m(s)$ is the vibrating mass of the structure per unit length
- $n_{i,y}$ is the natural frequency
- $\Phi_{i,y}(s)$ is the mode shape of the structure normalised to 1 at the point with the maximum displacement
- $y_{F,max}$ is the maximum displacement over time of the point with $\Phi_{i,y}(s)$ equal to 1.

The maximum displacement, $y_{F,max}$, can be calculated using two different approaches. The first approach [Eurocode-1, 2005, E.1.5.2] is the most general, and can be used for various kinds of structures and mode shapes. The second approach [Eurocode-1, 2005, E.1.5.3] may be used for cantilevered structures in its first mode, and is typically for chimneys and masts. As the second approach is rather complex and non-informative, only the first will be presented. The first approach gives the following expression for the maximum relative displacement:

$$\frac{y_{F,max}}{b} = \frac{1}{St^2} \cdot \frac{1}{Sc} \cdot K \cdot K_w \cdot c_{lat} \quad (2.10)$$

- b is the reference width of the cross section
- St is the Strouhal number
- Sc is the Scruton number
- K_w is the effective correlation length given in [Eurocode-1, 2005, E.1.5.4]
- K is the mode shape factor given in [Eurocode-1, 2005, E.1.5.2.5]
- c_{lat} is the lateral force coefficient given in [Eurocode-1, 2005, Table E.2]

2.4 Countermeasures

2.4.1 Aerodynamic countermeasures

The essence of aerodynamic countermeasures is to modify the airflow around the object to avoid rhythmic formation of vortices.

The most common method used for slender circular structures is helical strakes. The helical strakes consist typically of three strakes wrapped around a cylinder as shown in figure 2.7a. For a chimney, the helical strakes are installed on the top third part. This is where the load is most influential. A typical configuration for helical strakes are one revolution in three diameters, and a strake width of 10% of the chimney diameter. The strakes increase drag in the wind direction by a factor of approximately 1.4 [Dyrbye and Hansen, 1999]. The purpose of the strakes is to make the vortices shed non-rhythmic along the chimney and to disturb the span-wise correlation.

Vortex suppressing devices can also be designed to streamline the body as shown in figure 2.7d and 2.7g. If separation from the body can be minimized, vortex shedding will be minimized and drag will be reduced [Blevins, 1990, p.78]. It is important that the streamlining devices are free to pivot to account for all wind directions.

Other devices, like the ones at figure 2.7b and 2.7c have the objective to disrupt the vortex formation by introducing bleeding of air through perforations.

By introducing splitter plates, as shown in figure 2.7e the periodic vortex shedding is halted or at least significantly reduced.

A thorough evaluation of various aerodynamic VIV suppressing devices can be found in [Zdravkovich, 1981] or [Blevins, 1990].

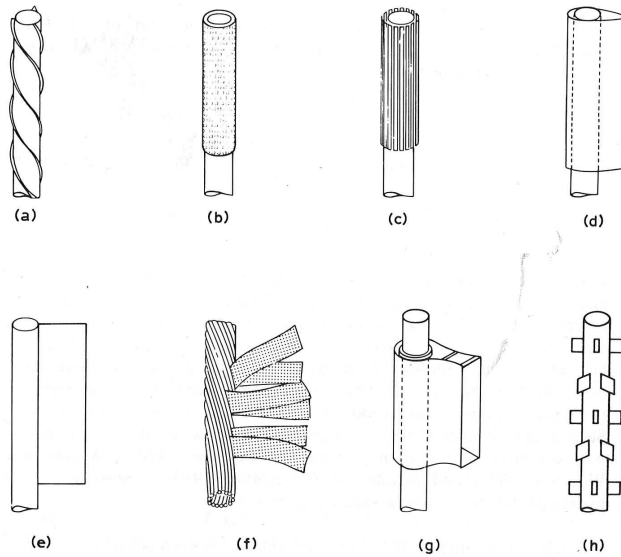


Figure 2.7: Add on devices for suppression of vortex-induced vibration of cylinders: (a) helical strike; (b) shroud; (c) axial slats; (d) streamlined fairing; (e) splitter; (f) ribbed cable; (g) pivoted guiding vane; (h) spoiler plates [Blevins, 1990]

2.4.2 Mechanical countermeasures

Vortex-induced vibrations can also be countered by modifying the mechanics of the structural system. The object of this is to change the natural frequency of the structure. To modify the natural frequency, either the mass or the stiffness has to be changed.

For tall and slender structures like chimneys, oil platforms and buildings, tuned mass dampers are a frequently used way of modifying the mass. The mass is suspended in a spring-damper system at the top of the structure. The mass should be about 0.01- 0.02 times the total mass of the structure. The natural frequency of the suspended mass should be close to the natural frequency of the structure [Dyrbye and Hansen, 1999].

The structural stiffness of the system can be modified by stiffening or weakening the system. In most cases stiffening of the system is the only option of these two since the structure stiffness was a consequence of the relevant ultimate load cases. The best way is of course is to have vortex shedding in mind during design phase, and to make sure that the natural frequencies of the structure are far enough away from the relevant vortex shedding frequencies. If unwanted vibrations occur after a structure has been installed, it could be difficult and expensive to modify the structural stiffness.

Chapter 3

Case study of a light supporting mast at Reykjavik Airport

The structure that will be investigated is a frame type mast supporting flight control lamps for the approach control at Reykjavik Airport. The light mast was installed in the summer of 2005. Soon after installation, large across-wind oscillations was observed at the mast cantilever beam at certain wind conditions. The vibrations was considered to be unacceptable and it was decided to investigate the problem. A report was made from these investigations [Bessason and Snaebjörnsson, 2008].



Figure 3.1: The mast supporting flight control lamps. Large oscillations were observed at the cantilever beam shortly after installation [Bessason and Snaebjörnsson, 2008].

The investigation resulted in installation of an aerodynamic countermeasure to prevent the vibrations. The wind flaps, ref. figure 3.2 were installed as a test arrangement to observe the effect, but became permanent since they were so successful.

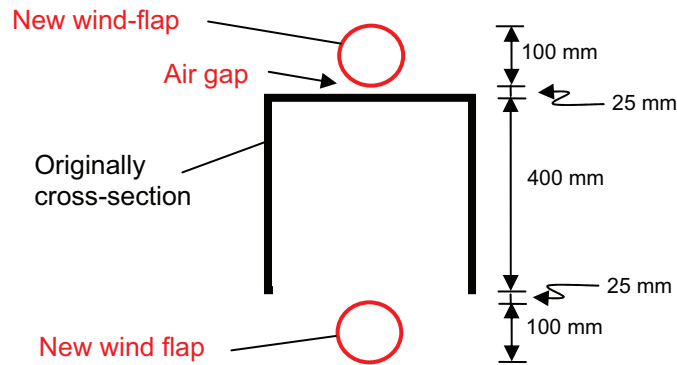


Figure 3.2: The light mast was equipped with pipes over and under the section [Bessason and Snaebjörnsson, 2008].



Figure 3.3: The light mast after the installation of flaps [Bessason and Snaebjörnsson, 2008].

Measurements were taken both before and after installation of countermeasures. Before installation the measurements showed that whenever wind speed reached 6-8 m/s the cantilever beam would start vibrating intensively. The maximum measured amplitude of motion during the measurements of the original structure was 6.43 cm.

The frequency of the cantilever vertical motion was measured to be 2.31 Hz, and the damping was estimated to be between 0.5% and 1% of critical.

After installation of countermeasures, new measurements were done. The new measurements showed that the vortex induced motion was reduced by 70%, and the maximum measured amplitude of motion after installation was less than 1.5cm. The added weight affected the response frequency and reduced it slightly to 2.2 Hz.

Chapter 4

Modal analysis

4.1 General

A modal analysis of the light mast has been performed in Abaqus [2010, v.6.10 Pre-Release]. The purpose of the modal analysis is to find the natural frequencies of the structure which subsequently will be used in the fluid-structure interaction analyses. A similar analysis of the light mast was previously performed by Bessason and Snaebjörnsson [2008]. The analyses in Abaqus is based on a dynamic formulation of the finite element method. Several different models have been evaluated using different element formulations and modelling techniques.

The light mast is a steel frame structure. The beams and columns of the light mast are made of welded 10mm plates. The columns of the light mast do not have an uniform cross section, but are increasing in width at the bottom of the column. The lamp supporting U-section has uniform cross section. Along the beam at the bottom part of the cross section the two webs are connected by 25mm diameter round bars, evenly spaced by a distance of 500mm . In addition to the structural elements, the structure is equipped with pipes for cabling and the flight control lamps it is supporting. The drawings of the structure can be found in appendix F).

A modal analysis has two important parameters, namely the stiffness and mass of the structure analysed. To get the correct modes and natural frequencies, these two parameters have to be modelled correctly. When considering the light mast structure, the 25mm bars at the lower part of the U-section is the challenging part of the structure to model. As it was uncertain how significant these bars were for the structural stiffness, several different modelling approaches have been evaluated.

4.2 Models

4.2.1 Model No.1 - Beam model with standard element formulation

The first model made was a typical beam element model of the structure. The columns of the structure were modelled as square hollow sections of 0.4m x 0.4m, and the lamp support beam as an open section (in Abaqus as “arbitrary section”) of 0.38m x 0.4m. The 25mm diameter bars was not included in this model. The extra mass of the lamps and fittings was included by increasing the material density by 10%. The mesh contained a total of 46

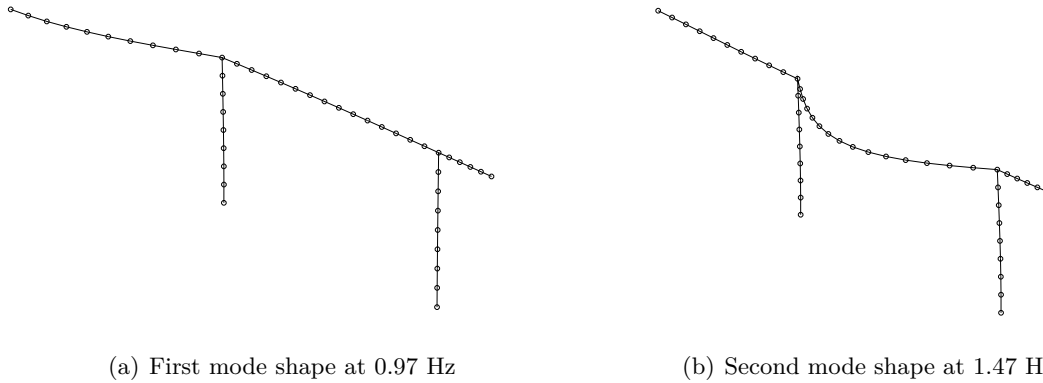


Figure 4.1: The first two mode shapes of the standard beam element model. The mode shapes shows uncontinous deformation.

element, meaning a length of 0.5-1m per element. The modelling and the mesh of this model were similar to the model by Bessason and Snaebjörnsson. The beam element formulation was the standard 6-DOF linear 2-node element in Abaqus (B31) and the structure had fixed boundary conditions at the two columns.

The output from this model gave unexpected and obviously erroneous results for the horizontal mode shapes. The deformation of the mode shapes was uncontinous, as shown in figure 4.1. At first it was belived to be due to an error in the analysis and all boundary conditions and input was checked. An identical model was also built up in Genie [2007, v3.5-20], but identical mode shapes were found there.

As all input seemed correct the focus was turned to the theory chapters of the Abaqus documentation [2010], and some answers were also found there. The problem with the uncontinous mode shapes seems to be due to the standard beam element formulation combined with an open section. For beams geometrically modelled as an open section using a regular beam element, the beam is assumed to be free to warp and the axial strain due to warping is neglected. The section will consequently have very little torsional stiffness [Abaqus documentation, 2010, B31 formulation]. The uncontinous modes are belived to be related to the minimal torsional stiffness the beam is given. Because of the issue with the uncontinous modes, the model based on the standard beam element could not be used and a new model was made.

4.2.2 Model No.2 - Beam model with open-section element formulation

The second model uses a special open-section element formulation (B31OS) provided by Abaqus. The open-section element in Abaqus has seven degrees of freedom, compared to six for the standard beam element. The warping is the additional degree of freedom. The geometry, boundary conditions and element meshing of this model was just as for model No.1, meaning that the stiffness provided by the 25mm bars neither is accounted for here. The section is therefore free to warp, which obviously would at least partially be prevented by the bars. The results from the analysis are shown in table 4.1.

Mode no.	Natural frequency	Mode description
1	1.23	Horizontal out of plane movement of long cantilever
2	2.42	Vertical in plane movement of cantilever
3	2.45	Horizontal out of plane movement of span between columns
4	3.45	Horizontal out of plane movement of short cantilever including one column
5	3.88	Horizontal out of plane movement of lamp support beam. The beam shape is like a 3rd degree function
6	4.17	In plane movement of whole structure
7	5.55	Horizontal movement out of plane of lamp support beam. The beam shape is like a 2nd degree function
8	6.65	Horizontal movement out of plane of lamp support beam. The beam shape is like a 4th degree function
9	8.21	Vertical in plane movement of span between columns

Table 4.1: Mode shapes for the open-section beam model

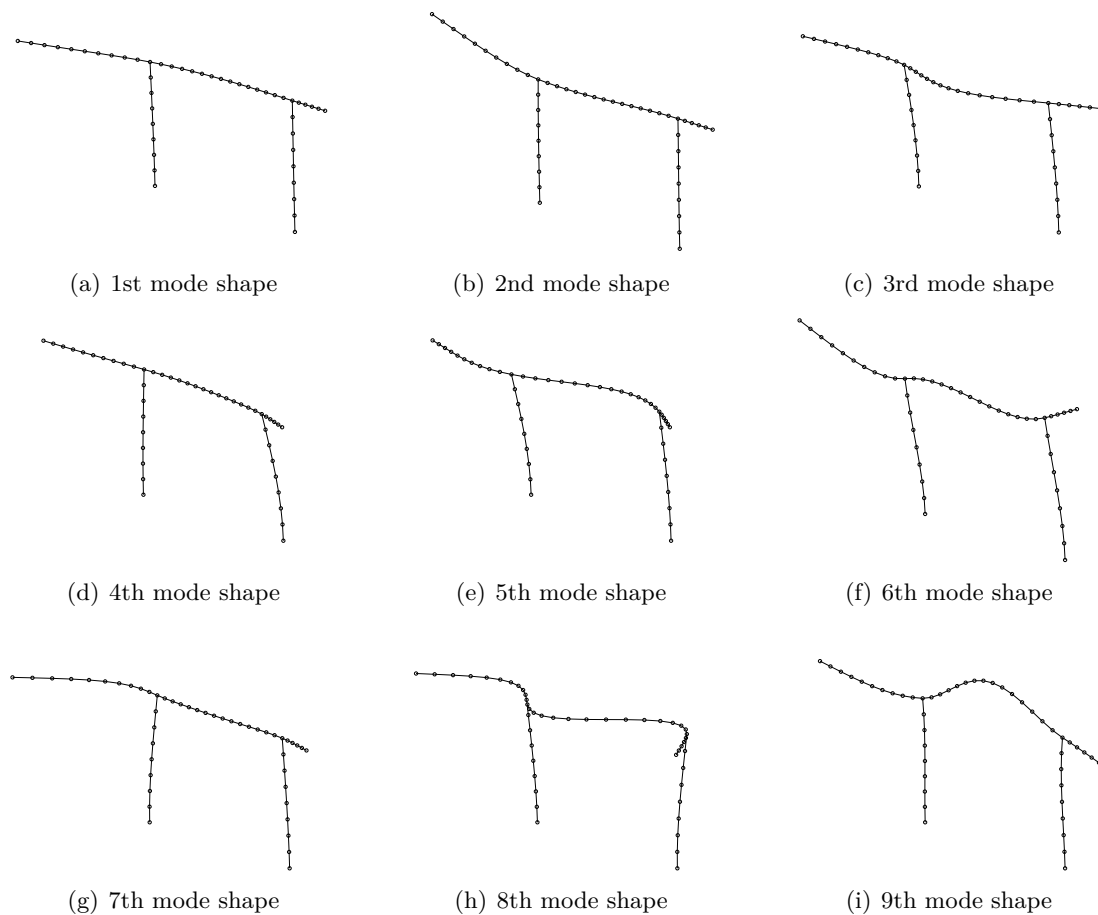


Figure 4.2: Mode shape 1-9 of the open-section beam element model

The resulting mode shapes showed, in contradiction to model No.1, continuous deformation. All mode shapes were now looking natural, as shown in figure 4.2. But it was discovered that the results were quite different from the results of Bessason and Snaeþbjörnsson. The natural frequency of the first mode shape, which is the horizontal cantilever movement has a frequency of 1.23 Hz. Bessason and Snaeþbjörnsson found this to be 1.94 Hz. And when this model gave nine mode shapes when including the vertical movement of the span as the last, Bessason and Snaeþbjörnsson only found six. The 4th, 5th, 7th and 8th mode shape of this model can not be found in the Bessason and Snaeþbjörnsson-model, while the 5th mode shape of the Bessason and Snaeþbjörnsson-model could not be found in this model.

As the frequency of the first horizontal cantilever mode of the Bessason and Snaeþbjörnsson-model is 58% higher than what it is for this model, a significantly different horizontal stiffness is suspected in the two models. It was therefore natural to believe that the model of Bessason and Snaeþbjörnsson had used a different element formulation. An attempt was therefore made to replica the results of Bessason and Snaeþbjörnsson, and model No.3 was therefore made.

4.2.3 Model No.3 - Beam model with closed section

The third model made was a beam element model with the lamp supporting beam modelled as a closed hollow section with a bottom flange of 0.1mm. The thin flange is included to make the section to be reckoned as a closed section, and the flange would also prevent warping of the section, just as the 25mm bars partially are expected to do. The purpose of this analysis was also hopefully to replicate the results of Bessason and Snaeþbjörnsson. The element formulation used is the standard linear beam element (B31). The geometry, boundary conditions and element meshing of this model was just as for model No.1 and 2.

Mode no.	Natural frequency	Mode description
1	1.92	Horizontal out of plane movement of long cantilever
2	2.39	Vertical in plane movement of cantilever
3	3.09	Horizontal out of plane movement of span between columns
4	4.12	Horizontal in plane movement of whole structure
5	4.48	Horizontal out of plane movement of whole structure. The columns moves out of phase, and the lamp supporting beam exhibits torsion.
6	8.07	Vertical in plane movement of span between columns

Table 4.2: Mode shapes of the closed-section beam model

The results from this model as shown in table 4.2, show a good agreement with Bessason and Snaeþbjörnsson. The order of the mode shapes is identical, and the deviation of the results is at maximum 2.5%. This model was therefore clarifying some of the questions accrued during the study of model No.1 and No.2.

The question which remains unanswered by model No.2 and No.3 was to what degree the 25mm bars contribute to the structural stiffness. As quite large deviations were found between the results for the horizontal mode shapes of the models, it was seen that the effect of simplifying the beam to being either closed or open was significant. The 25mm bars are expected to contribute to the stiffness of the structure, but to what degree? As it was seen

that the beam element modelling approach could not answer this question, a shell element model was made.

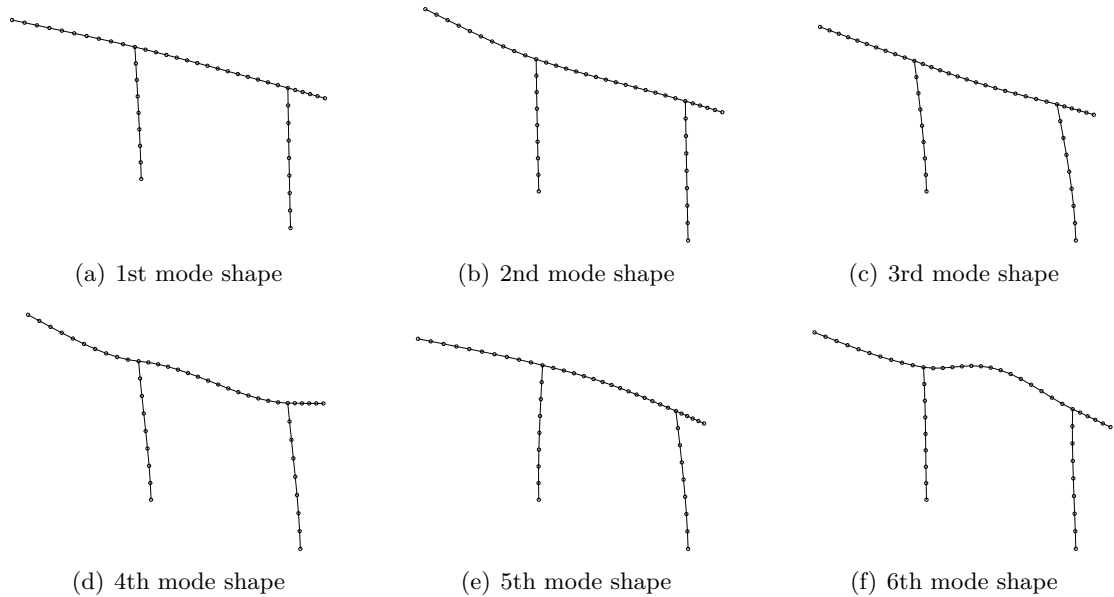


Figure 4.3: Mode shape 1-6 of the closed-section beam element model

4.2.4 Model No.4 - Shell model

The shell-element model was built up by 8-node quad elements with a thickness of 10mm. The 25mm bars in the bottom part of the U-section were modelled as beam elements. The size of the shell elements was 100mm in each direction and the model had 6353 elements in total. The results are shown in table 4.2.

Mode no.	Natural frequency	Mode description
1	1.38	Horizontal out of plane movement of long cantilever
2	2.28	Vertical in plane movement of cantilever
3	2.53	Horizontal out of plane movement of whole structure
4	3.54	Horizontal out of plane movement of whole structure. The columns moves out of phase, and the lamp supporting beam exhibits torsion
5	3.97	Horizontal in plane movement of whole structure
6	4.65	Beam in torsion
7	6.31	Beam in torsion
8	7.56	Vertical in plane movement of span between columns

Table 4.3: Mode shapes for the shell element model

The shell element model gives eight different modes when including the vertical movement of the U-section span as the last one. There are six mode shapes which are basically similar

to the mode shapes found in the two other models, namely mode shape 1,2,3,4,5 and 8. The torsional modes at the 6th and 7th mode are only found by this model.

When comparing the natural frequencies of the first mode calculated by the different models, the results for model No.2, No.3 and No.4 are respectively 1.23Hz, 1.92Hz and 1.38Hz. It is seen that model No.4 places itself in between of the two others, but closest to model No.2.

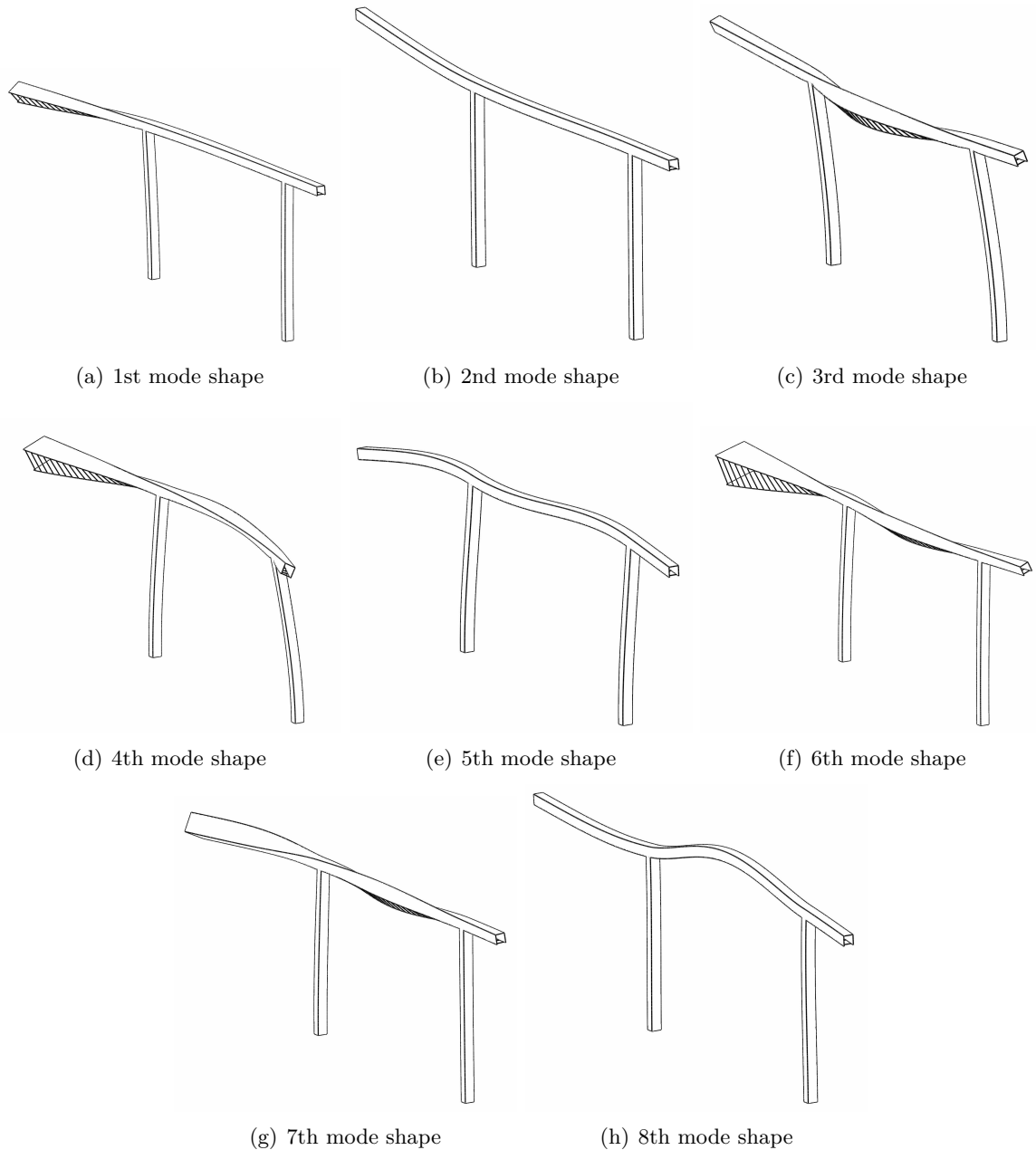


Figure 4.4: Mode shape 1-8 of the shell element model

4.3 Conclusion

Four different models have been made as a part of the modal analysis. Model No.1 gave obviously incorrect results and was disregarded, but the three others have been further evaluated. The results from the three models, as shown in table 4.1, 4.2 and 4.3, indicate that the differences between the different models are small concerning the vertical modes. For the horizontal modes, where the torsional stiffness of the U-section is important, the results are very divergent. Model No.2 and No.3 were both simplifying the geometry of the section, by either neglecting the stiffness provided by the 25mm bars or including the pin as acting as a closed section. The deviation between these model's was seen to be as much as 58% for the first mode. As the difference between these model was so significant, a shell element model was made. The shell element model provided the possibility of modelling the structure more accurate. It was seen that the results from this model's horizontal modes placed themselves inbetween of the two others. As the stiffness of the 25mm bars has been modelled in model No.4, this model is belived to be the one closest to reality. The results from the shell element model will therefore be used in the further analyses and calculations of this report.

Through the modal analysis of the light mast, the torsional stiffness of a semi-closed section has been analysed. It is found that the use of different beam element formulations gave very divergent results. For this structure it was found that a shell element model was necessarily to provide a modelling techique that could give accurate results for the semi-closed U-section.

Chapter 5

Computational Fluid Dynamics

5.1 General

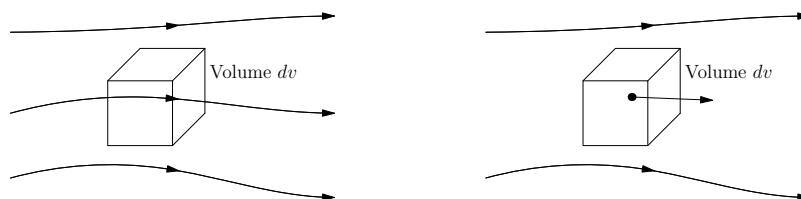
Computational fluid dynamics (CFD) is a method of solving systems involving fluid flow and heat transfer based on computer simulations. The method involves discretizing of the fluid flow and the use of numerical calculation methods for solving partial differential equations.

5.2 Governing equations

Computational fluid dynamics is based on three governing equations.

1. Mass is conserved (The continuity equation)
2. Newton's second law, $\mathbf{F}=\mathbf{ma}$ (The momentum equation)
3. Energy is conserved (The energy equation)

The governing equations can be derived in two forms, the conservation form and the nonconservation form, ref. figure 5.1.



(a) Conservation form: An infinitesimal fluid element fixed in space with the fluid moving through it
(b) Nonconservation form: An infinitesimal fluid element moving along the fluid

Figure 5.1: The two different forms used for deriving the governing equations

¹Section 5.2 is based on Anderson [1995, Ch.2].

The two different forms uses different differential operator. For the conservation form, the local derivate $\partial/\partial t$ is used, meaning time rate of change at a fixed point. For the nonconservation form, the substantial derivate D/Dt is used,

$$\frac{D}{Dt} = \frac{\partial}{\partial t} + u \frac{\partial}{\partial x} + v \frac{\partial}{\partial y} + w \frac{\partial}{\partial z} \quad (5.1)$$

with the physical meaning instantaneous time rate of change for a moving fluid element.

5.2.1 The continuity equation

Imagine a infinitesimally small element fixed in space with the fluid moving through it:

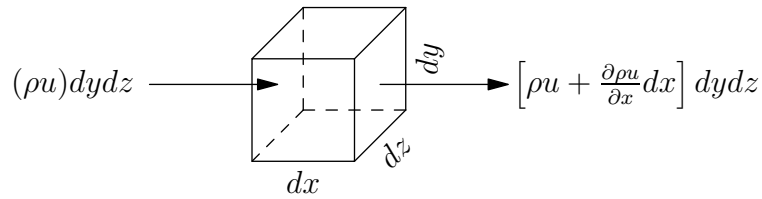


Figure 5.2: An infinitesimally small element fixed in space with mass flux through the faces.

Figure 5.2 shows the mass flux in the x-direction of flow. The net outflow in the x-direction is:

$$\left[\rho u + \frac{\partial(\rho u)}{\partial x} dx \right] dy dz - (\rho u) dy dz = \frac{\partial(\rho u)}{\partial x} dx dy dz \quad (5.2)$$

The terms are similar for y and z-direction. From the basis of the terms in all directions, the total mass flow out of the element can be summarized as

$$\left[\frac{\partial(\rho u)}{\partial x} + \frac{\partial(\rho v)}{\partial y} + \frac{\partial(\rho w)}{\partial z} \right] dx dy dz \quad (5.3)$$

The total mass of the fluid element is $m = \rho(dx dy dz)$. The time rate of mass increase can therefore be written

$$\frac{\partial \rho}{\partial t} (dx dy dz) \quad (5.4)$$

The net mass flow out of the element must be equal to the time rate of decrease of mass inside the element:

$$\begin{aligned} \left[\frac{\partial(\rho u)}{\partial x} + \frac{\partial(\rho v)}{\partial y} + \frac{\partial(\rho w)}{\partial z} \right] dx dy dz &= -\frac{\partial \rho}{\partial t} (dx dy dz) \\ \frac{\partial \rho}{\partial t} + \left[\frac{\partial(\rho u)}{\partial x} + \frac{\partial(\rho v)}{\partial y} + \frac{\partial(\rho w)}{\partial z} \right] &= 0 \\ \frac{\partial \rho}{\partial t} + \nabla \cdot (\rho \mathbf{V}) &= 0 \end{aligned} \quad (5.5)$$

Equation 5.5 is a partial differential equation form of the continuity equation for a compressible fluid. For an incompressible fluid, the density ρ is constant, and the equation reduces to:

$$\nabla \cdot \mathbf{V} = 0 \quad (5.6)$$

5.2.2 The momentum equation

The momentum equation is derived from the second law of Newton $F=ma$. The equation is here derived in the nonconservation form and a model of a infinitesimal small volume element moving with the flow is used.

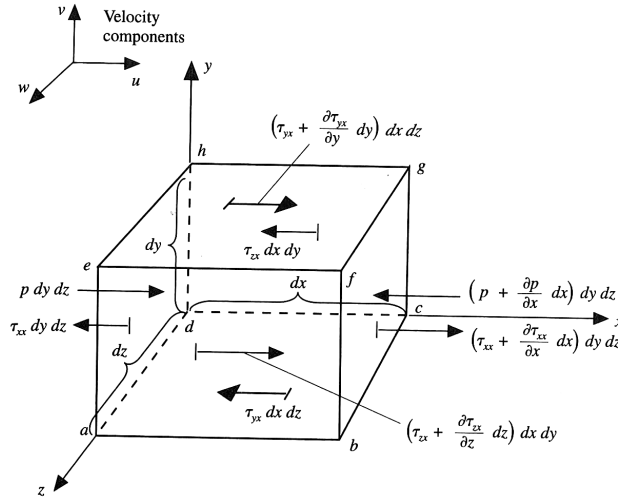


Figure 5.3: Stress components in the x-direction Anderson [1995].

The forces on the element are divided into body forces and surface forces. In figure 5.3 the surface forces are shown. Imagine that the volume element is moving with the flow in the positive x-direction. The forces on the volume's sides (abfe, dcgh, abcd and efgh) are due to the viscosity of the fluid as the volume is moving through it. On back and front sides (adhg and bcgf) you have normal stresses due to suction and drag in addition to the pressure forces. The forces in figure 5.3 can be summarized as follows:

$$\begin{aligned} & \left[p - \left(p + \frac{\partial p}{\partial x} dx \right) \right] dy dz + \left[\left(\tau_{xx} + \frac{\partial \tau_{xx}}{\partial x} dx \right) - \tau_{xx} \right] dy dz \\ & + \left[\left(\tau_{yx} + \frac{\partial \tau_{yx}}{\partial y} dy \right) - \tau_{yx} \right] dx dz + \left[\left(\tau_{zx} + \frac{\partial \tau_{zx}}{\partial z} dz \right) - \tau_{zx} \right] dx dy \end{aligned} \quad (5.7)$$

In addition there are body forces on the volume element, where f_x denotes the x-component of the body force pr unit mass:

$$\rho f_x (dx dy dz) \quad (5.8)$$

The total forces in the x-direction is the sum of equation 5.7 and 5.8. This can be summarized, shortened and written as:

$$F_x = \left[-\frac{\partial p}{\partial x} + \frac{\partial \tau_{xx}}{\partial x} + \frac{\partial \tau_{yx}}{\partial y} + \frac{\partial \tau_{zx}}{\partial z} \right] dx dy dz + \rho f_x dx dy dz \quad (5.9)$$

Equation 5.9 represent the left-hand side of $F_x = ma_x$. Considering the right-hand side, the mass m of the fluid element is equal to

$$m = \rho dx dy dz \quad (5.10)$$

while the acceleration, a_x is equal to the time rate of change of the velocity u . Since the element is moving with the flow, the time rate of change is given by the substantial derivative D/Dt . Thus a_x is given by

$$a_x = \frac{Du}{Dt} \quad (5.11)$$

The total x-component of the momentum equation is then aquired by combining equations 5.9, 5.10 and 5.11:

$$\rho \frac{Du}{Dt} = -\frac{\partial p}{\partial x} + \frac{\partial \tau_{xx}}{\partial x} + \frac{\partial \tau_{yx}}{\partial y} + \frac{\partial \tau_{zx}}{\partial z} + \rho f_x \quad (5.12)$$

The momentum equation can be derived in a similar manner for the y- and z-direction. The derived expression is nonconservation form of the momentum equation.

5.2.3 The energy equation

The energy equation can be derived from the physical principle that energy is conserved. This is the first law of thermodynamics. The energy equation can be written in words as:

$$\begin{array}{l} \text{Rate of change of} \\ \text{energy inside fluid} \\ \text{element} \end{array} = \begin{array}{l} \text{Net flux of heat} \\ \text{into element} \end{array} + \begin{array}{l} \text{Rate of work done on} \\ \text{element due to body} \\ \text{and surface forces} \end{array} \quad (5.13)$$

The energy equation is here derived in the nonconservation form. The rate of work done on the element can be divided into work done by body or work by surface forces. The rate of work done by body forces is equal to the product of the force and the velocity in the direction of the force, and can therefore be written

$$\rho \mathbf{f} \cdot \mathbf{V} (dx dy dz) \quad (5.14)$$

where \mathbf{f} is the force vector pr unit mass, $\rho (dx dy dz)$ is mass and \mathbf{V} is the velocity vector.

The rate of work done by surface forces can be derived from figure 5.4. For the pressure and shear forces in the x-direction the work done is equal to the product of the velocity in the x-direction, u and the force. The terms in figure 5.4 can be added together and written as

$$\begin{aligned} & \left[up - \left(up + \frac{\partial(up)}{\partial x} dx \right) \right] dy dz + \left[\left(u\tau_{xx} + \frac{\partial(u\tau_{xx})}{\partial x} dx \right) - u\tau_{xx} \right] dy dz \\ & + \left[\left(u\tau_{yx} + \frac{\partial(u\tau_{yx})}{\partial y} dy \right) - u\tau_{yx} \right] dx dz + \left[\left(u\tau_{zx} + \frac{\partial(u\tau_{zx})}{\partial z} dz \right) - u\tau_{zx} \right] dx dy \end{aligned} \quad (5.15)$$

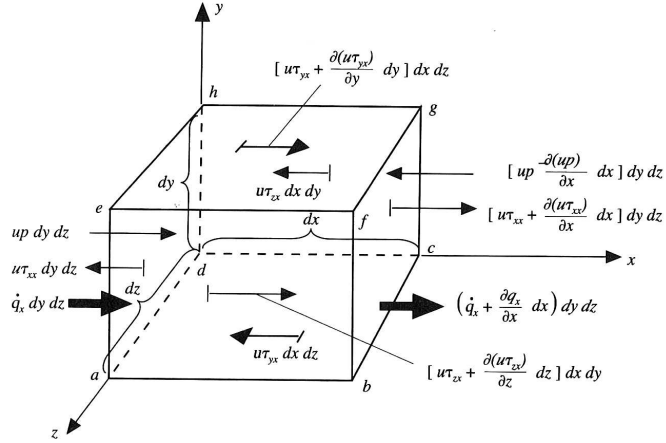


Figure 5.4: Energy fluxes in the x-direction Anderson [1995].

Adding and cancelling terms, this reduces to

$$\left[-\frac{\partial(up)}{\partial x} + \frac{\partial(u\tau_{xx})}{\partial x} + \frac{\partial(u\tau_{yx})}{\partial y} + \frac{\partial(u\tau_{zx})}{\partial z} \right] dx dy dz \quad (5.16)$$

If terms for y- and z-direction are added, the total rate of work done by body and surface forces can be written

$$\left[-\left(\frac{\partial(up)}{\partial x} + \frac{\partial(vp)}{\partial y} + \frac{\partial(wp)}{\partial z} \right) + \frac{\partial(u\tau_{xx})}{\partial x} + \frac{\partial(u\tau_{yx})}{\partial y} + \frac{\partial(u\tau_{zx})}{\partial z} + \frac{\partial(v\tau_{xy})}{\partial x} + \frac{\partial(v\tau_{yy})}{\partial y} + \frac{\partial(u\tau_{zy})}{\partial z} + \frac{\partial(w\tau_{xz})}{\partial x} + \frac{\partial(w\tau_{yz})}{\partial y} + \frac{\partial(w\tau_{zz})}{\partial z} \right] dx dy dz + \rho \mathbf{f} \cdot \mathbf{V} dx dy dz \quad (5.17)$$

The next term in the energy equation is the net flux of heat into the element. The heat flux is due to volumetric heating such as absorption or emission of radiation and the heat transfer across the surface due to thermal conduction.

The volumetric heating of the element is the product of the rate of volumetric heat addition per unit mass, \dot{q} and the mass, $\rho (dx dy dz)$

$$\rho \dot{q} dx dy dz \quad (5.18)$$

The heating caused by thermal conduction is found for each direction by looking at the heat flux in to and out of the element. Figure 5.4 shows the heat flux in the x-direction. The sum of the heat flux across the surface in all directions is

$$-\left(\frac{\partial \dot{q}_x}{\partial x} + \frac{\partial \dot{q}_y}{\partial y} + \frac{\partial \dot{q}_z}{\partial z} \right) dx dy dz \quad (5.19)$$

The total net flux into the element is the sum of eq. 5.18 and eq. 5.19

$$\left[\rho \dot{q} - \left(\frac{\partial \dot{q}_x}{\partial x} + \frac{\partial \dot{q}_y}{\partial y} + \frac{\partial \dot{q}_z}{\partial z} \right) \right] dx dy dz \quad (5.20)$$

Then, Fourier's law of heat conduction $\dot{q}_x = -k \partial T / \partial x$ is introduced (with similar expressions for y- and z-direction), and the total net flux into the element can be written

$$\left[\rho \dot{q} + \frac{\partial}{\partial x} \left(k \frac{\partial T}{\partial x} \right) + \frac{\partial}{\partial y} \left(k \frac{\partial T}{\partial y} \right) + \frac{\partial}{\partial z} \left(k \frac{\partial T}{\partial z} \right) \right] dx dy dz \quad (5.21)$$

The last term of the energy equation is the rate of change of the energy inside the fluid element. The element's internal energy is the sum of energy of all molecules or atoms in the element. This energy consists of translational, rotational, vibrational and electronic energies. The internal energy is denoted as e , and is per unit mass.

In addition to internal energy, the element has kinetic energy since the element is moving. The kinetic energy of the fluid element is $\frac{1}{2} m V^2$, giving that the kinetic energy per unit mass is $V^2/2$

The sum of the internal and the kinetic energy is the total energy of the fluid element. The time rate of change of the total energy per unit mass is given by the substantial derivate. The mass of the element is $\rho(dx dy dz)$. This leads to the total expression for the rate of change of the energy inside the fluid element:

$$\rho \frac{D}{Dt} \left(e + \frac{V^2}{2} \right) dx dy dz \quad (5.22)$$

Now all three terms in the energy equation have been derived, and the terms from equations 5.22, 5.21 and 5.17 can be inserted into equation 5.13:

$$\begin{aligned} \rho \frac{D}{Dt} \left(e + \frac{V^2}{2} \right) &= \rho \dot{q} + \frac{\partial}{\partial x} \left(k \frac{\partial T}{\partial x} \right) + \frac{\partial}{\partial y} \left(k \frac{\partial T}{\partial y} \right) + \frac{\partial}{\partial z} \left(k \frac{\partial T}{\partial z} \right) \\ &\quad - \frac{\partial(up)}{\partial x} - \frac{\partial(vp)}{\partial y} - \frac{\partial(wp)}{\partial z} + \frac{\partial(u\tau_{xx})}{\partial x} + \frac{\partial(u\tau_{yx})}{\partial y} + \frac{\partial(u\tau_{zx})}{\partial z} + \frac{\partial(v\tau_{xy})}{\partial x} \\ &\quad + \frac{\partial(v\tau_{yy})}{\partial y} + \frac{\partial(u\tau_{zy})}{\partial z} + \frac{\partial(w\tau_{xz})}{\partial x} + \frac{\partial(w\tau_{yz})}{\partial y} + \frac{\partial(w\tau_{zz})}{\partial z} + \rho \mathbf{f} \cdot \mathbf{V} \end{aligned} \quad (5.23)$$

This is the energy equation in the nonconservation form.

5.3 Numerical calculation methods used in CFD

The numerical calculation methods used in CFD are,

- The finite difference method (FDM)
- The finite volume method (FVM)
- The finite element method (FEM)

The numerical methods used in CFD are a comprehensive subject, and the subject is therefore difficult to summarize in short terms. But a comparison of the methods is here presented, as published by Shaw [1992]. The three methods have several similarities:

- The methods produce equations for the values of the variable at a finite number of points in the domain under consideration.
- For time dependent problems an initial condition has to be set.
- Boundary conditions have to be set.
- Each method can either produce explicit or implicit forms. If an implicit form is produced, then a set of simultaneous equations must be solved.

Shaw [1992] also summarizes the differences between the methods:

- The finite difference and the finite volume method produce the numerical equations in one node based on the values in the neighbouring nodes. The finite element method produces the equations for each element independently. The interaction between the elements is first taken into account when the element matrices are collected to the global system matrices.
- The finite element method takes care of derivative boundary conditions when the element equations are formed and then the fixed values of variables must be applied to the global matrices. This contrasts with the other two methods which can easily apply the fixed-value boundary conditions by inserting the values into the solution, but must modify the equations to take account of any derivative boundary conditions.
- The finite difference method requires a uniform grid either in cartesian coordinates, in other coordinate systems or in a transformed coordinate system. The method therefore has its shortcomings when dealing with complex geometries. The finite volume and finite element method both allow unstructured grids.

Most commercial CFD software use either FVM or FEM, where FVM is the most used method. More information regarding the mathematical difference between FVM and FEM can e.g. be found in Idelsohn and Oñate [1994].

5.4 Turbulence

Flow can be laminar, in transition phase or turbulent. As Reynolds number increase, a transition from laminar to turbulent flow will be induced. CFD software often ignores the transition phase, and only operates with predefined flow, either laminar or turbulent. The transition region often constitutes only a very small fraction of the size of the flow domain and in those cases it is assumed that the errors made by neglecting its detailed structure are only small [Versteeg and Malalasekera, 2007, p.49].

Turbulent flow is described by a mean component Φ and a turbulent component $\varphi'(t)$:

$$\varphi(t) = \Phi + \varphi'(t) \quad (5.24)$$

where the time average of the turbulent component is zero by definition.

In CFD code, there are different turbulence models available to capture the effects of turbulence. The turbulence models can generally be grouped into three categories:

¹Section 5.4 is based on Versteeg and Malalasekera [2007].

- **Turbulence models for Reynolds-averaged Navier-Stokes equations(RANS)**
The Navier-Stokes equations are time averaged. The flow equations consist extra terms for modelling turbulence. These terms are modelled with different turbulence models. The RANS turbulence models require modest computer resources for reasonably accurate flow calculations, and these models have therefore been the most used models for engineering calculations the last three decades.
- **Large eddy simulation**
This method tracks the behaviour of the larger eddies and involves space filtering of the unsteady Navier-Stokes equations prior to the computation. The filtering passes the larger eddies and rejects the smaller eddies. The effect from the small unresolved eddies is included by means of a so-called sub-grid model. The method involves solving of unsteady flow equations, and the computing resources required for this are large.
- **Direct numerical simulation**
The method computes the mean flow and all turbulent velocity fluctuations. The method is highly costly in terms of computational resources and is not used for industrial flow computations.

The RANS equations is as mentioned the most used method for engineering purposes. It is necessary to develop turbulence models to predict the turbulence since the time-averaging operation on the momentum and transport equation produce additional unknown terms.

The most common turbulence models are:

- The mixing length model
- The Spalart-Allmaras model
- The k- ϵ model
- The k- ω model
- The Algebraic stress model
- The Reynolds stress model (RSM)

The different turbulence models have different advantages, disadvantages and area of use. A more detailed description of the different turbulence models can be found in Versteeg and Malalasekera [2007]. As the Spalart-Allmaras model is used in this project a further discussion of this can be found in section 6.2.4.

5.5 Errors and uncertainty in CFD modelling

The nature of CFD, being a numerical method, introduces many sources of error and uncertainty. A summary is here presented.

¹Section 5.5 is based on Versteeg and Malalasekera [2007].

5.5.1 Numerical errors

CFD is a method of solving non-linear partial differential equations using numerical methods. This introduces three sources of numerical errors:

- **Roundoff error**

The computers interpretation of a real number is a number with a finite number of significant digits. This introduces the roundoff error.

- **Iterative convergence error**

The numerical solution of a CFD problem is based on an iterative process. Convergence limits are specified by the user in the input of CFD programs. When the solution has converged within the limit specified, the problem is considered solved. This leaves a truncation error for every set of iteration with a magnitude dependent on the convergence input limit.

- **Discretisation error**

A CFD model is a discretisation of a physical problem. The problem is discretized in time and space mesh. The mesh design is of vital importance to achieve high-quality CFD results. In theory, the discretisation error can be made arbitrarily small by progressive reduction of the time step and mesh, but this requires increasing amount of computing time.

5.5.2 Input uncertainty

The modelling itself introduces several user-controlled sources of errors. A computers solution to a problem is never better than the input. There are several input uncertainties:

- **Geometry input**

The meshing of complex geometries can be problematic and simplification in the mesh are therefore necessarily. In addition the fabrication of an item always introduces a degree of geometry deviation which also introduces geometry errors.

- **Boundary conditions**

A CFD model requires a certain set of boundary conditions to be specified. These boundary conditions consist e.g. of inlet, outlet, wall conditions and turbulence model boundary conditions. The conditions are often set based on assumptions and simplifications.

- **Fluid properties**

Fluid properties like density, viscosity and thermal conductivity depend to a greater or lesser extent on the local value of the flow parameters like velocity and pressure. These properties are often assumed constant. This is acceptable provided that the variation in the fluid properties in reality are small.

5.5.3 Validity of sub-models

Another source of errors are the sub-models used in the CFD analysis. Sub-models exist for turbulence, combustion, heat and mass transfer. For aerodynamic use of CFD, the turbulence model is the most relevant. Turbulence models are often semi-empirical. They have been

tuned to fit experimental data to solve one type of flow problems, and therefore have their validity area. They also have different ways of solving the boundary layer. The $k-\epsilon$ model for instance, uses a ‘wall function’ that uses algebraic relationships to solve the near-wall region. This method requires near-wall grid points at an y^+ distance of 30 to 500. Other models requires a different near-wall grid spacing. The Spalart Allmaras model requires for instance a y^+ of approximately 3 to achieve a good solution of the boundary layer [Abaqus documentation, 2010]. It is therefore important that the near-wall grid spacing is adjusted to fit the turbulence model’s wall approach.

5.5.4 Simplifications

For saving computer-time in analyses, simplifications are often used. Common simplifications are:

- Steady vs. transient flow
- Two-dimensional or axisymmetric vs. three-dimensional
- Incompressible vs. compressible
- Adiabatic vs. heat transfer across the boundaries
- Singlephase vs. multiphase

These simplifications can sometimes safely be used and sometimes not. Flow speeds below a mach number of 0.3 can for instance safely be treated as incompressible. But dealing with axisymmetrical models simplifications can not be used unless all parameters are axisymmetrical, and not just the geometry. It is tempting to simplify to an axisymmetrical model when having an almost symmetrical inflow and symmetric geometry, but in some cases small variations of inflow can be amplified and the simplification to an axisymmetric model will give major discrepancies between an axisymmetric model and the real flow.

5.5.5 Verification and validation of CFD results

The sources of errors and uncertainties in CFD are many and unavoidable. A verification and validation of the CFD model is necessarily to quantify the errors. The numerical errors can be quantified by using these methods:

- The roundoff errors can be quantified by a comparison between different levels of computer accuracy.
- The iterative convergence error can be quantified by a systematic study of the effects of changing the convergence criteria. Different parameters, like pressure and velocity, can be compared to quantify the convergence error.
- The discretization error can be quantified by a mesh/time-step refinement study. The mesh is systematically refined until monotonic reduction of the discretisation error is met for two or three levels of mesh refinement. A method of discretisation error estimation can be found in Versteeg and Malalasekera [2007, p.294].

However, the best verification of a CFD analysis is a comparison between the CFD output and experimental data. An important aspect here is that the quality of this validation will rely on the quality of the experimental data. If a comparison to low-quality data is made the quality of the validation is poor.

Since a comparison is based on subjective judgement, several suggestions have been proposed for a more rigorous basis for validation of CFD results. These methods are using statistical approaches for the comparison, and are therefore able to take the deviation of the experimental data into account when judging the quality of the CFD results. These methods are described in more detail by Versteeg and Malalasekera [2007, p.296].

Chapter 6

CFD Model

6.1 Software

The CFD analyses are performed in Abaqus 6.10 Pre-release v.3-v.5. The implementation of a CFD solver is brand new in version 6.10 of Abaqus. The numerical implementation of CFD is based on the finite element method. For time-dependent problems, a second-order projection method is used. The pressure is calculated through a node centered approach, and the transport equations have an edge-based implementation [Abaqus documentation, 2010].

6.2 Modelling

6.2.1 Geometry

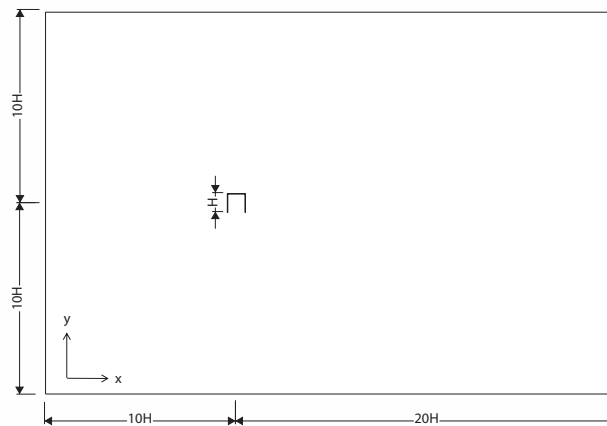


Figure 6.1: The model's dimensions in x- and y-direction.

The model's dimensions in x- and y-direction are set up according to the height of the U-section ($H=0.4\text{m}$). The model has dimensions $10H$ in front of, $20H$ in back and $10H$ above and below the U-section. It is important that the boundaries are not too close to the area of interest. If the boundaries are too close, the results will be affected. Versteeg and Malalasekera [2007, p.283] recommends outlet boundary conditions to be placed further than

10 heights downstream of an obstacle. As our model has $20H$ downstream, this dimension is well within the recommended value.

The CFD model is in 3D. This is because only 3D fluid elements are available in Abaqus. The fluid element used is a 8-node brick element. As it first was planned to use a 2D model, only one element in the z-direction was modelled initially. This worked fine when analysing laminar flow, but when the Spalart-Allmaras turbulence model was activated, the analysis would not run. This was found to be due to the model having only one element in z-direction, and the number of elements was therefore increased. Because of this, the z-dimension needed to be decided. Several different z-lengths and number of elements have been evaluated, as described in section 6.4. Although a 2D model would have been used if possible, the benefit from using 3D is that vortex shedding also has 3D effects. Hopingly this has increased the solution's accuracy. The flow in the z-direction is however not focused on and a coarse mesh in the z-direction has been used.

6.2.2 Boundary conditions

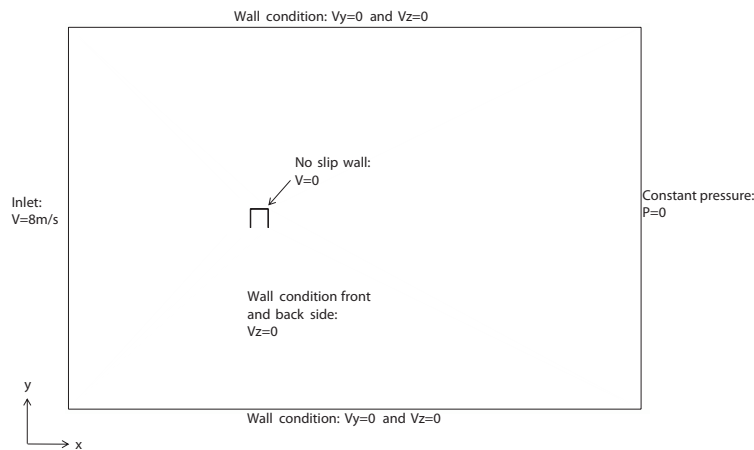


Figure 6.2: The model's boundary conditions.

The boundary conditions of the model are set using an inlet condition with a specified velocity, several different wall conditions, and an outlet with a constant pressure. The boundary conditions are shown in figure 6.2.

The inlet velocity is set to 8 m/s for all analyses. This velocity was initially chosen since the lightmast measurements showed large oscillations at this velocity. It is therefore believed that this velocity is within the lock-in range of the critical velocity of the vertical cantilever movement mode shape.

The outlet is specified with a constant pressure of zero. This boundary condition is appropriate for external flows having a constant atmospheric pressure. A zero pressure is specified instead of the atmospheric pressure since the atmospheric pressure is equal in all directions and therefore doesn't contribute to the forces acting on the U-section.

The boundary conditions at the U-section is specified as no-slip walls, meaning that all velocity components are set to zero.

At the sides, top and bottom of the model, “shear” wall-conditions are specified. The fluid does not adhere to the wall but cannot penetrate it.

6.2.3 Solver settings

The solver settings specified in the set-up of the analyses consists among others of fluid parameters, time incrementation settings and convergence settings. The fluid parameters used for air are shown in table 6.1:

Density	1.225 kg/m^3 ($15^\circ C$)
Viscosity	1.7894e-5 $kg/(m \cdot s)$ ($11^\circ C$)

Table 6.1: Fluid settings

The time step incrementation in Abaqus are at default set to be automatic. According to Abaqus documentation [2010], this guarantees for the solution’s stability. The time step will adjust itself automatically according to a stability condition called the Courant-Freidrichs-Levy (CFL) stability condition. The time step can be specified manually at fixed incrementation, but stability may not be guaranteed. The default setting with automatic time step has been used in the analyses.

Time step incrementation	Automatic (Fixed CFL)
Initial time increment	0.01s
Maximum CFL number	0.45
Increment adjustment frequency	1
Time step growth scale factor	0.025
Divergence tolerance	1e-10
Time Integration Parameters	Viscous,Load,BC - Trapezoid(1/2)

Table 6.2: Time incrementation settings

The solver settings for the three governing equations are shown in table 6.3. These settings are the default values in Abaqus and were not changed.

Momentum equation	
Iteration limit	50
Convergence checking frequency	2 increments
Linear convergence limit	1e-5
Pressure equation	
Iteration limit	250
Convergence checking frequency	2 increments
Linear convergence limit	1e-5
Transport equation	
Iteration limit	50
Convergence checking frequency	2 increments
Linear convergence limit	1e-5

Table 6.3: Solver settings

6.2.4 Turbulence model

Two different turbulence model are available in Abaqus CFD, namely the Implicit Large-Eddy Simulation (ILES) model and the Spalart-Allmaras model. The Spalart-Allmaras model is a RANS model (ref section 5.4). It is a one-equation model, meaning that one additional partial differential equation has to be solved. This equation is a conservation equation for the eddy viscosity (also known as the turbulent viscosity). The Spalart-Allmaras model uses less computer resources than two-equation models like the $k - \epsilon$ model. The model has constants that can be calibrated to different flow problems. The default constants are tuned for external aerodynamic flow. The eddy viscosity is varying through the domain and is calculated from the constants, the vorticity and the near-wall distance [Spalart and Allmaras, 1994]. The model produces reasonable accurate predictions of turbulent flows in the presence of adverse pressure gradients, and may be used for flow where separation occur [Abaqus documentation, 2010]. The model is originally designed for streamlined shapes like airfoils, and according to [Bakker, 2010], the model is weak for massivly seperated flow and free shear flows.

The information found on the Spalart-Allmaras model reveals both pros and cons of this model. This is however the reality of all turbulence models, since no universal turbulence model exists. In our case, we have an external aerodynamic flow where we expect separation and recirculation at the U-section's corners. The question is how accurately the separation around the U-section will be solved in the Spalart-Allmaras model.

In the end, when considering the information found on the two turbulence models available, the Spalart-Allmaras model was preferred because of the computational efficiency, and this was therefore used in all analyses.

The boundary conditions and an initial eddy viscosity $\tilde{\nu}$ have to be specified for the turbulence model. The eddy viscosity at all walls are automatically set to zero by Abaqus. At the inlet and outlet, the eddy viscosity needs to be specified. According to [NASA, 2010], the eddy viscosity boundary conditions should be between 3 and 5 times the kinematic viscosity ν . [CFDOnline, 2010] recommends a freestream value of 5ν . An eddy viscosity of 5ν

was therefore intended to be used, but during the model setup, this was erroneously specified to 5 times the dynamic viscosity μ instead. This means that an inlet eddy viscosity of 6.1ν has been used in the analyses.

6.2.5 Computer information

The analyses have been performed on a Windows XP computer running four CPUs at 1.86 GHz clock speed. The amount of RAM was 3.25Gb. The analyses were run using either at three or four CPUs. There was some incidents of analysis abortion when running at four CPUs, and therefore three CPUs were sometimes used to be on the safe side.

6.3 Post-processing in Abaqus and Matlab

The postprocessing of the results have been performed by the built in postprocessor of Abaqus in combination with Matlab.

The results of primarily interest in these analyses are the non-dimensional force coefficients, defined as:

$$C_D = \frac{F_x}{\frac{1}{2}\rho AU^2} \quad (6.1)$$

$$C_L = \frac{F_y}{\frac{1}{2}\rho AU^2} \quad (6.2)$$

where F is the force, A is the projected area and U is the wind speed and ρ is the density of air.

The force coefficients are not a part of the analysis output, and therefore further post-processing was done in Matlab. The pressure at the nodes around the section was exported to text files. The nodes at the edges in the z-direction were generally excluded. A Matlab program was made to combine the scalar pressure with the section geometri, creating the force vectors. Then the force vectors could be used to calculate C_D and C_L . The Matlab code can be found in appendix E.

Since the force coefficients are calculated from the pressure, the frictional forces are not included in the coefficients. But since the Reynold's number is high ($2.2 \cdot 10^5$), the frictional forces are small compared to the forces due to pressure. The error of excluding the frictional forces are therefore very small.

For annotating the pressure's scale at surface pressure plots, the non-dimesional pressure coefficient has been used:

$$C_p = \frac{p}{\frac{1}{2}\rho U^2} \quad (6.3)$$

A frequency analysis was done to find the frequencies present in C_D and C_L . The power spectral density plots are calculated with the use of Burg's method. This command was used:

```
%ORDER =    ;           % order of AR model, 20 or 100 is used
%FREQUENCY= 0:0.01:10; % vector of frequencies of interest
%FS = 100;           % Sampling frequency = 100 Hz
pburg(X,ORDER,FREQUENCY,FS)
```

The autoregressive order of the Burg analysis is supposed to be calculated by a separate order analysis (e.g. AIC criteria), but as this command was not available in the Matlab software used (“System Identification Toolbox” missing), the order has been set by trial and error instead. When having plots with many frequencies, a higher order was needed to see the different frequencies. The order used is remarked on all frequency plots.

6.4 Z-direction meshing

A sensitivity analysis has been performed to evaluate the appropriate meshing in the z-direction. The z-meshing of the model has influence on the turbulence model. If laminar flow was used, only one element in the z-direction would have been sufficient. Since the turbulence model could not be activated using only one element, a certain number of elements and length in the z-direction was needed. The eddy viscosity is automatically set to zero at walls, meaning that there is no turbulence there. It was therefore unknown how the eddy viscosity boundary condition affected the results, and a mesh study of this parameter was needed.

Six different models were made. The mesh in the x-y plane is identical for all models, as shown in figure 6.4. The boundary layer mesh is quite coarse with a near-wall resolution of 20mm. This was chosen to minimize computer time. The models have 8310 elements in the x-y plane. The total number of elements is found by multiplying with the z-direction number of elements. The calculation time for these models was from 2.5 hours to 22 hours.

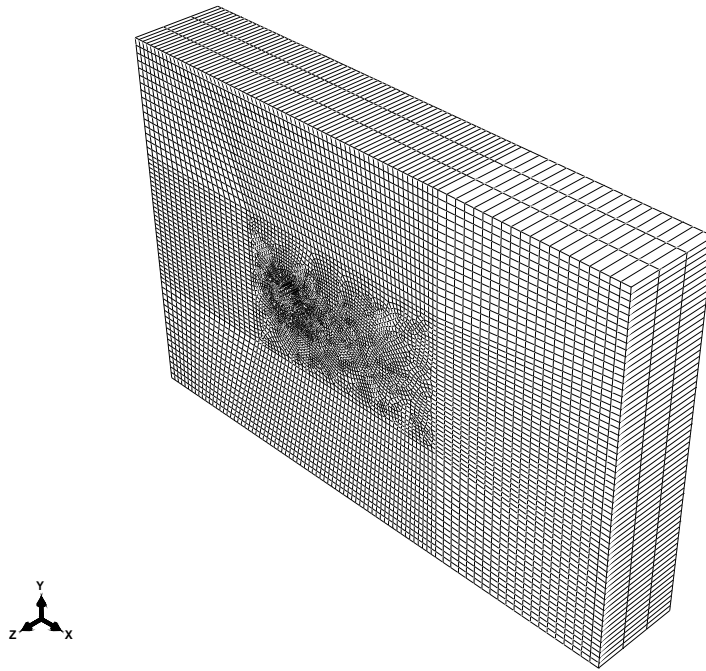


Figure 6.3: 3D model meshing (Model No.5).

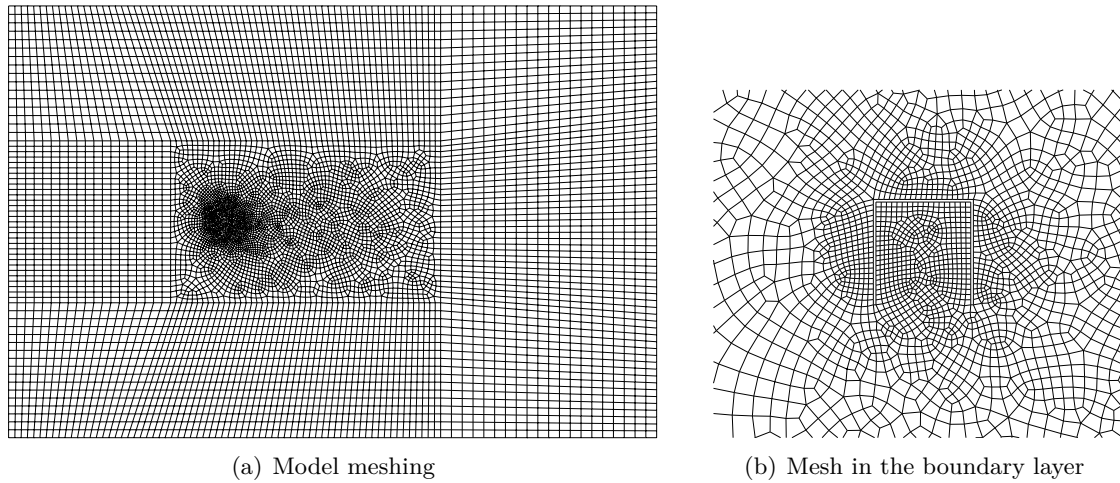


Figure 6.4: The x-y mesh in the model used to evaluate the z-length significance

6.4.1 Model No. 1: 0.4m length and 2 elements

The first model testet had a z-length of 0.4 m with 2 elements in the z-direction. As seen in figure 6.5, the lift and drag are showing unsteady behaviour, and the frequency spectrum of drag is showing a lot of different frequencies other than the expected f_s and $2f_s$.

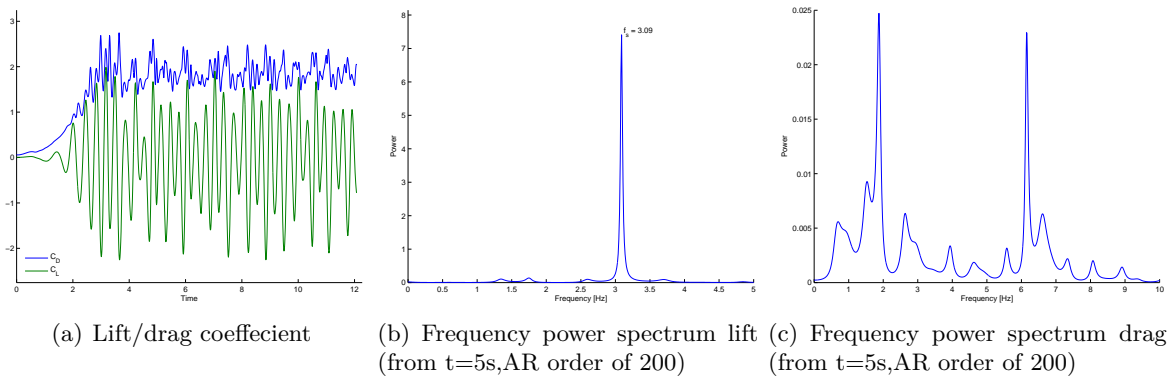


Figure 6.5: Model with z-length 0.4m made up by 2 elements of 0.2m.

6.4.2 Model No. 2: 1m length and 5 elements

The second model testet had a z-length of 1 m with 5 elements in the z-direction. As seen in figure 6.6, the lift and drag are showing a more regular pattern than model in no.1. The frequency spectrums are showing the expected frequencies at f_s and $2f_s$.

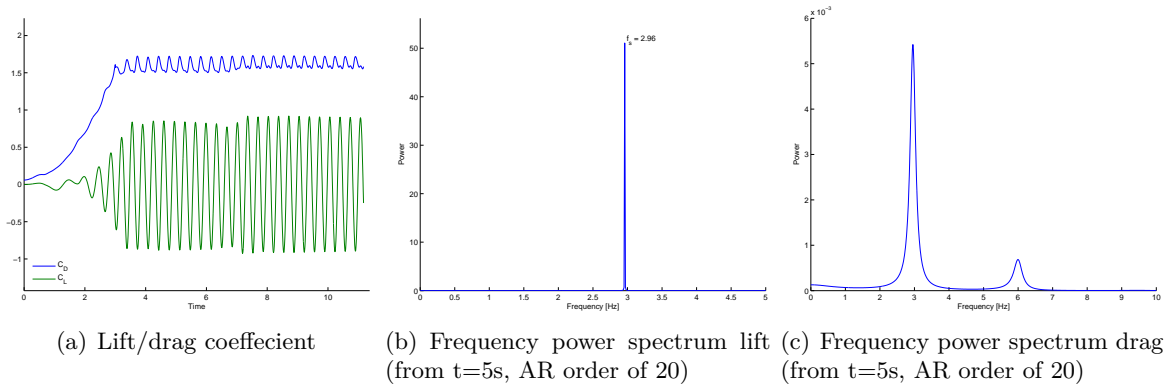


Figure 6.6: Model with depth 1m made up by 5 elements of 0.2m.

6.4.3 Model No. 3: 2m length and 10 elements

The third model testet had a z-length of 2 m with 10 elements in the z-direction. As seen in figure 6.7, the lift and drag show an even more harmonic pattern than in model no.2. The mean level of drag is about the same as in model no.2, but the amplitude of the lift oscillation has reduced. The vortex shedding frequency has reduced compared to model no. 2. The drag frequency spectrums are not showing the expected frequency at $2f_s$.

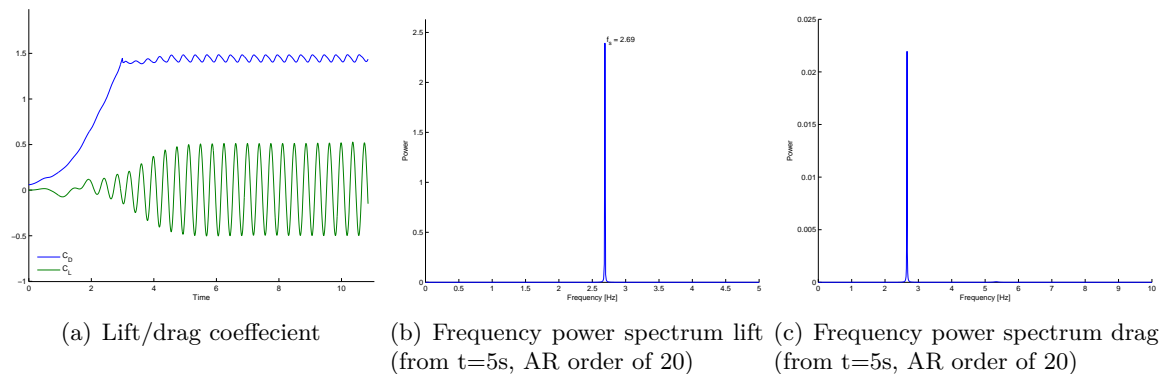


Figure 6.7: Model with depth 2m made up by 10 elements of 0.2m.

6.4.4 Model No. 4: 2m length and 5 elements

The fourth model testet had a z-length of 2 m with 5 elements in the z-direction. This was chosen to evaluate if it was the length of 2m or the number of elements that were most significant, hoping that less than 10 elements would be sufficient. As seen in figure 6.8, the drag is at the same level as for model no. 3, but the lift amplitude has increased. The vortex shedding frequency is close to identical compared to model no. 3. The drag frequency spectrums are not showing the expected frequency at $2f_s$.

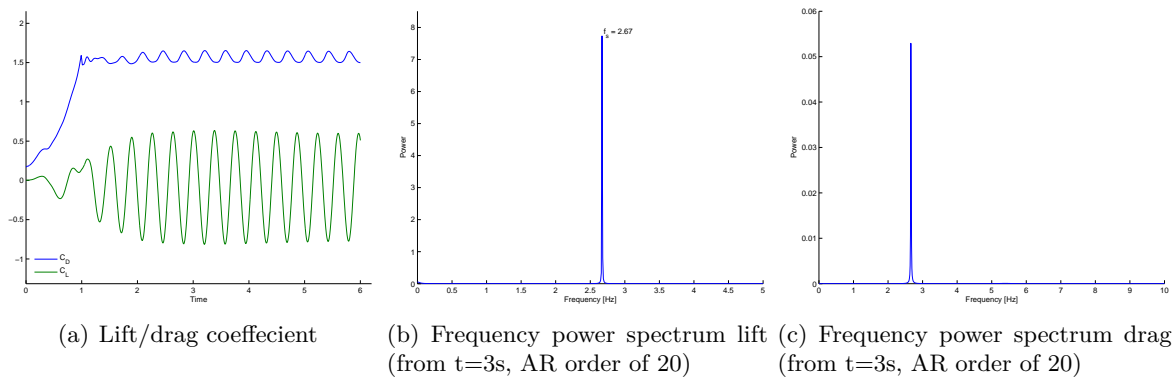


Figure 6.8: Model with depth 2m made up by 5 elements of 0.4m.

6.4.5 Model No. 5: 2m length and 3 elements

The fifth model testet had a z-length of 2 m with 3 elements in the z-direction. As seen in figure 6.9, the drag is at the same level as model no. 4, but the lift amplitude has increased. The vortex shedding frequency has also increased.

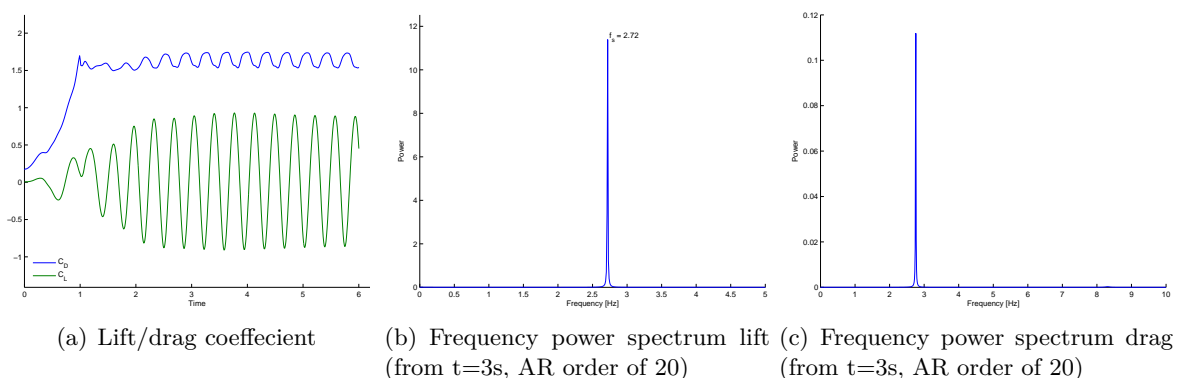


Figure 6.9: Model with depth 2m made up by 3 elements of 0.67m.

6.4.6 Model No. 6: 3m length and 5 elements

The sixth model testet had a z-length of 3 m with 5 elements in the z-direction. A comparison between model no.6's results in figure 6.10 and model no.4's in figure 6.8, leads to the conclusion that the results from the two models are close to identical.

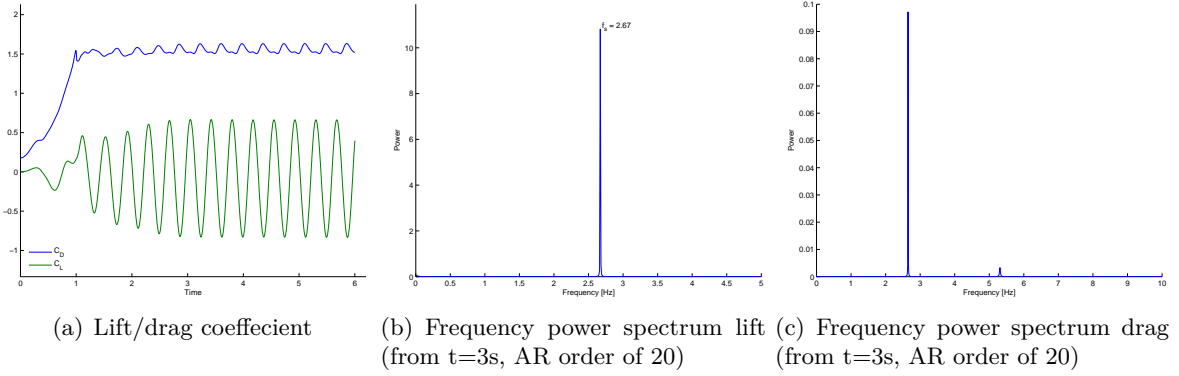


Figure 6.10: Model with depth 3m made up by 5 elements of 0.6m.

6.4.7 Summary - z-direction meshing

Model No.	Z-length	Elements	$\overline{C_D}$	$\overline{C_L}$	$\overline{C_{L,max}}$	$\overline{C_{L,min}}$	f_s	S_t
1	0.4m	2	1.87	-0.06	1.28	-1.45	3.09	0.155
2	1m	5	1.60	0.00	0.87	-0.89	2.96	0.148
3	2m	10	1.44	0.01	0.51	-0.50	2.69	0.135
4	2m	5	1.56	-0.06	0.62	-0.80	2.67	0.134
5	2m	3	1.64	0.06	0.90	-0.89	2.72	0.136
6	3m	5	1.55	-0.06	0.66	-0.83	2.67	0.134

Table 6.4: Summary of the results from the z-length and z-number of elements study.

Table 6.4 notations:

$\overline{C_D}$ - Mean drag

$\overline{C_L}$ - Mean lift

$\overline{C_{L,max}}$ - Mean maximum amplitude of lift

$\overline{C_{L,min}}$ - Mean minimum amplitude of lift

All the results are summarized in table 6.4. The results can not be judged to be fully conclusive since all parameters have not converged for 2 or more models. The main parameter used in the study was however f_s , and for this parameter it is shown a convergence of the results between model no. 3, 4, and 6. If the mean drag is evaluated next, it is seen identical results for model 4 and 6. Convergence is therefore seen in terms of the z-length. Regarding the number of elements, convergence for all parameters is not seen. To achieve a more conclusive convergence, more elements in the z-direction should probably have been tried. A conclusion was however required to be made, and it was decided to use the parameters from model no. 4, namely a z-length of 2 meters with 5 elements in the z-direction.

6.5 Boundary layer meshing

6.5.1 Recommended near wall mesh density

The next step in the sensitivity analysis was looking at the boundary layer meshing around the U-section. This is the most important mesh parameter. The criticality of the boundary layer meshing is illustrated by figure 6.11. The number of grid points in the boundary layer determines the shape of the velocity profile and the computed thickness of the boundary layer.

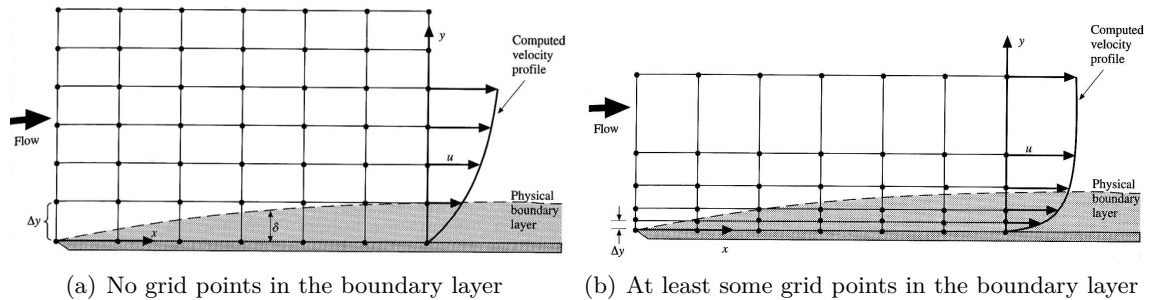


Figure 6.11: The velocity profile for viscous flow over a flat plate [Anderson, 1995].

When evaluating the boundary layer mesh, it is often referred to a non-dimensional wall distance y^+ . This is given as

$$y^+ = \frac{u_* y}{\nu} \quad (6.4)$$

where y is the distance to the nearest wall, ν is the local kinematic viscosity of the fluid. And u_* is the friction velocity at the nearest wall given by

$$u_* = \sqrt{\frac{\tau_w}{\rho}} \quad (6.5)$$

where τ_w is the wall shear stress and ρ is the fluid density at the wall.

The wall shear stress can be written as [Schlichting and Gersten, 2000, p.154]:

$$\tau_w = \mu \left(\frac{\partial u}{\partial y} \right)_w \quad (6.6)$$

The Abaqus documentation [2010] suggests an y^+ of approximately 3: “The Spalart-Allmaras model can provide very accurate boundary layer results if the near-wall region is resolved (near-wall resolution such that the nondimensional wall distance is approximately 3). However, the implementation of boundary conditions for the Spalart-Allmaras model in Abaqus/CFD permits the use of coarser meshes as well”.

The expressions from equation 6.5 and 6.6 are inserted into equation 6.4, and the equation is solved for y , giving:

$$y = \frac{y^+ \nu}{\sqrt{\nu \left(\frac{\partial u}{\partial y} \right)_w}} \quad (6.7)$$

For an estimation of the velocity gradients, analytic formulas for a flat plate at laminar flow is used [Schlichting and Gersten, 2000, p.31]. The boundary layer thickness for a flat plate is given by

$$\delta_{99}(x) = 5 \sqrt{\frac{\nu x}{U_\infty}} \quad (6.8)$$

Inserting the kinematic viscosity of air ν and $U=8\text{m/s}$ the function is plotted as shown in figure 6.12.

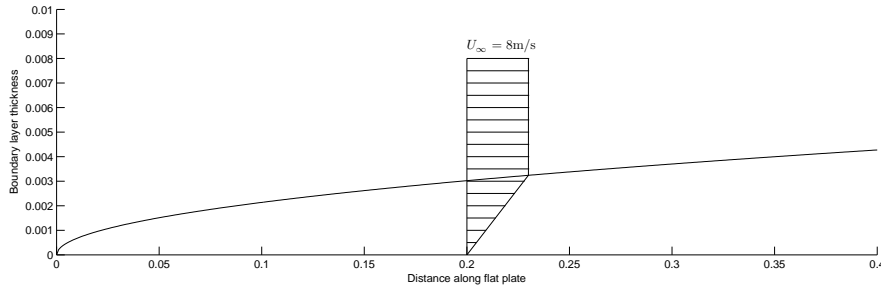


Figure 6.12: The boundary layer over a flat plate at laminar flow, $U=8\text{m/s}$.

The corresponding simplified linear velocity gradient $\partial u / \partial x$ is plotted in figure 6.13.

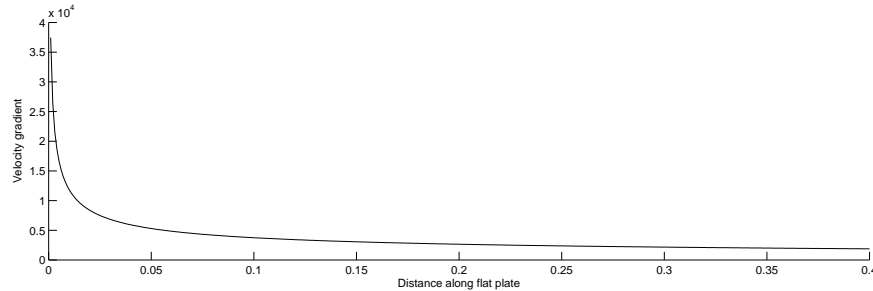


Figure 6.13: The velocity gradients over a flat plate at laminar flow, $U=8\text{m/s}$.

As seen in figure 6.13, the velocity gradients vary between approximately 37000 at $x=0\text{m}$ and 1900 at $x=0.4\text{m}$. The corresponding near wall mesh density according to $y^+ \approx 3$ is 0.06mm at $x=0\text{m}$ and 0.27mm at $x=0.4\text{m}$.

It was seen that the recommendations from Abaqus documentation [2010] were very tough to fulfill. As the models with 20mm near wall mesh took around 5 hours calculating 6 seconds, the consequence of using a 100 times finer mesh would assumingly be calculation times far exceeding the available time for this project. Instead a mesh refinement study was done with a coarser mesh.

6.5.2 Model no.7 - Near wall resolution of 5mm

The first model made with a refined mesh has a near-wall resolution of 5mm. In addition the mesh at the outer edges is made coarser than in the z-length study. At the outer edges the element size is 0.5m in this model. The element size is gradually reduced by using an unstructured meshing technique until the last 5 cm around the U-section where a structured mesh is used. A growth factor of 1.2 is used to increase the mesh size from the wall and out. The model has a total of 70210 elements. The mesh is shown in figure 6.14.

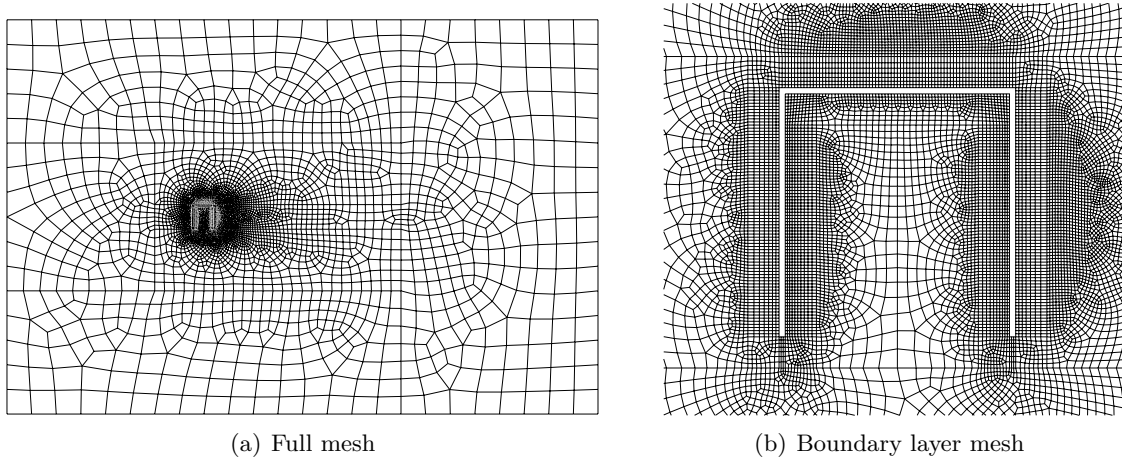


Figure 6.14: The mesh of model no. 7. The boundary layer mesh has a near-wall resolution of 5mm.

The analysis was set to calculate 7 seconds of time, where the first second was used to gradually increase the velocity from zero to 8m/s. The calculation time for this model was 4 days and 20 hours, giving a calculation speed of 1.4 seconds per day.

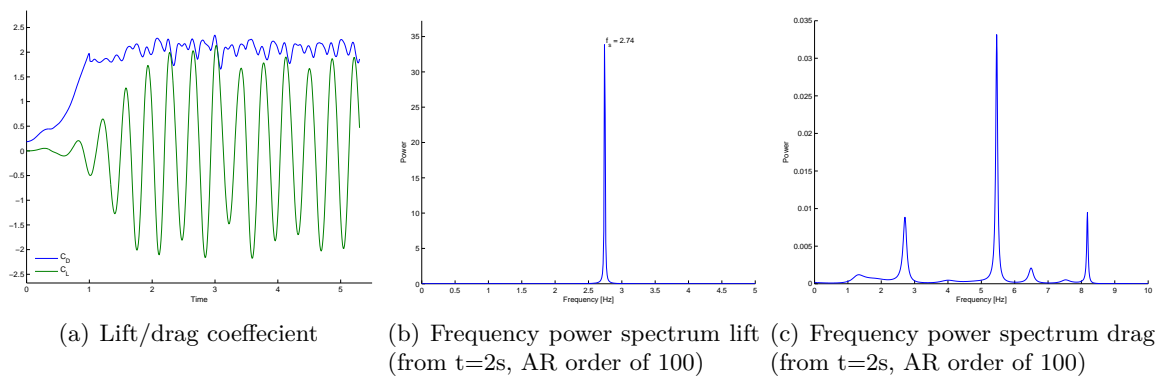


Figure 6.15: Refined mesh in the boundary layer with a near-wall resolution of 5mm.

The results from the analysis, ref figure 6.15 and table 6.5, shows a change in several parameters compared to the previous models with a near-wall resolution of 20mm. The mean drag and the lift amplitude have increased significantly compared to model no.4, while the

vortex shedding frequency f_s has a slight increase. While the drag frequency spectrum of model no.4 did not show the frequency at $2f_s$, this frequency is very clear in this model and is seen to be the dominating frequency of the drag. Alltogether the difference between 20mm and 5mm near wall resolution is seen to be significant. In addition it is seen, just from looking at the drag plot, that the drag looks more “turbulent” than the plot from model no. 4 did. This is taken as a positive sign believing that the mesh refinement has led to the turbulence model having more effect.

6.5.3 Model no.8 - Near wall resolution of 1mm

As the difference between the results from 5mm to 20mm near wall resolution was significant, a further refinement of the near wall mesh was done. This was done with some concern regarding the calculation time, as it was expected to increase significantly. The near wall mesh of the model is shown in figure 6.16, while the meshing in the regions far from the U-section is just as in figure 6.14(a). The meshing technique is similar as to model no. 7, with a mesh growth factor of 1.2 in the structured zone from the wall and out. The model has a total of 133810 elements.

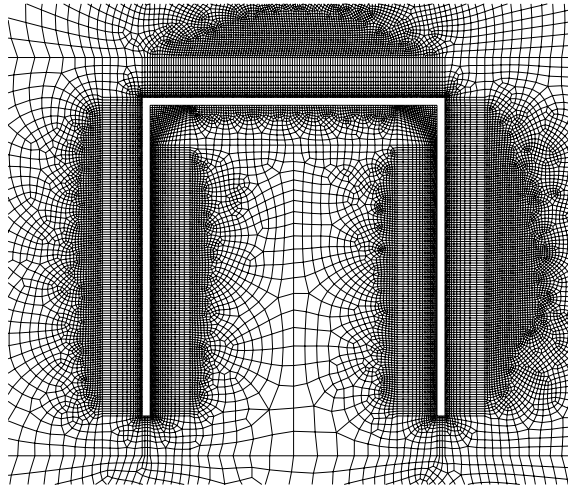


Figure 6.16: The near wall mesh of model no. 8. The boundary layer mesh has a near-wall resolution of 1mm.

The analysis was set to calculate 7 seconds of time, where the first second was used to gradually increase the velocity from zero to 8m/s. The analysis was unfortunately disrupted at around 3.5 seconds by a power failure. At that time the calculation had run for 7 days and 14 hours, meaning a progress of 0.46 seconds per day. If the analysis had not been stopped, it would have run for over 15 days. Even if a shorter period than intended was solved for the analysis, there were enough results, and it was considered unnecessarily to run the analysis again.

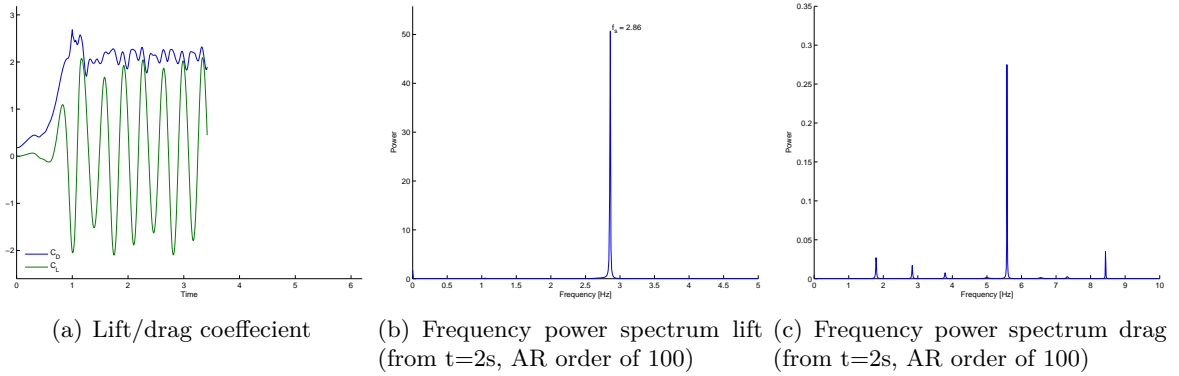


Figure 6.17: Refined mesh in the boundary layer with a near-wall resolution of 1mm.

The results from the analysis, ref figure 6.17 and table 6.5, shows only small differences compared to model no. 7. The mean drag is only a few digits higher. The amplitude of the lift is also very close, but a positive mean lift has been introduced. The difference in the mean lift is however not to be trusted, considering the short period which the mean lift is calculated for. If the analysis had run for the same period as model no.7, the results could likely be different. Not all parameters are identical. The vortex shedding frequency has increased slightly, from 2.74 to 2.86 and the $2f_s$ frequency of the drag looks even stronger than in model no.7.

6.5.4 Summary - Boundary layer meshing

Model No.	Near wall spacing	$\overline{C_D}$	$\overline{C_L}$	$\overline{C_{L,max}}$	$\overline{C_{L,min}}$	f_s	S_t
4	20mm	1.56	-0.06	0.62	-0.80	2.67	0.134
7	5mm	2.08	0.01	1.88	-1.92	2.74	0.137
8	1mm	2.11	0.10	2.01	-1.85	2.86	0.143

Table 6.5: Summary of the results from boundary layer meshing study

When evaluating the results from model no.7 and no.8, the models are seen to give very similar results. The drag and lift levels can be considered identical, and only a small deviation in the vortex shedding frequency is found. Convergence between the models are therefore seen for most parameters and only the frequency seems to deviate. The deviation between the models is around 4% for this parameter, which is not a substantial number.

To validate the results further, it is compared to values from Eurocode. The relevant values found in Eurocode are tabulated in table 6.6. Values for an U-section could not be found, so instead the comparison is done to similar sections.

Section type	C_D	S_t
Rectangular (d/b=1)	2.0	0.12
I-section (d/b=1)	2.0	0.14

Table 6.6: Drag coefficient and Strouhal number for relevant cross sections [Eurocode-1, 2005].

The Strouhal numbers calculated are seen to be identical to the Strouhal number of an I-section, while higher than the Strouhal number of a rectangular section. A result in the middle of these two would have been expected, but as no documentation is found regarding what Strouhal number of an U-section it is difficult to say if the Strouhal number found is correct or not. The expected mean drag is 2.0 for all sections, and the mean drag calculated is thereby just slightly higher with a deviation of 4-5.5%. It is also seen that model no.4 with a near wall mesh of 20mm did not produce accurate calculation of the drag coefficient compared to design codes.

Alltogether only small deviations are found to the Eurocode values, and the results are therefore evaluated to be very good. Because of the good results from these two models, it was considered unnecessarily to decrease the near-wall mesh size further. The conclusion made is that a near-wall mesh size of 5mm is sufficient for the parameters being studied.

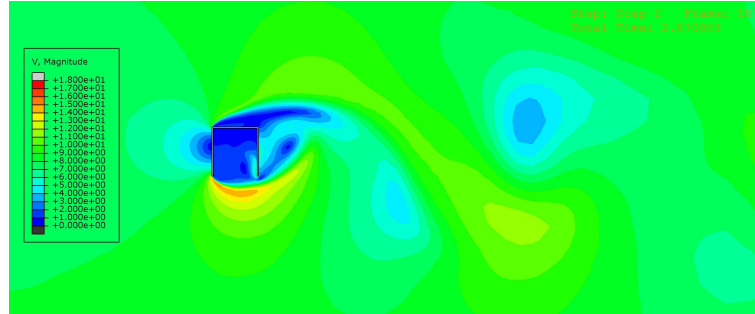
The mesh chosen is a lot coarser than the recommended value of $y^+ \approx 3$. In terms of y^+ the mesh density of 5mm corresponds to a y^+ in the range of 60 to 250 for the flat plate boundary layer (figure 6.12). The model is therefore not expected to solve all the details of the flow, but very good results has been achieved for the mean drag and the vortex shedding frequency. These parameters are also the parameters of primarily interest in these analyses.

Chapter 7

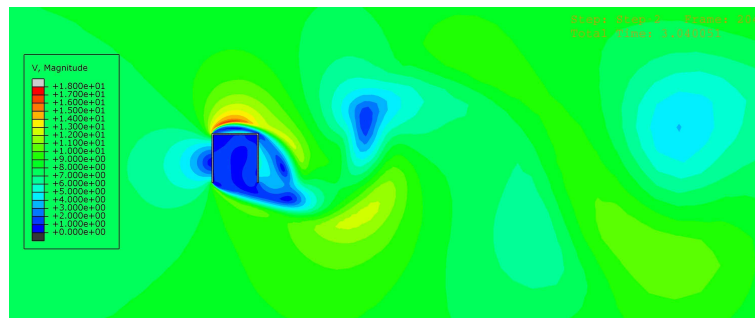
CFD Results

7.1 CFD model of original U-section

The original U-section model will in this section be further evaluated. The model with the chosen mesh density from the boundary layer meshing study, namely model no.7, will be used for this purpose. The modelling of this model and main results like drag and lift coefficients have already been presented in section 6.5.2. In this section the observations seen in flow plots and pressure plots will be discussed. Two points of time at minimum and maximum lift are chosen for further study. At $t=2.87\text{s}$ a minimum is found where C_L has a value of -2.11 . At $t=3.04$ there is a maximum where C_L has a value of 2.13 .



(a) At $t=2.87\text{s}$, $C_L=-2.11$



(b) At $t=3.04\text{s}$, $C_L=2.13$

Figure 7.1: Velocity contour plots of the wake

To evaluate the results it is useful to compare to some expected flow characteristics from the theory of fluid mechanics [Versteeg and Malalasekera, 2007, p.301]:

- Fluid flows from high to low pressure
- Static pressure decreases when velocity increases (Bernoulli's theorem for inviscid flows)
- The speed of the fluid near the wall is smaller than the speed further away from the wall (boundary layer formation)
- Boundary layers rapidly separate under the influence of an adverse pressure gradient. (Pressure increases in the direction of flow outside the boundary layer)
- Flows will separate at corners
- If a flow separates there is always recirculation

The characteristic vortex trail is clearly spotted at figure 7.1a and figure 7.1b. At $t=2.87s$, the velocity is at maximum underneath the U-section, creating a negative pressure at the inside of the section resulting in a net downforce. At $t=3.04s$, the velocity is at maximum above the U-section, creating a negative pressure at the top of the section resulting in a net upforce. The decrease in pressure when velocity increases is just as Bernoulli's theorem predicted.

The alternating vortex shedding is also clearly spotted when comparing the velocity vector plots at C_L, min and C_L, max . At figure 7.2a, a counterclockwise vortex is seen to form, while at figure 7.3a a clockwise vortex is seen. The fundamental behaviour of vortex shedding is therefore found, namely vortices forming with alternating directions at the back of the body.

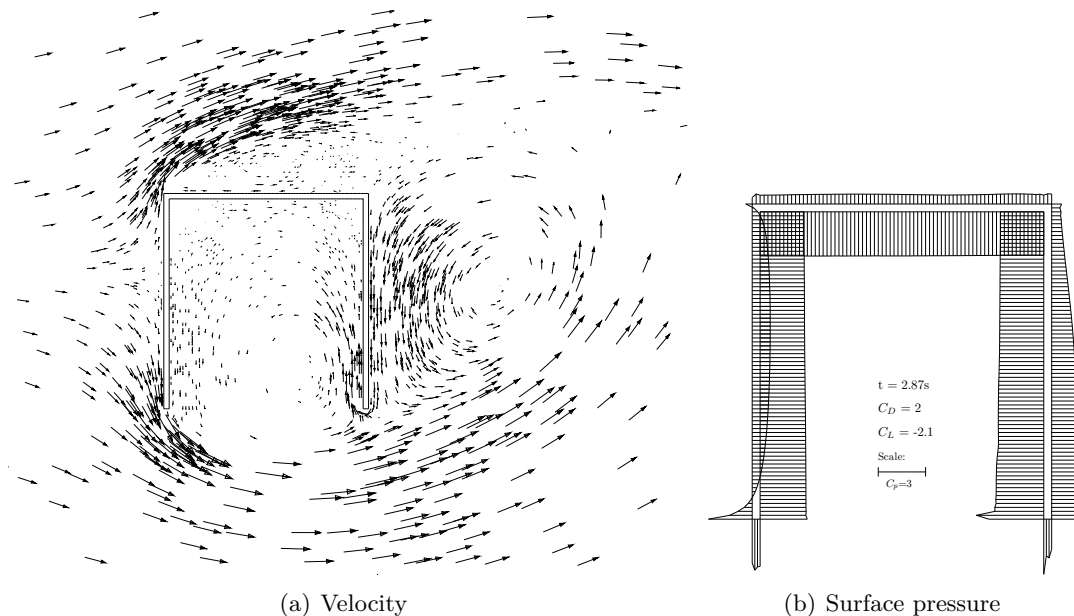


Figure 7.2: Velocity and surface pressure at $t=2.87$, $C_L=-2.11$

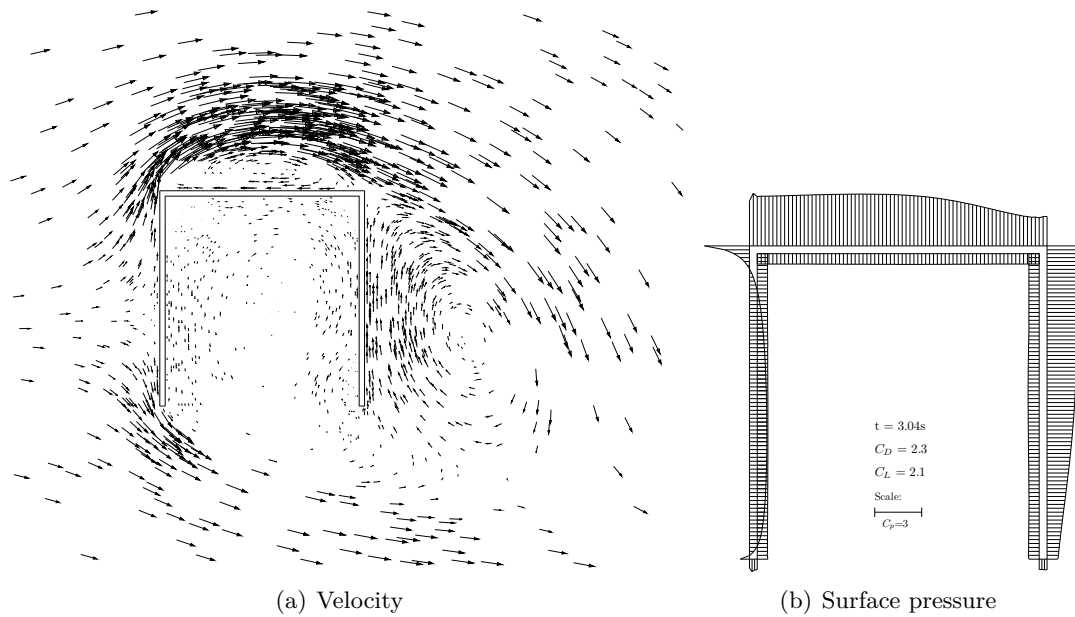


Figure 7.3: Velocity and surface pressure at $t=3.04$, $C_L=2.13$

Looking at figure 7.2a and figure 7.3a, separation is clearly seen for both velocity plots at the upper and lower front corner. The corresponding adverse pressure gradient is also seen at the pressure plots. Above the top flange, recirculation is very clear at figure 7.3a. At figure 7.2a, recirculation is also seen, but the velocities are smaller. Corresponding to the lower front separation, a recirculation swirl as big as the inside of the U-section is seen in both figures, but this swirl is strongest at figure 7.2a.

When comparing the flow directions to the pressure behind the section, it is seen that the air is flowing from high (less negative) to low (more negative) pressure on both figures, just as the theory stated.

Alltogether the model's capability of calculating important flow characteristics like separation and recirculation seems satisfactory. The flow around the U-section seems to be in good agreement with the theory of fluid mechanics, and many details of the flow have been captured. The vortex shedding problem of the original light mast is clearly confirmed, as the characteristics of vortex shedding has been found in this model.

7.2 CFD model of U-section with installed countermeasure

The light mast was as mentioned in chapter 3 equipped with aerodynamic countermeasures to prevent the vibrations. The measures installed were two DN100 pipes, with a outer diameter of 114mm installed above and below the u-section. The intentional function of these flaps is to round off the corners of the cross-section and introduce a positive Reynolds number effect. The 25 mm gap between the pipe and the U-section is designed to allow the wind to bleed through the section and thereby counteract the formation of vortices [Bessason and Snaebjörnsson, 2008]. The measured maximum amplitude of motion was reduced from 6.4 cm prior to installation to 1.5 cm after the wind flaps were installed.

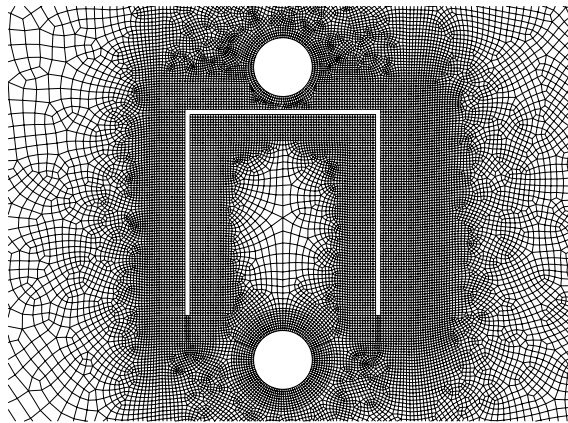


Figure 7.4: The mesh of the wind-flaps model.

A CFD model was built up based on engineering drawings, see attachment F. The near-wall mesh is shown in figure 7.4. The CFD model consists of 149790 elements. The analysis was set to calculate a period of 11 seconds, where the first second was used to increase the wind velocity from zero to 8 m/s. The calculation time for this analysis was 12 days, meaning a progress of 0.9 analysis-seconds per day.

The lift and drag coefficients as presented in figure 7.5 are showing promising results in terms of countermeasuring VIV, just as the live case predicted. A first sight the lift shows an initial vortex-shedding response starting at $t=1s$ which dies out in a couple of seconds. From $t=4s$ and on no regular vortex shedding activity is spotted. The drag stabilizes at around 1.5 which is a lower level than for the u-section without flaps. This is at first sight maybe somewhat surprising since the total projected area has increased by 57%, but this is judged as a sign on reduced separation.

The successful prevention of vortex shedding is also seen by studying the wake after the initial vortex shedding has died out. At $t=7s$ a long stable wake is seen, ref figure 7.6. It is also observed that the U-section with the pipes seem to act as only one body considering the wake. According to Blevins [1990, p.48], cylinders positioned over a flat plate is not affected by the plate if the spacing between the cylinder and the plate is bigger than 0.5 diameters of the cylinder. The spacing in this case is 0.2 diameters. If the spacing between the U-section and the pipe had been too big the pipe would have developed it's own vortex shedding activity.

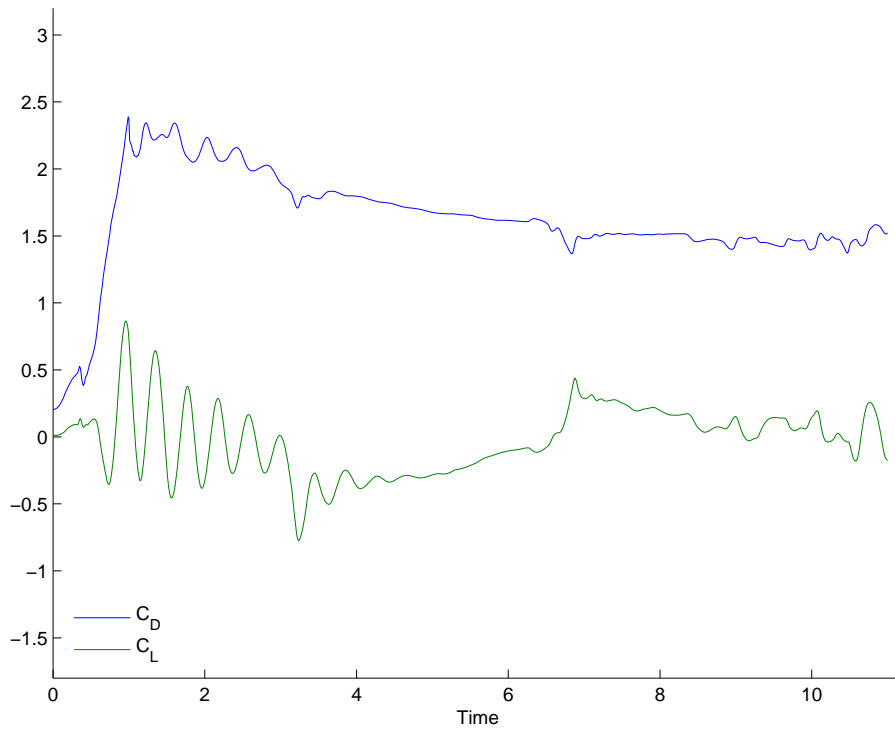


Figure 7.5: Drag and lift coefficients for the model with wind flaps.

The frequencies of the pipe would then had been introduced. The structure would probably still be exposed to VIV but the amplitude would possibly have been reduced because of the broader response spectrum.

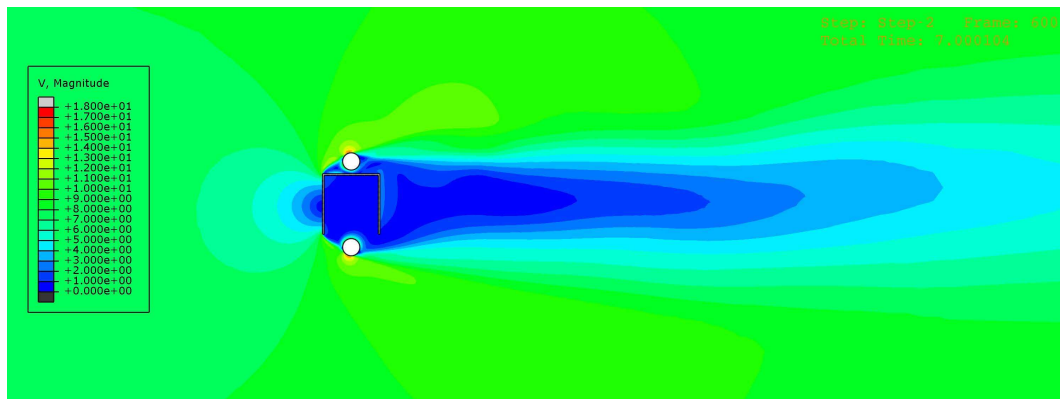


Figure 7.6: Velocity plot of the wake at t=7s

A point in time at t=7s is chosen for a detailed study of the flow, and plots are presented for velocity and surface pressure at figure 7.7. Since no distinguished regularity is seen in the lift coefficient at figure 7.5 this point is picked quite arbitrary. More plots are presented in appendix B.

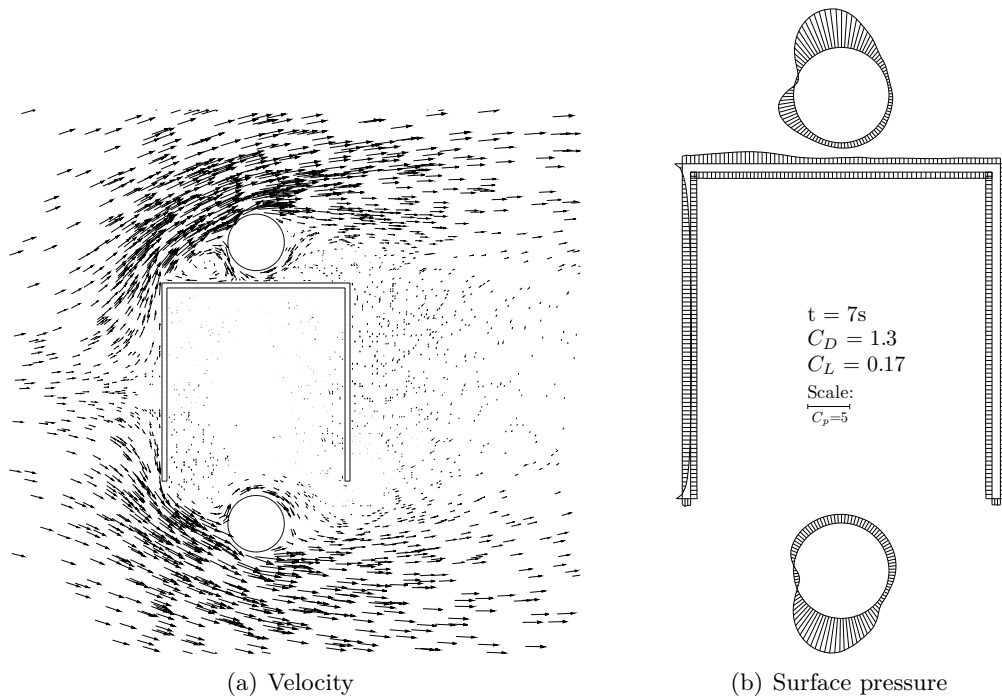


Figure 7.7: Velocity and surface pressure at $t=7s$

The flow at the front corners looks quite similar to what was observed in the model of the U-section alone. At the top front corner, a recirculation swirl can be spotted. This is due to the separation at the top front corner. At the bottom front corner, strong separation is also seen. When looking closely a low velocity swirl filling the inside of the section is observed. These recirculation swirls are just as observed at figure 7.2 and figure 7.3.

When studying the flow around the pipes it is seen that the purpose of the 25mm gap between the U-section and the pipe is fulfilled. The flow is bleeding through the gap, and the flow is seen to curve nicely around the pipe before the flow from each side is merging together again behind the pipe. The effect of this is that no vortices are generated in the wake of the pipes. The wake is therefore very stable, as figure 7.6 also shows.

Mild separation of the flow from each direction is seen at the back of the pipes. Adverse pressure gradients in the flow directions are confirming this. A tiny recirculation swirl is probably present between the two separation points, but this is not indicated by the velocity plot. The separation from the pipe is however not seen to introduce any vortex shedding.

The main reason for the positive effects introduced by the installed countermeasure is that the flow is separating at the pipes instead of at the back of the U-section. Since the flow is bleeding through the gap, flow from both sides meets at the back of the pipe countermeasuring vortex generation. An additional benefit of the installed flaps is that drag on the cross section has decreased due to the more streamlined shape and the reduced separation.

Alltogether, the CFD analysis of the wind flaps is seen to locate the VIV countermeasuring effect predicted from the live case. The desired flow effects planned for in the design of the wind flaps has been found, and through the CFD analysis more understanding is achieved about why this is a successful VIV countermeasure.

7.3 Alternative No.1 - Flat plate flap

Two alternative suggestions to VIV countermeasures have been evaluated. The first one is a flat plate 180x10 mm placed 75mm above the U-section flange. The flat plate is tested to see how this will disturb the flow on top of the U-section, and hopefully it will disturb some of the vortex shedding.

The model consisted of 96010 elements. The analysis was set to calculate a period of 11 seconds, where the first second was used to increase the wind velocity from zero to 8 m/s. The calculation time for this analysis was 6 days and 10 hours, meaning a progress of 1.7 seconds per day. As seen in figure 7.8 the mesh inside the section is coarser than on the outside. This was done to save elements, since the previous models had shown that the flow velocities inside the section were very low. If the velocity is lower, the boundary layer will be thicker (ref eq. 6.8), and the velocity gradients will be lower. A coarser mesh were low velocities are expected is therefore justified.

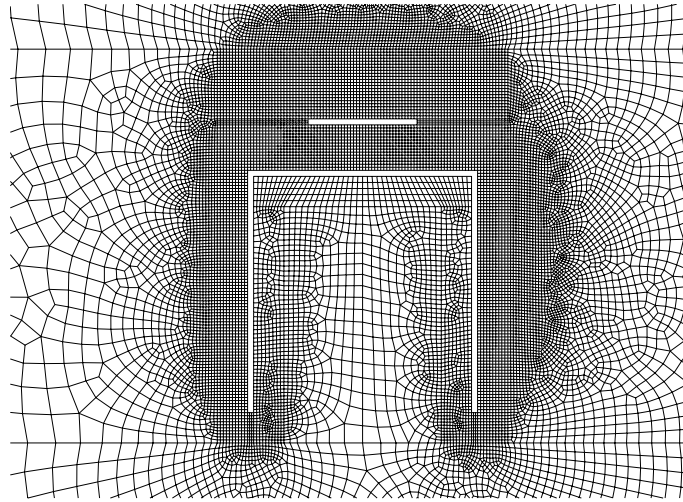


Figure 7.8: The near-wall mesh of the flat plate model.

Model	$\overline{C_D}$	$\overline{C_L}$	$\overline{C_{L,max}}$	$\overline{C_{L,min}}$	f_s	S_t
U-section	2.08	0.01	1.88	-1.92	2.74	0.137
U-section with plate flap	2.00	-0.38	0.47	-1.43	2.81	0.141

Table 7.1: Summary of the results from the plate flap model

The main results of this model are shown in table 7.1. The drag is similar to what was observed for the original U-section, and the vortex shedding frequency is also very similar. The mean lift is however deviating, and it seems like a mean negative lift has been introduced. The mean amplitude of the lift force, found by subtraction between the mean lift maximum $\overline{C_{L,max}}$ and the mean lift minimum $\overline{C_{L,min}}$ is found to be reduced from 3.8 for the U-section to 1.9 for the U-section with plate flap, meaning a 50% mean reduction in the mean lift amplitude.

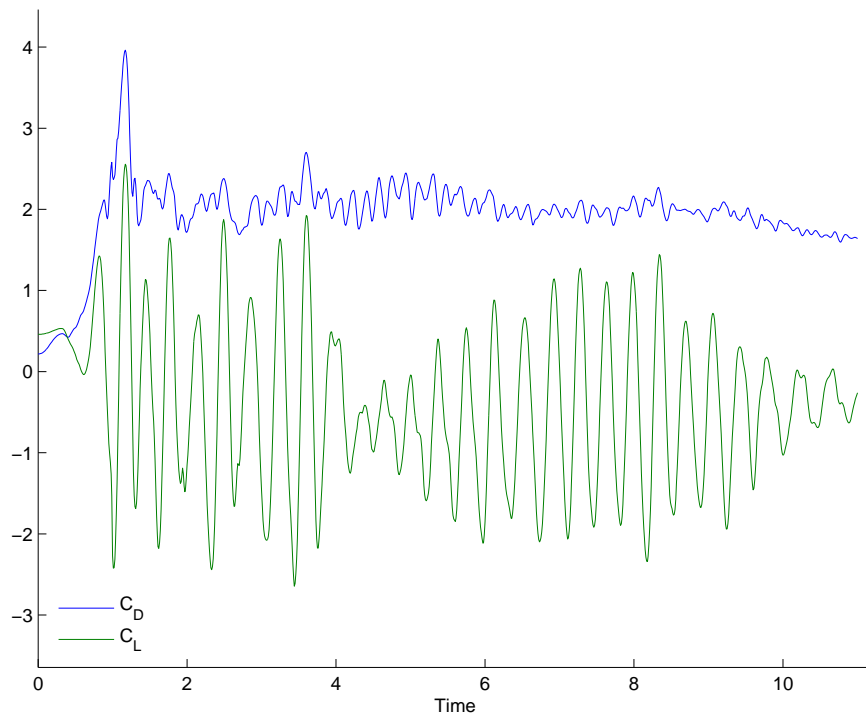


Figure 7.9: Lift and drag coefficient of the plate flap model

The lift coefficient plot of this model, as seen in figure 7.9 is showing a characteristic pattern from around $t=4.5\text{s}$ to $t=11\text{s}$. The lift amplitude seems to almost have died down at $t=4.5\text{s}$, but then gradually builds up again to a maximum at around 7-8s and then dies down again at around $t=11\text{s}$.

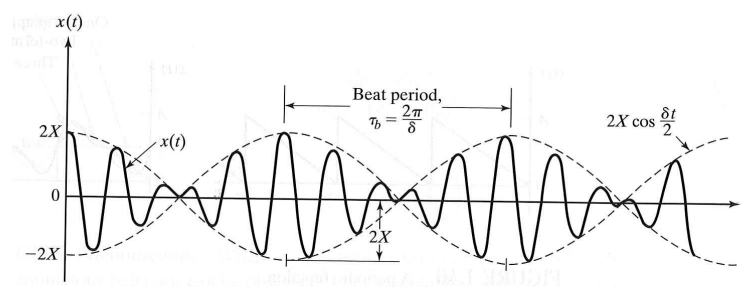


Figure 7.10: The beating phenomena [Rao Singiresu, 2004].

This phenomena is called beating, and happens when two harmonic frequencies close to one another are added [Rao Singiresu, 2004, p.52]. The beat period is seen to be around 6.5 seconds from studying figure 7.9. The beat period τ_b can be expressed as

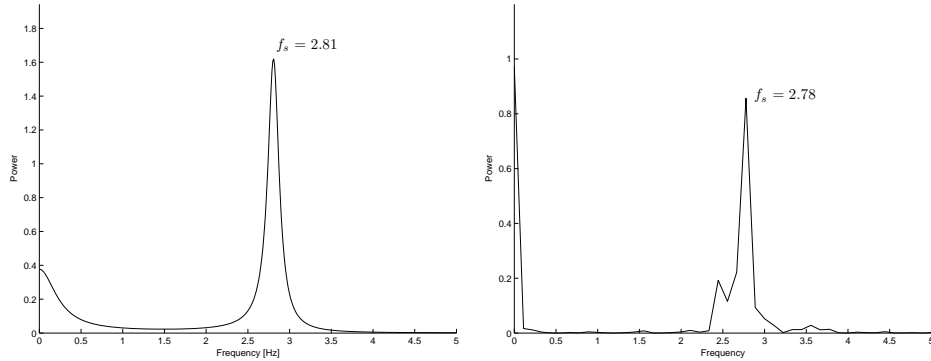
$$\tau_b = \frac{2\pi}{\delta} \quad (7.1)$$

where δ is the difference between the two harmonic motions in angular velocity. The corresponding frequency difference is found by

$$\Delta f_s = \frac{\delta}{2\pi} \quad (7.2)$$

When having a beating period of 6.5s, Δf_s is found to be 0.15Hz. According to this there should be two harmonic frequencies in this model separated by 0.15 Hz.

The frequency power spectrum of C_L is shown in figure 7.11. When performing the frequency analysis, a second frequency in the lift was expected. At first the Burg method was used, as shown in figure 7.11a. This did not show any distinct second frequency at the expected distance at either an AR order of 20 or using higher order. The Fast Fourier Transform (FFT) method was therefore tried instead, as shown in figure 7.11b. The FFT method gave approximately the same main peak frequency as the Burg method, but did in addition show a second peak at $f_s=2.44$ Hz. The difference between the two peaks is 0.34Hz. This is twice the difference calculated, but as the beating period is based on studying the plot visually and there are round offs in the frequency analysis, the difference is probably within the uncertainty range. The suspicion of two close frequencies interacting, creating the beating phenomena, therefore seems to be confirmed.



(a) Using Burg's method (from $t=2$ s, AR order of 20) (b) Using FFT method (from $t=2$ s). The second peak is at 2.44Hz.

Figure 7.11: Frequency power spectrum lift.

The drag frequency spectra was also evaluated both using both Burg's method and the FFT method, as shown in figure 7.12. As for the drag frequencies there is a lot of different frequencies present, but two peaks are seen at around 5-6 Hz indicating the corresponding drag frequencies at $2f_s$.

When summarizing the observations made and evaluating the VIV prevention capabilities of the flat plate, it is seen some quite promising results. Although vortex shedding is clearly observed in this model the irregularity introduced is positive. The beating phenomena was found, meaning that more frequencies were present in the lift force. In other words, a more broadbanded frequency response spectrum has been induced. The benefit of a more broadbanded response, is that the fluctuating force will vary randomly along the length of the beam. Thereby the probability of getting violent vibrations will be reduced. A broad banded spectrum is a commonly used avoidance criteria of VIV as e.g. published by Oppen

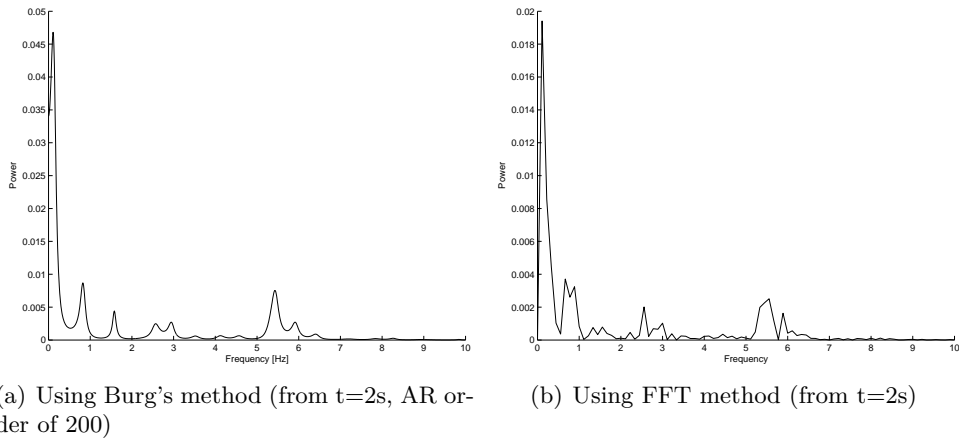


Figure 7.12: Frequency power spectrum drag.

[1995].

The flat plate flap is seen to have favorable effects that can prevent vortex shedding. It is seen that the magnitudes of the lift has reduced and a more broadband spectrum of the vortex shedding frequency has been induced. It is therefore likely to believe that vortex-induced vibrations would have been significantly reduced by installing this flap. Exactly how much the vibrations would have been reduced is however impossible to predict from a pure CFD model. To explore this further, a FSI model or a live experiment would have been necessarily.

Velocity contour and pressure plots of this model is not presented here, but can be found in appendix C.

7.4 Alternative No.2 - Square flap

The second alternative spoiling device tested is a square 40x40mm piece attached to the top flange of the U-section. The square flap will be tested to see if this device can give any positive VIV countermeasuring effects.

The model consists of 110630 elements. The analysis was set to calculate a period of 11 seconds, where the first second was used to increase the wind velocity from zero to 8 m/s. The calculation time for this analysis was 8 days, meaning a progress of 1.4 analysis-seconds per day.

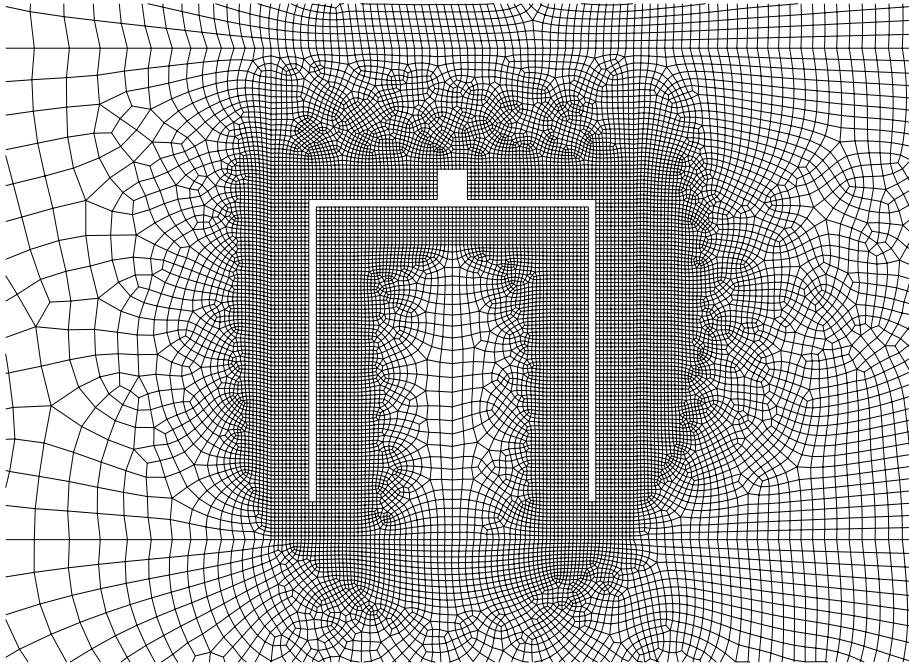


Figure 7.13: The mesh of the square flap model.

The resulting force coefficient plot, as presented figure 7.14, is showing disappointing results when it comes to countering VIV. The results, ref table 7.2, is almost identical to the results from the U-section alone.

Model	$\overline{C_D}$	$\overline{C_L}$	$\overline{C_{L,max}}$	$\overline{C_{L,min}}$	f_s	S_t
U-section	2.08	0.01	1.88	-1.92	2.74	0.137
U-section with square flap	2.04	0.02	1.95	-1.84	2.84	0.142

Table 7.2: Summary of the results from boundary layer meshing study.

When looking at the velocity plots at figure 7.15a and figure 7.16a the impression is that the 40x40mm square flap is just not big enough to alter the flow in a significant way. When comparing the velocity vector plots at figure 7.15 and 7.16 to the plots for the U-section at fig. 7.2 and 7.3 they are almost identical. The only difference made by the square is to split

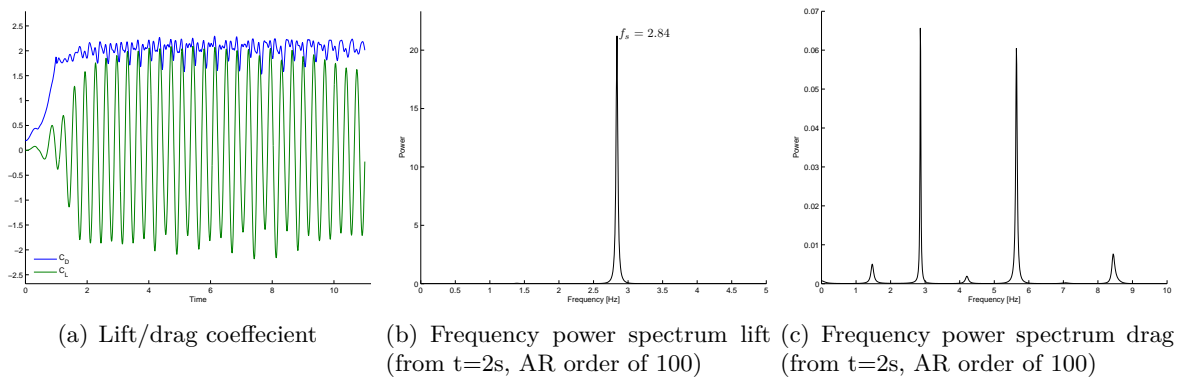


Figure 7.14: Results from the model with the square flap.

the recirculation swirl above the flange in two, but this is not seen to have any influence on the flow.

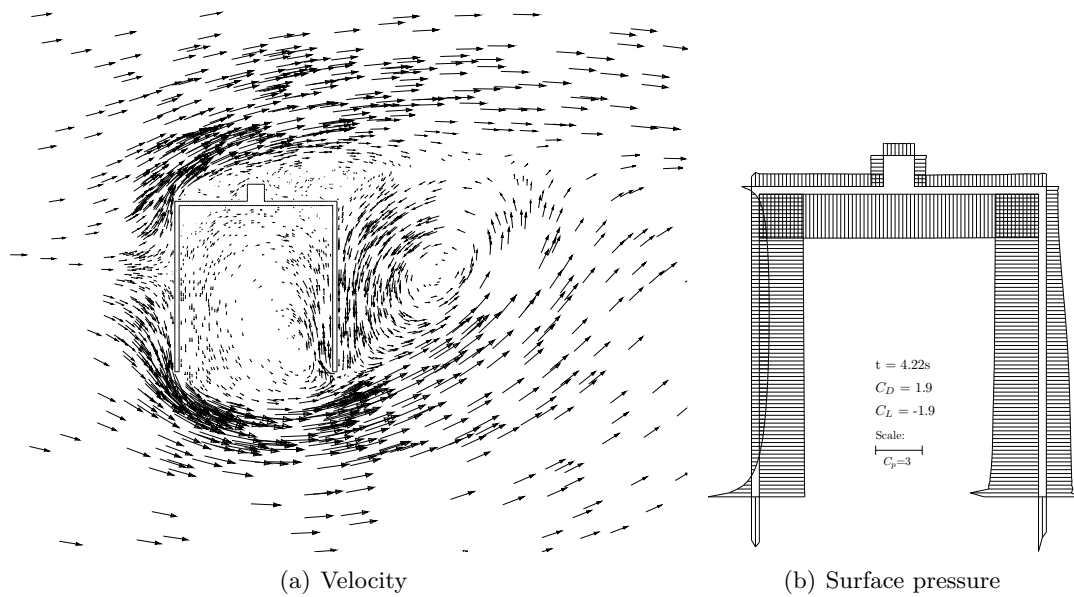


Figure 7.15: Velocity and surface pressure at $t=4.22$, $C_L=-1.9$.

The conclusion seen is that the 40x40mm square flap is not a successful VIV counter-measuring device. The square is too small compared to the section to change the flow. To change the flow, the size of the square should be increased to more than the height of the recirculation swirl above the flange. From the velocity plot (fig. 7.16a) approximately twice the size looks appropriate. The question is how succesful this would have been. As there was not enough time to modify the model and run a new analysis, this question will have to remain unanswered.

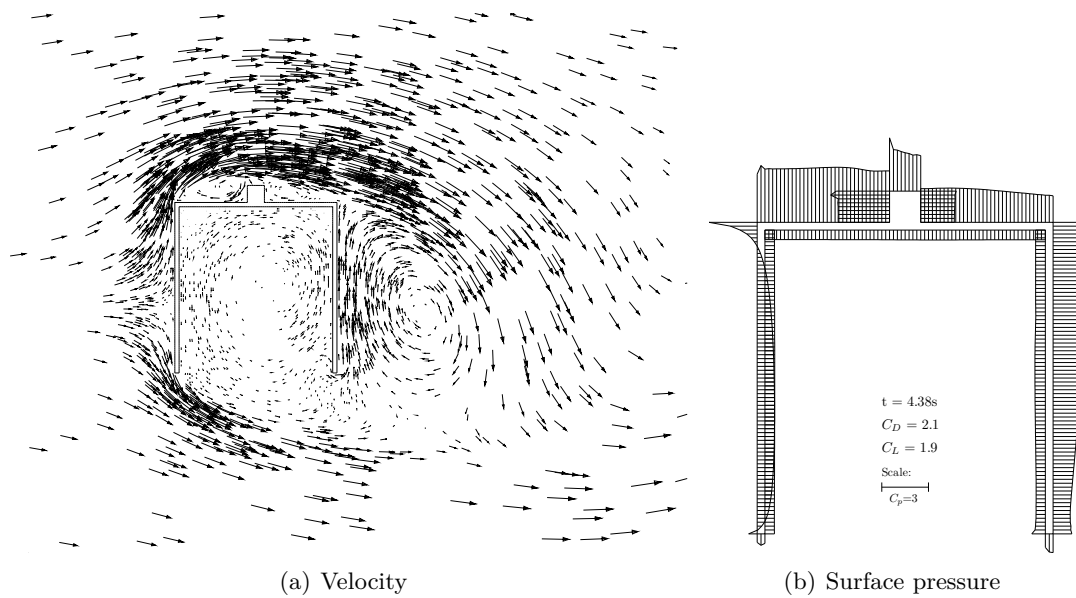


Figure 7.16: Velocity and surface pressure at $t=4.38$, $C_L=1.9$.

Chapter 8

Fluid Structure Interaction

8.1 General

A fluid structure interaction model was made in Abaqus. Abaqus 6.10 has built in support for these types of analysis. A FSI model consists of two individual models. There is one model for the flow part and one model for the structural part. These two models are then coupled during the run of a FSI-analysis. For each time step the calculated load from the CFD model is applied to the structure, and the structural response calculated by the structural analysis is in the subsequent time step applied back to the flow analysis.

8.2 FSI modelling

8.2.1 Structure modelling

The principle of the FSI-model made is illustrated in figure 8.1. A spring and a damper is specified to model the structural behaviour.

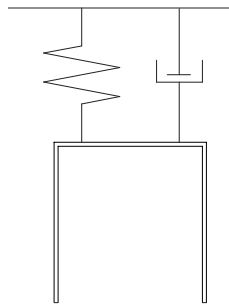


Figure 8.1: Principle sketch of the FSI model.

The modelling of the structural part consisted of a 2m long part of the U-section as shown in figure 8.2. The elements used for meshing was an eight node 3D element(C3D8R). The mesh of the structural model was quite coarse as this was not significant.

The boundary conditions of the model were set so that all degrees of freedom except displacement in y-direction were set to zero. For the y-direction, a spring stiffness k and a structural damping c was specified. As to the spring stiffness, the results from the modal

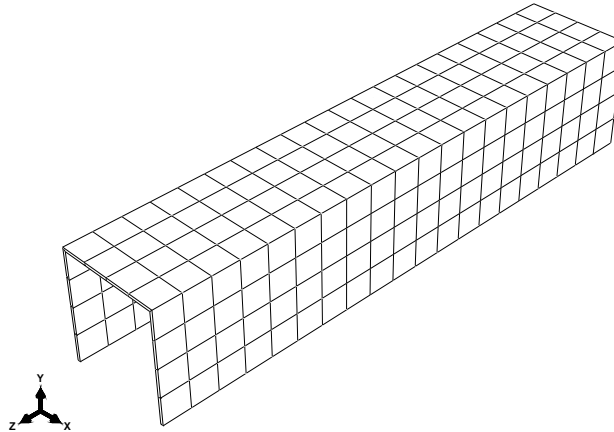


Figure 8.2: Structural model meshing

analysis was used to tune the spring. The natural frequency of the vertical cantilever mode was there found to be 2.28Hz. Several modal analysis were then performed on this model until a natural frequency of 2.28Hz was achieved. The resulting spring stiffness was $k=2.35$ kN/m. The dashpot damper was also tuned in a similar way. From Bessason and Snaebjörnsson [2008] a damping ratio ξ of between 0.5% and 1% was estimated. The dashpot damper was tuned to be $\xi=0.75$, giving $c=2.5$ Ns/m.

8.2.2 CFD modelling

The geometry of the CFD model was just as for the other models (ref. chapter 6), but the boundary layer mesh used was coarsened a bit to a near wall mesh density of 10mm. It had previously been experienced that the near wall mesh density did not influence the vortex shedding frequency dramatically and a quite coarse mesh was therefore used. The boundary conditions needed to be modified for use in a co-simulation. The wall boundary conditions around the U-section cutout needed to be removed, as this was the co-simulation interaction boundary.

8.2.3 Co-simulation setup

The procedure of a FSI analysis in Abaqus is first setting up the two individual models, and then coupling these two together specifying the co-simulation boundary. The co-simulation boundary was in the structural model set to be all outer faces of the U-section except the faces at the U-section's ends. In the CFD model the co-simulation boundary was set to be the faces of the U-section cutout. The meshing of the two models at the interaction boundary did not have to be identical [Abaqus documentation, 2010]. The wall boundary conditions at the interaction boundary was taken care of by Abaqus and needed not to be specified. In addition, a co-simulation analysis job needed to be created.

The procedure of setting up a FSI analysis in Abaqus was altogether fairly simple and user friendly.

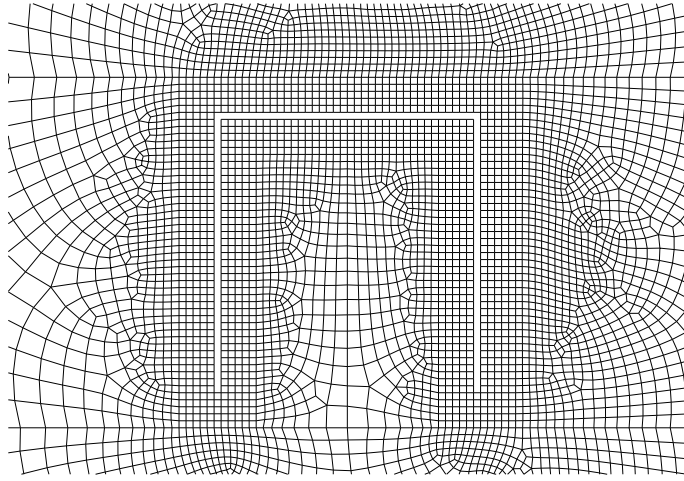


Figure 8.3: CFD model meshing.

8.3 FSI analysis failure

The analysis run of the model was then started. The iterations seemingly went on nicely for some time, but the analysis came to a failure after doing about 800 iterations. From the analysis log-file it was seen a violent increase in energy of the model. This is a sign on calculation instability.

Several attemptx were made to re-run the analysis. It was aslo tried to reduce the number of co-simulation boundaries, specifying just the outer parts of the U-section as interaction boundaries. This was not successful. As the available time was running out, the work on this model needed to be stopped, leaving the model unsolved. If more time had been available several different modifications of this model could have been tried to find the issue causing the analysis breakdown:

- Running the model without turbulence model in a model with only one element in z-direction
- Try a simpler structural geometry, e.g. a square beam to minimize the co-simulation boundaries
- Running the model using a fully rigid structural part as a test

8.4 Conclusion

The experience gained from working with this FSI analysis is that the complexity of these analysis seems to make them more fragile to instability compared to pure CFD or pure structural analysis.

The software used was a pre-release of Abaqus 6.10. The FSI cababilities is brand new in this version of Abaqus, and the possibility of instable code and bugs are present.

The analysis breakdown could have several possible explanations e.g. modelling and mesh problems, erroneous analysis settings or the use of pre-release software.

Chapter 9

Conclusions

A light supporting mast at Reykjavik Airport has been used as a case study for studying vortex-induced vibrations. Computational fluid dynamics has been used as a tool to study the vortex shedding phenomena. A theory summary has been written on vortex induced vibrations and computational fluid dynamics. Subjects like aeroelasticity, VIV countermeasures, turbulence models and numerical calculation methods has been topics of interest.

Several different computer analyses has been done. A modal analysis of the lightmast has been performed. CFD analysis has been done on the original light mast, the light mast with flaps and in addition two alternative suggestive VIV reducing devices. An analysis using Fluid-Structure Interaction was also attempted, but no results were produced.

The modal analysis gave unexpected problems since the light mast partially was built up by a semi-open U-section. The issue was whether this beam should be modelled as a closed or an open section. As the different models gave very divergent results, a shell element model was made, and comparison was done to the beam element models. It was found that the semi-open U-section was closer to being an open section than a closed one. The shell element model was however reasoned as the most accurate, since the geometry of the light mast could be modelled in detail.

The first CFD model evaluated, was of the original light mast U-section. Just as the measurements and observation at site had predicted, a narrow banded vortex shedding lift force was found. The flow around the U-section clearly indicated the alternating pattern of vortex generation behind the U-section. The analysis also gave very accurate results for mean drag coefficient and Strouhal number.

The second CFD model was a model of the U-section equipped with the installed pipe flaps. Also here the CFD analysis could confirm the observations made during field study. The pipe flaps was seen to be very effective VIV countermeasuring devices, and the fluctuating lift force was seen to almost completely vanish. The main effect introduced by the pipes was flowing of air both over and under the pipes. The effect of this was that the formation of vortices were almost fully reduced. The installed pipes were also seen to reduce separation and thereby reducing the mean drag force.

The first alternative VIV countermeasuring device tested, was a flat plate fixed above the U-section flange. The flat plate was seen to disrupt the narrow banded vortex shedding frequency, and a more broad banded spectrum was seen. The effect of a broad banded

spectrum is that the lift force is randomly varying along the section, thereby reducing the violent vibrations. It is therefore believed that this countermeasure would reduce the vibrations significantly.

The second alternative device tested was a square flap attached to the U-section's flange. This device gave no changes at all compared to the original U-section. It is believed that the square flap was too small, and that a bigger flap possibly could give an effect. It is however not known to what extent the flow would be altered using a bigger square.

A Fluid-Structure Interaction analysis was also attempted. This analysis was aborted due to analysis instabilities and no results were produced. FSI analysis seems more exposed to analysis instability than pure CFD analysis. The mathematics and computer coding involved is complex, and consequently more instability and fragile behaviour should be expected when running these analysis.

One experience gained from working with CFD is that computer time is a major factor. For practical engineering use, where project time is limited, CFD is seemingly not always an appropriate solution to vortex shedding problems. The time consumption of a CFD analysis is extensive. When including all steps of an CFD analysis, from modelling, mesh analysis and to the final analysis time, time in the extent of several weeks/months is often needed. Because of this, analytic and empirical formulas will probably still be the most used vortex shedding design guide for many years to come.

The main benefit experienced from using CFD is the level of 'hands on experience' achieved. This experience is invaluable, and no analytic or empirical formulas can provide the same level of understanding of the flow characteristics. For designing aerodynamical countermeasures to existing structures VIV problems, the use of CFD provides an opportunity of making well documented devices and suggestions for VIV reduction.

The benefits of CFD will likely be discovered by many more engineers from different disciplines in the time to come. As time consumption decreases, CFD will probably be introduced to an increasing range of problems and fields of study.

Bibliography

- Abaqus, 2010. v.6.10 Pre-Release 3,4 and 5.
- Abaqus documentation. Simulia, 2010. Version 6.10 Pre-Release.
- J.D. Anderson. *Computational fluid dynamics*. McGraw-Hill New York, 1995.
- A. Bakker. Computational Fluid Dynamics Lectures. Personal webpage, June 2010. URL <http://www.bakker.org/dartmouth06/engs150/10-rans.pdf>.
- B. Bessason and J.T. Snaebjörnsson. Vortex shedding induced vibrations of a light mast. 2008.
- R.D Blevins. Flow-induced vibration, 1990.
- CFDOnline. CFD Online Wiki, June 2010. URL <http://www.cfd-online.com/Wiki>.
- DNV. DNV-RP-C205: Environmental conditions and environmental loads, April 2007.
- Claës Dyrbye and Svend Ole Hansen. *Wind loads on structures*. Wiley, Chichester, 1999.
- Eurocode-1. Actions on structures - Part 1-4: General actions - Wind actions, 2005.
- Sesam Genie, 2007. v3.5-20.
- J.D. Holmes. *Wind loading of structures*. Spon Pr, 2001.
- S. R. Idelsohn and E. Oñate. Finite volumes and finite elements: Two “good friends”. *International Journal for Numerical methods in Engineering*, 37:3323–3341, 1994.
- NASA. The Spalart-Allmaras Turbulence Model. Langley Research Center Turbulence Modeling Resource, June 2010. URL <http://turbmodels.larc.nasa.gov/spalart.html>.
- A.N. Oppen. Vortex Induced Vibrations - Evaluation of design criteria. Statoil Document no.95337, 1995.
- S. Rao Singiresu. *Mechanical vibrations*. Pearson Education South Asia Pte. Ltd., 2004.
- H. Schlichting and K. Gersten. *Boundary-layer theory*. Springer Verlag, 2000.
- C.T. Shaw. *Using computational fluid dynamics*. Prentice Hall, 1992.

- Emil Simiu and Robert H Scanlan. *Wind effects on structures: fundamentals and applications to design*. Wiley, New York, 1996.
- P. R. Spalart and S.R. Allmaras. A one-equation turbulence model for aerodynamic flows. *La Recherche Aèrospatiale*, (1):5–21, 1994.
- H.K. Versteeg and W. Malalasekera. *An introduction to computational fluid dynamics: the finite volume method*. Prentice Hall, 2007.
- B.J. Vickery and R.I. Basu. Across-wind vibrations of structures of circular cross section. part 1 and 2. *Journal of Wind Engineering and Industrial Aerodynamics*, 12:49–73 and 75–97, 1983.
- M. M. Zdravkovich. Review and classification of various aerodynamic and hydrodynamic means for suppressing vortex shedding. *Journal of Wind Engineering and Industrial Aerodynamics*, 7(2):145–189, 1981.

List of Figures

2.1	The vortex street behind a cylinder [Dyrbye and Hansen, 1999].	6
2.2	The variation of the Strouhal number for various cross sections and Reynolds numbers [Holmes, 2001].	7
2.3	Evolution of vortex-shedding frequency with wind velocity over an elastic structure [Simiu and Scanlan, 1996].	8
2.4	Influence of the amplitude of motion upon the correlation length [Dyrbye and Hansen, 1999].	8
2.5	The ratio between the aerodynamic damping in turbulent flow, δ_a^T , and smooth flow, δ_a^S , as a function of the large-scale turbulence intensity for a circular cylinder [Dyrbye and Hansen, 1999].	10
2.6	The risk of violent vortex-induced vibrations increases with low turbulence intensity and low Scruton numbers [Dyrbye and Hansen, 1999].	11
2.7	Add on devives for suppression of vortex-induced vibration of cylinders: (a) helical strike; (b) shroud; (c) axial slats; (d) streamlined fairing; (e) splitter; (f) ribboned cable; (g) pivoted guiding vane; (h) spoiler plates [Blevins, 1990]	13
3.1	The mast supporting flight control lamps. Large oscillations were observed at the cantiliever beam shortly after installation [Bessason and Snaeðbjörnsson, 2008].	14
3.2	The light mast was equipped with pipes over and under the section [Bessason and Snaeðbjörnsson, 2008].	15
3.3	The light mast after the installation of flaps [Bessason and Snaeðbjörnsson, 2008].	15
4.1	The first two mode shapes of the standard beam element model. The mode shapes shows uncontinous deformation.	17
4.2	Mode shape 1-9 of the open-section beam element model	18
4.3	Mode shape 1-6 of the closed-section beam element model	20
4.4	Mode shape 1-8 of the shell element model	21
5.1	The two different forms used for deriving the governing equations	23
5.2	An infinitesimally small element fixed in space with mass flux through the faces.	24
5.3	Stress components in the x-direction Anderson [1995].	25
5.4	Energy fluxes in the x-direction Anderson [1995].	27
6.1	The model's dimensions in x- and y-direction.	34
6.2	The model's boundary conidtions.	35
6.3	3D model meshing (Model No.5).	40
6.4	The x-y mesh in the model used to evaluate the z-length significance	41

6.5	Model with z-length 0.4m made up by 2 elements of 0.2m.	41
6.6	Model with depth 1m made up by 5 elements of 0.2m.	42
6.7	Model with depth 2m made up by 10 elements of 0.2m.	42
6.8	Model with depth 2m made up by 5 elements of 0.4m.	43
6.9	Model with depth 2m made up by 3 elements of 0.67m.	43
6.10	Model with depth 3m made up by 5 elements of 0.6m.	44
6.11	The velocity profile for viscous flow over a flat plate [Anderson, 1995].	45
6.12	The boundary layer over a flat plate at laminar flow, $U=8\text{m/s}$	46
6.13	The velocity gradients over a flat plate at laminar flow, $U=8\text{m/s}$	46
6.14	The mesh of model no. 7. The boundary layer mesh has a near-wall resolution of 5mm.	47
6.15	Refined mesh in the boundary layer with a near-wall resolution of 5mm.	47
6.16	The near wall mesh of model no. 8. The boundary layer mesh has a near-wall resolution of 1mm.	48
6.17	Refined mesh in the boundary layer with a near-wall resolution of 1mm.	49
7.1	Velocity contour plots of the wake	51
7.2	Velocity and surface pressure at $t=2.87$, $C_L=-2.11$	52
7.3	Velocity and surface pressure at $t=3.04$, $C_L=2.13$	53
7.4	The mesh of the wind-flaps model.	54
7.5	Drag and lift coefficients for the model with wind flaps.	55
7.6	Velocity plot of the wake at $t=7\text{s}$	55
7.7	Velocity and surface pressure at $t=7\text{s}$	56
7.8	The near-wall mesh of the flat plate model.	58
7.9	Lift and drag coefficient of the plate flap model	59
7.10	The beating phenomena [Rao Singiresu, 2004].	59
7.11	Frequency power spectrum lift.	60
7.12	Frequency power spectrum drag.	61
7.13	The mesh of the square flap model.	62
7.14	Results from the model with the square flap.	63
7.15	Velocity and surface pressure at $t=4.22$, $C_L=-1.9$	63
7.16	Velocity and surface pressure at $t=4.38$, $C_L=1.9$	64
8.1	Principle sketch of the FSI model.	65
8.2	Structural model meshing	66
8.3	CFD model meshing.	67

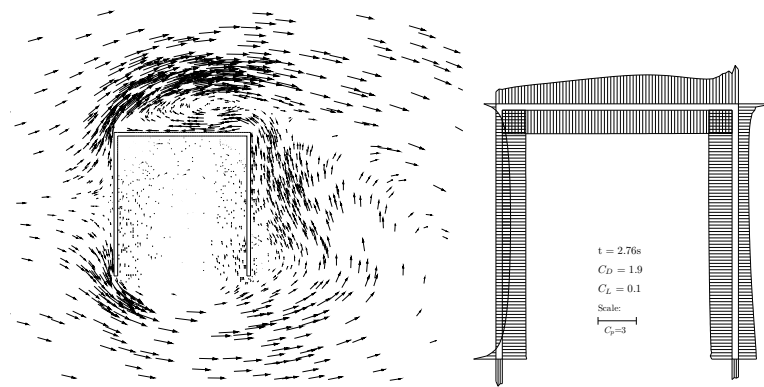
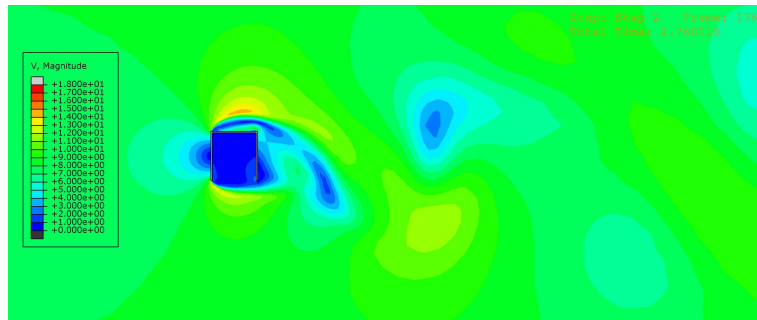
List of Tables

4.1	Mode shapes for the open-section beam model	18
4.2	Mode shapes of the closed-section beam model	19
4.3	Mode shapes for the shell element model	20
6.1	Fluid settings	36
6.2	Time incrementation settings	36
6.3	Solver settings	37
6.4	Summary of the results from the z-length and z-number of elements study. . .	44
6.5	Summary of the results from boundary layer meshing study	49
6.6	Drag coefficient and Strouhal number for relevant cross sections [Eurocode-1, 2005].	50
7.1	Summary of the results from the plate flap model	58
7.2	Summary of the results from boundary layer meshing study.	62

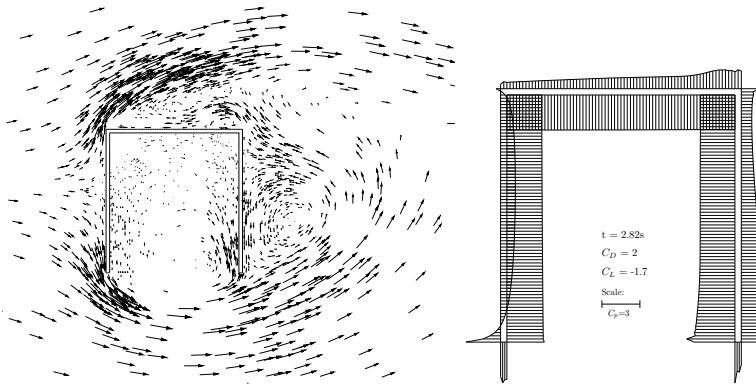
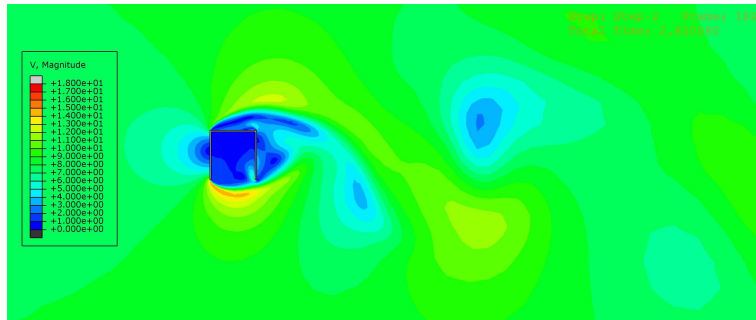
Appendix A

Plots - U-section model

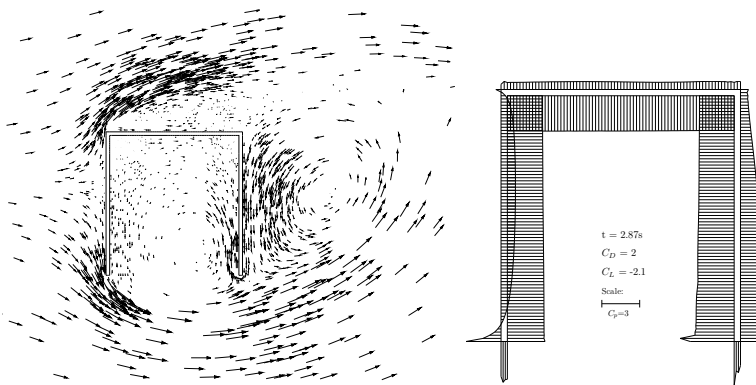
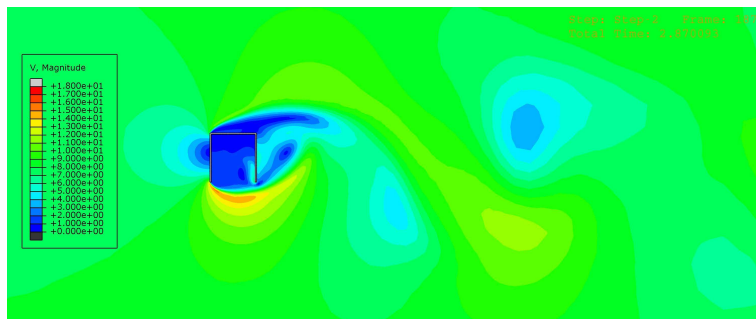
This appendix includes velocity contour plots, velocity vector plots and surface pressure plots for one full vortex shedding period.



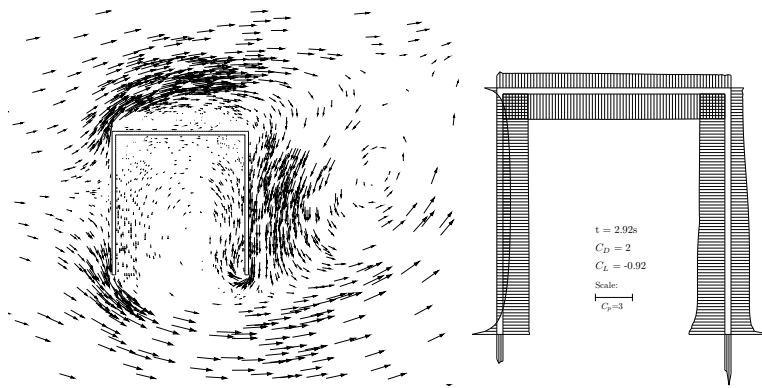
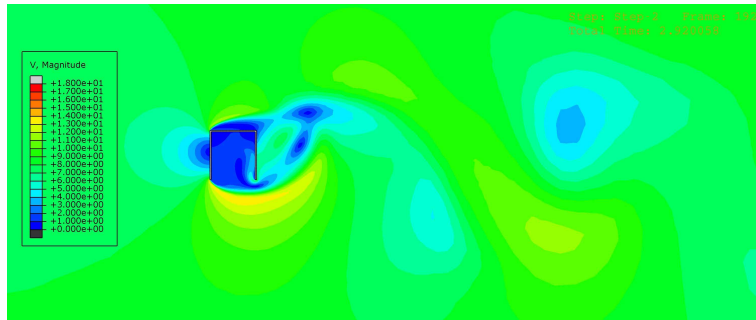
$t = 2.76s$



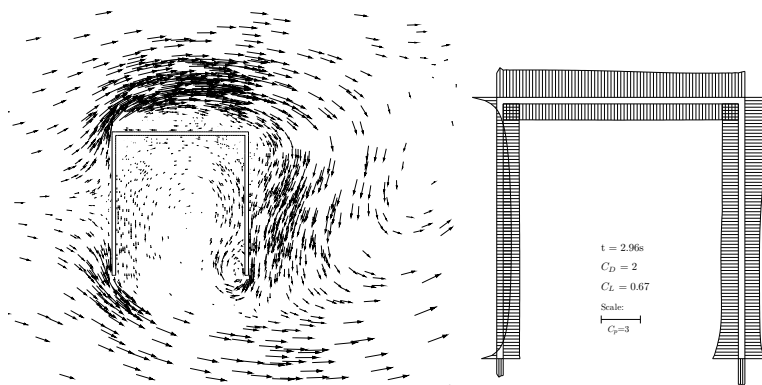
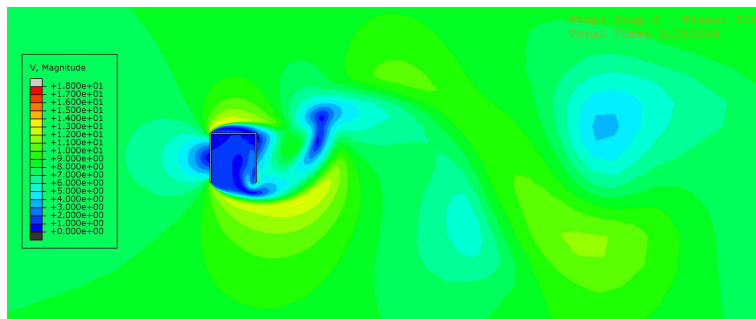
$t = 2.82s$



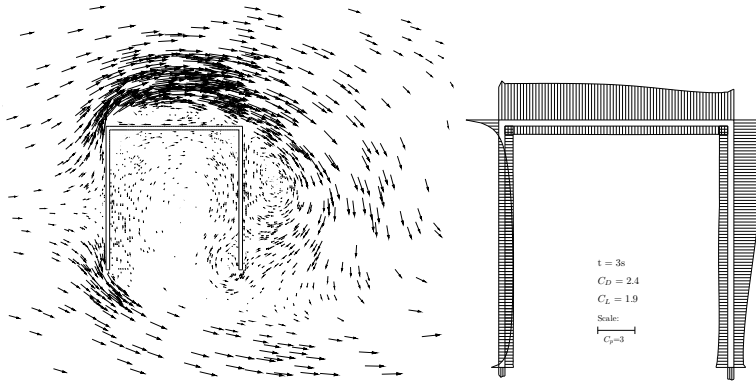
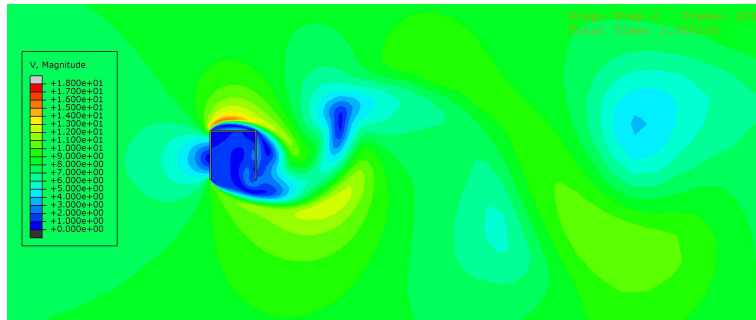
$t = 2.87s$



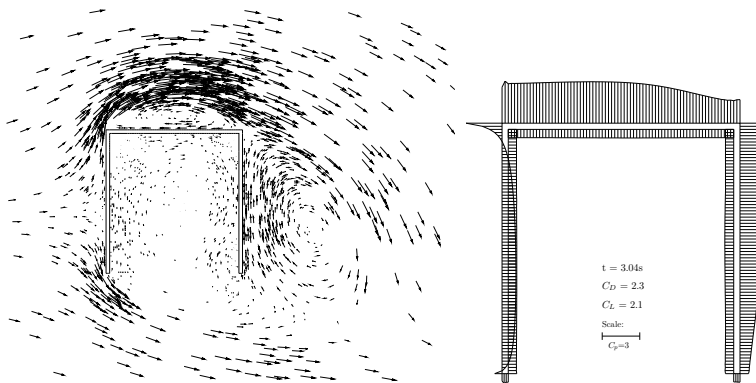
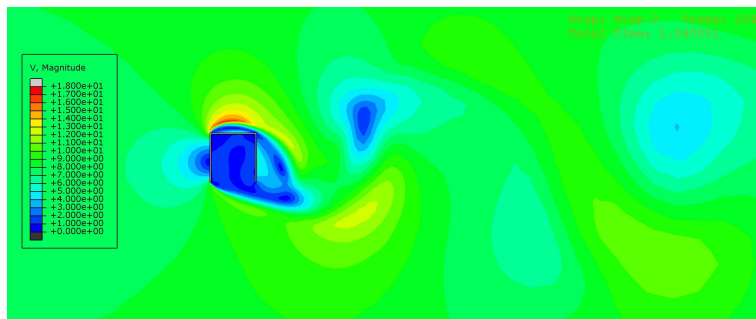
$t = 2.92s$



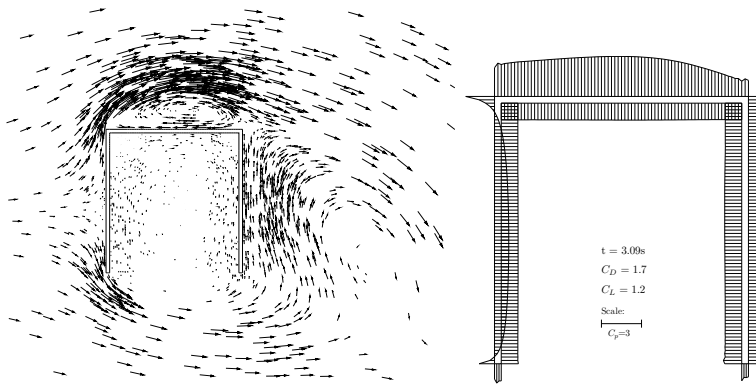
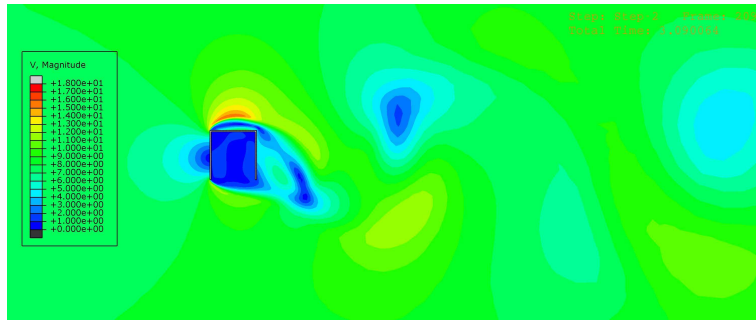
$t = 2.96s$



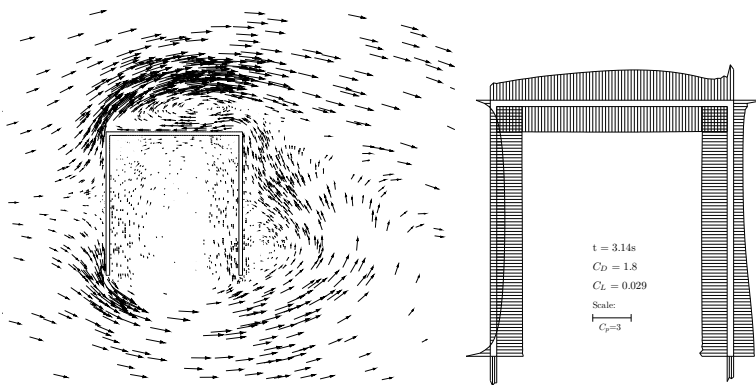
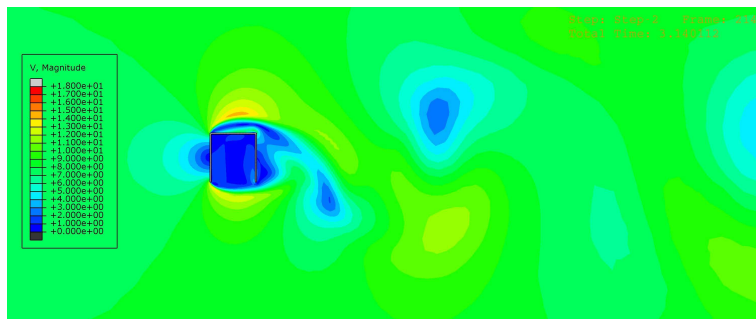
t = 3.00s



t = 3.04s



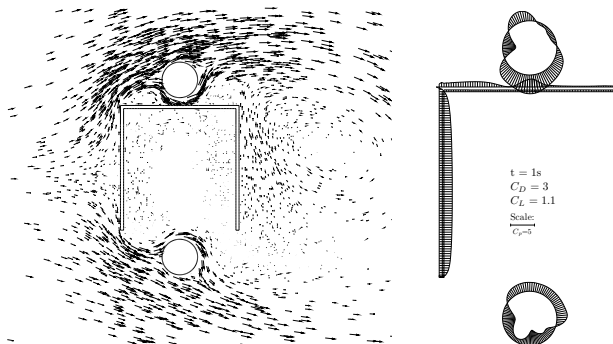
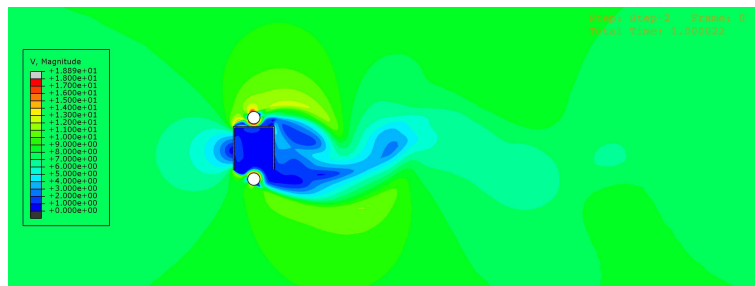
t = 3.09s



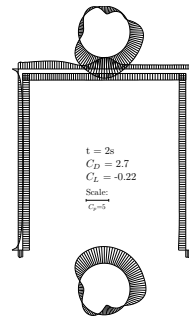
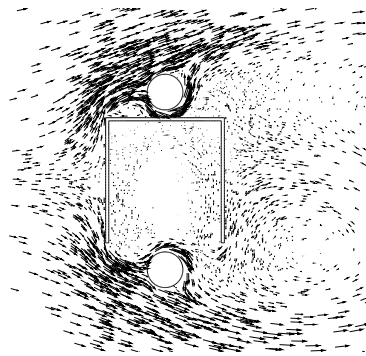
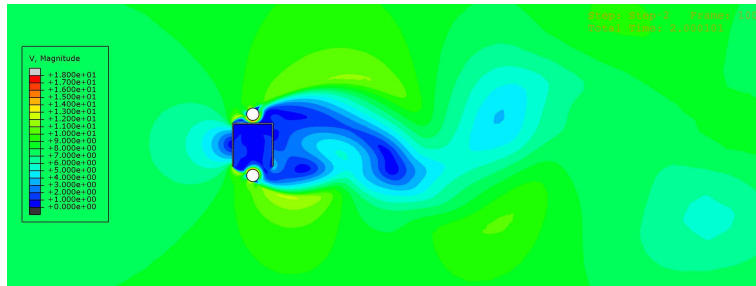
t = 3.14s

Appendix B

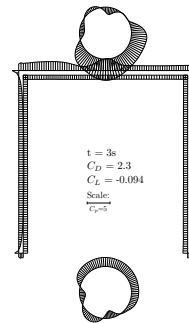
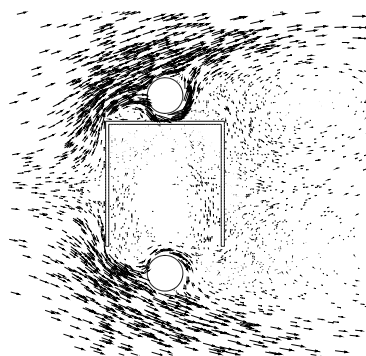
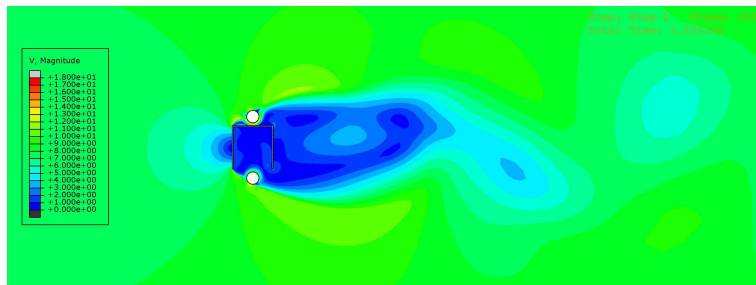
Plots - Installed countermeasure model



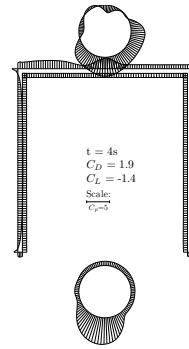
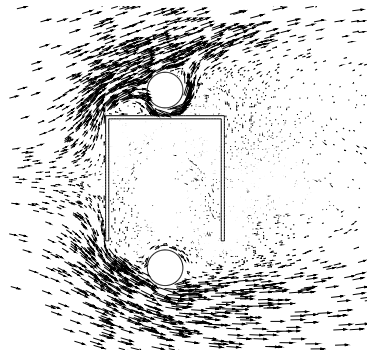
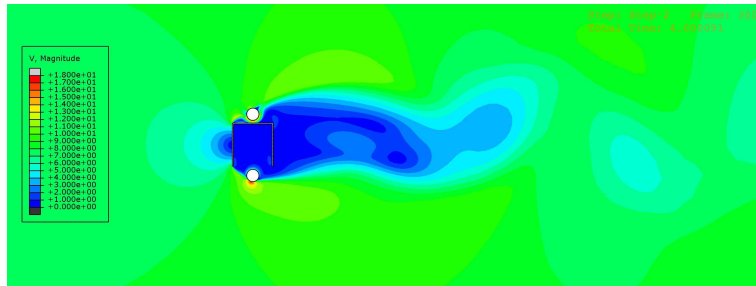
$t = 1s$



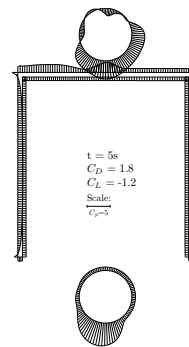
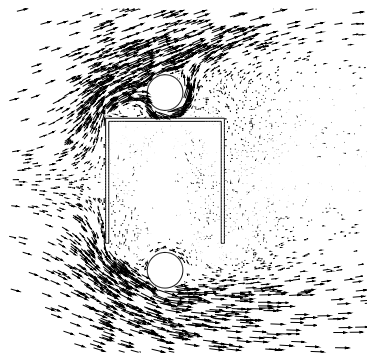
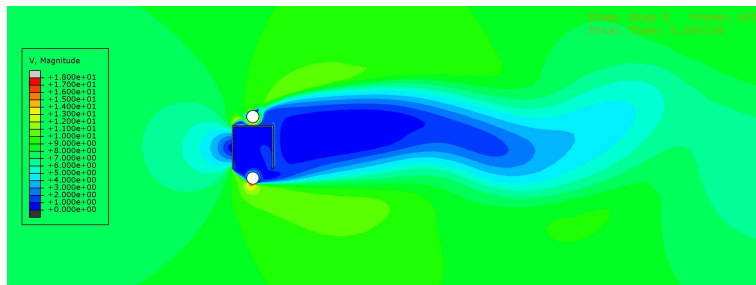
$t = 2s$



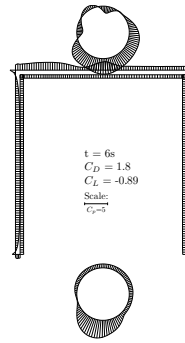
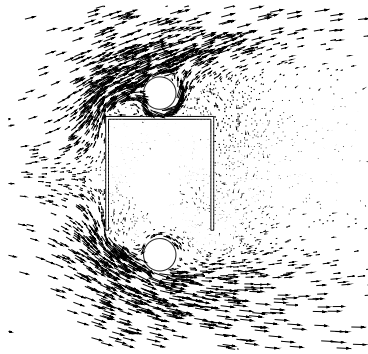
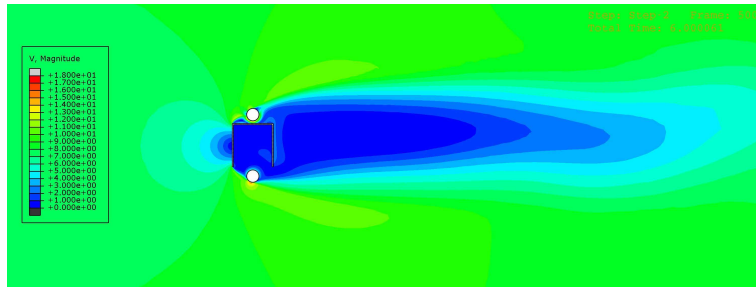
$t = 3s$



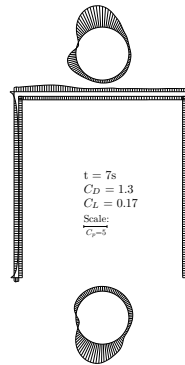
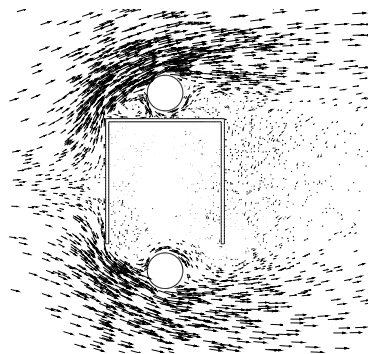
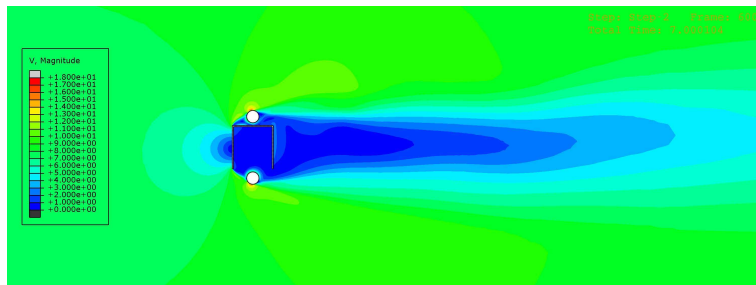
t = 4s



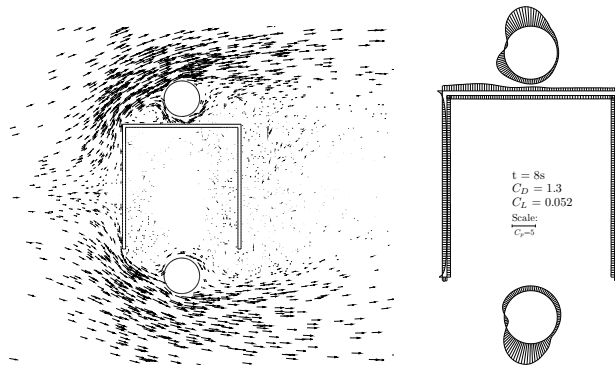
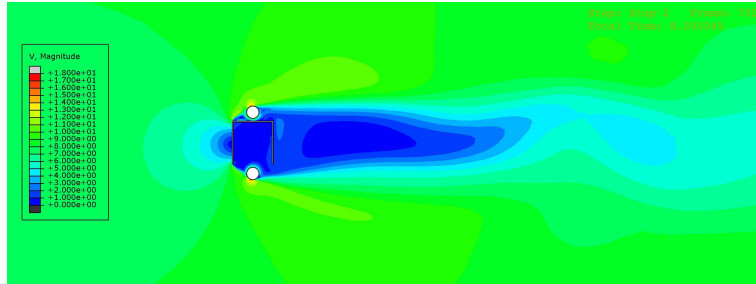
t = 5s



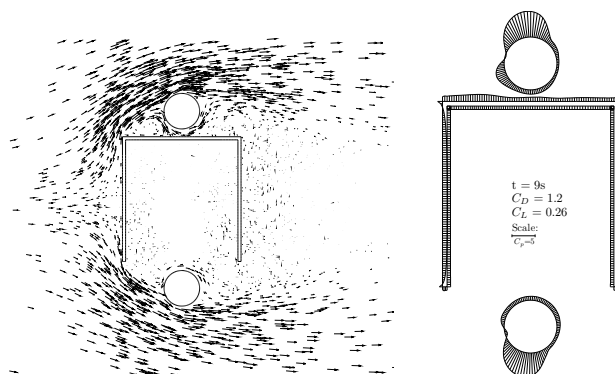
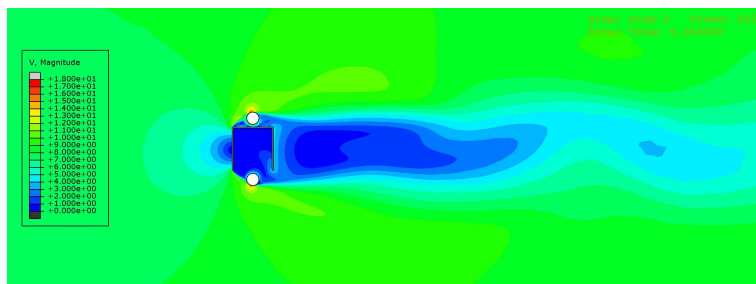
$t = 6s$



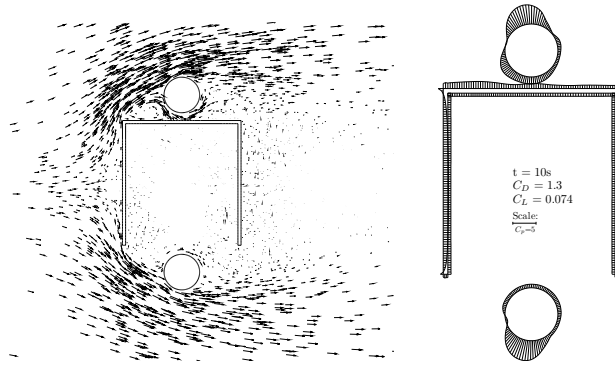
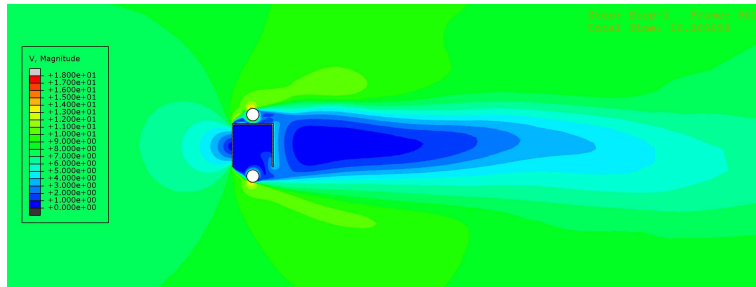
$t = 7s$



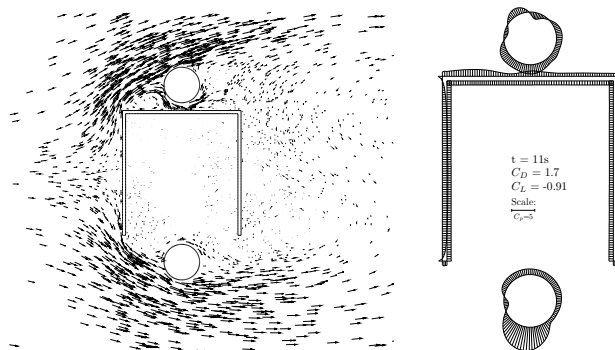
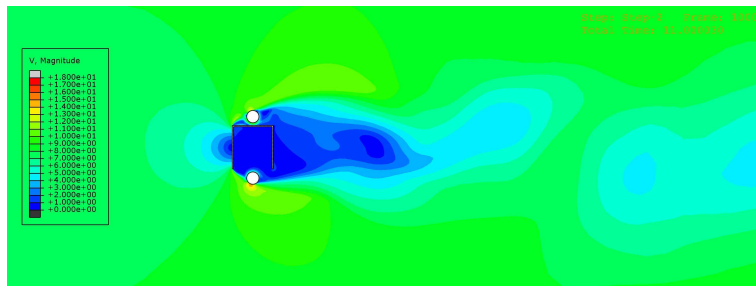
t = 8s



t = 9s



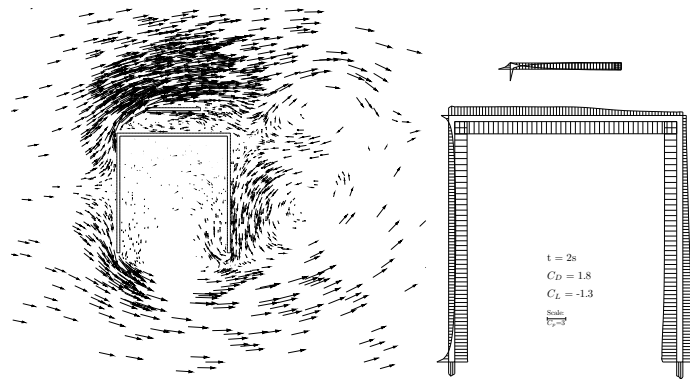
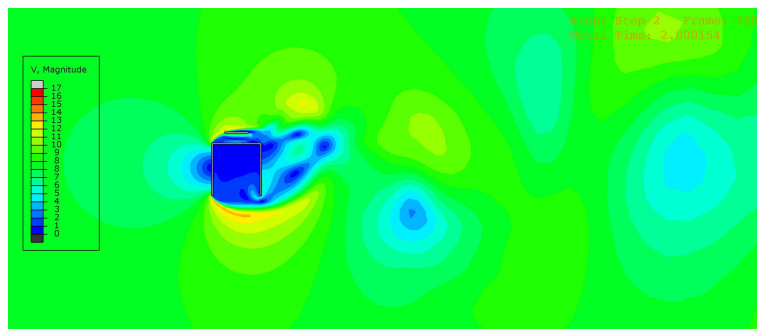
t = 10s



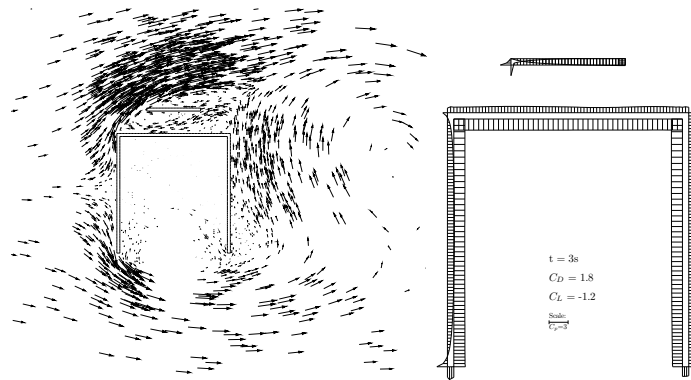
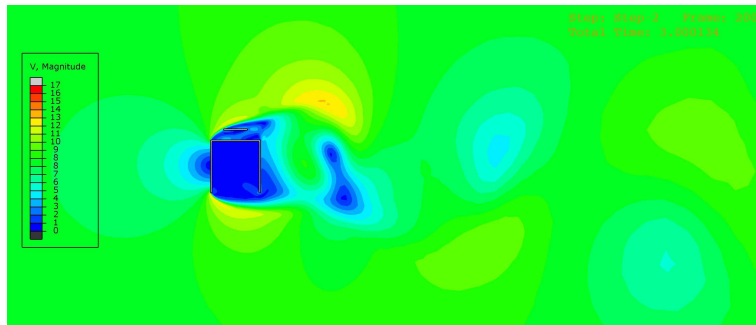
t = 11s

Appendix C

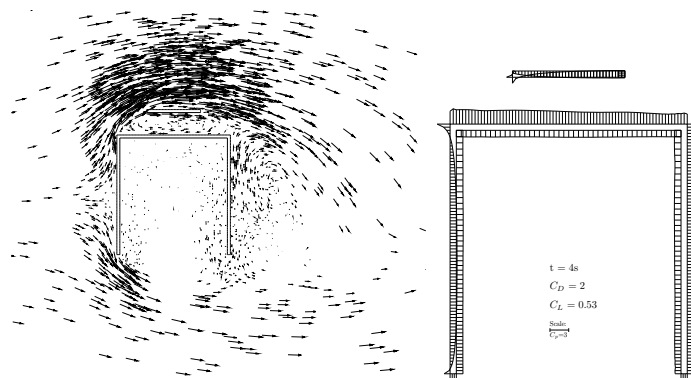
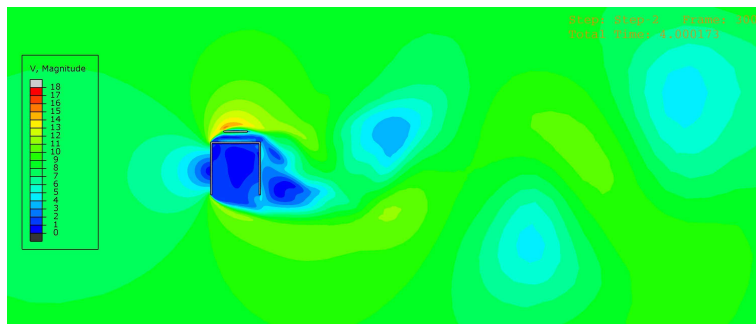
Plots - Flat plate model



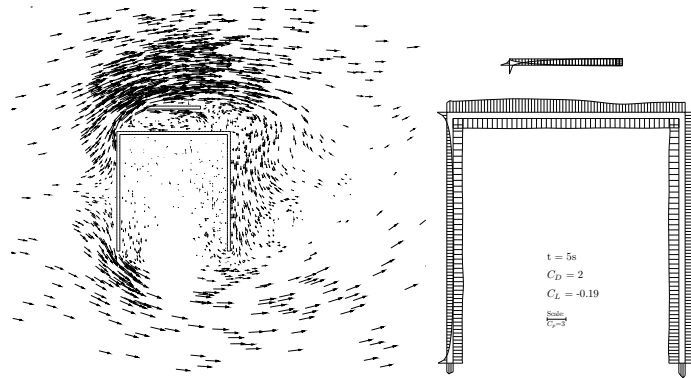
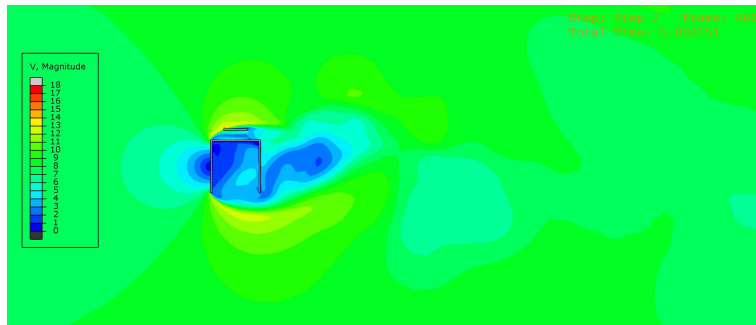
$t = 2s$



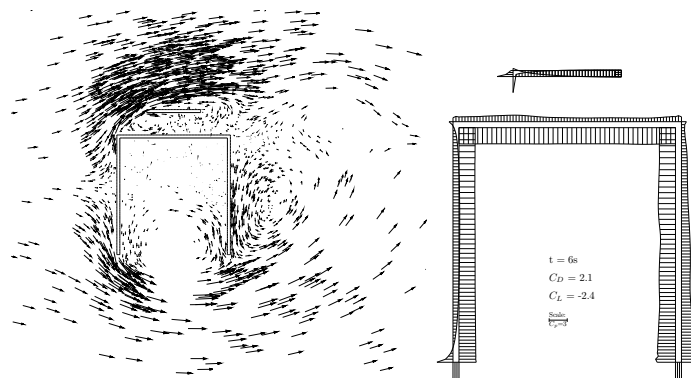
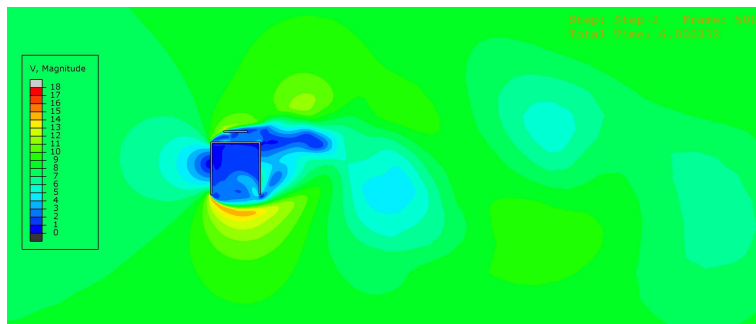
$t = 3s$



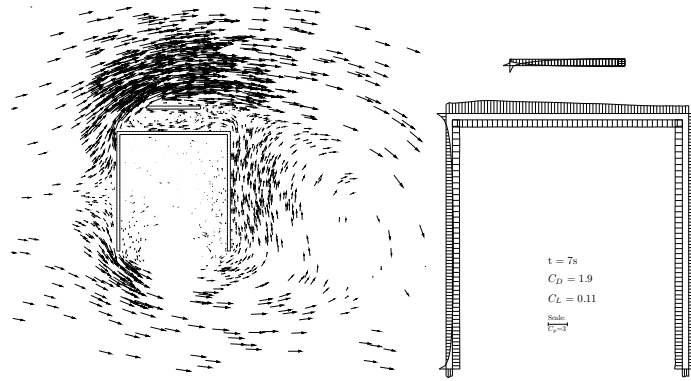
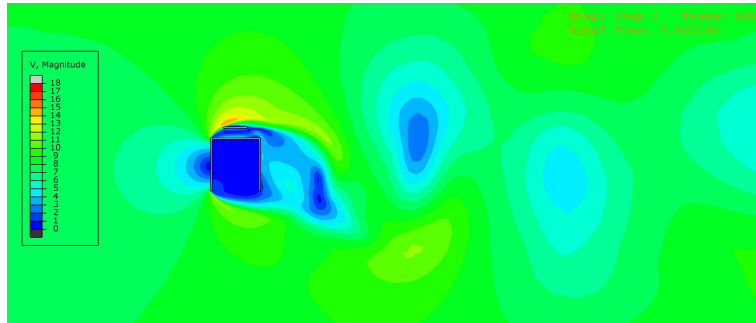
$t = 4s$



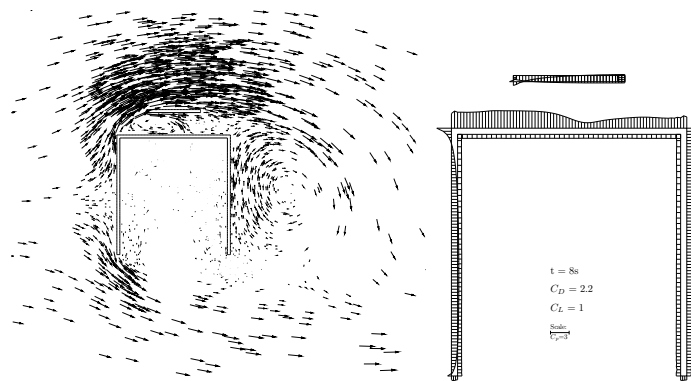
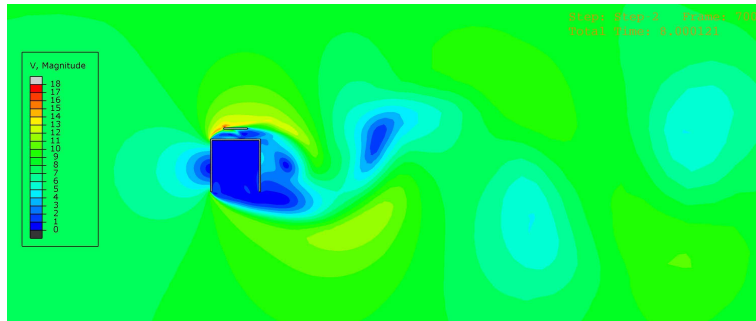
t = 5s



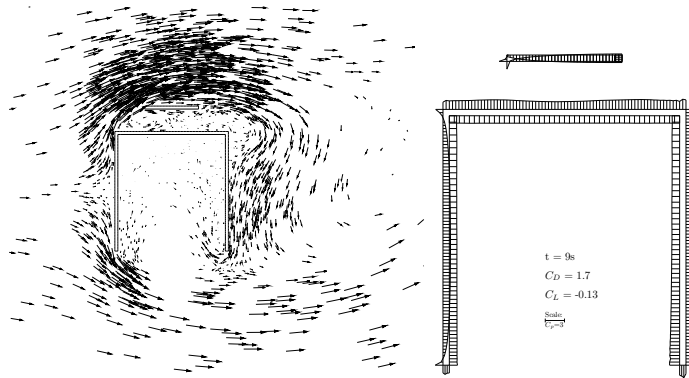
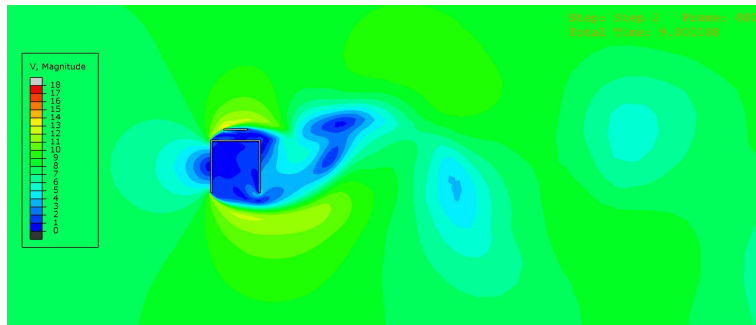
t = 6s



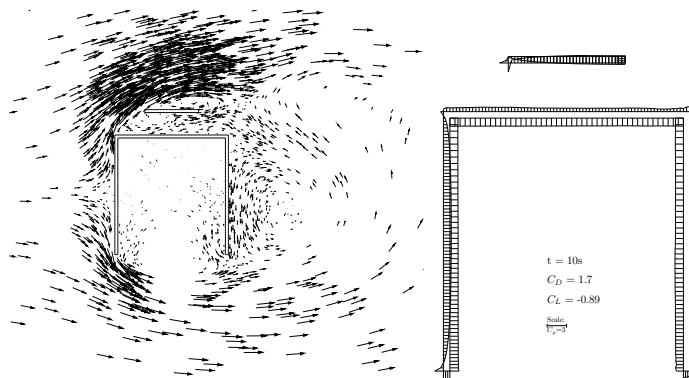
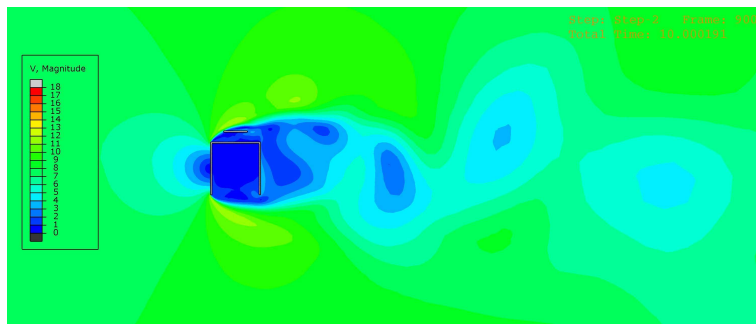
$t = 7s$



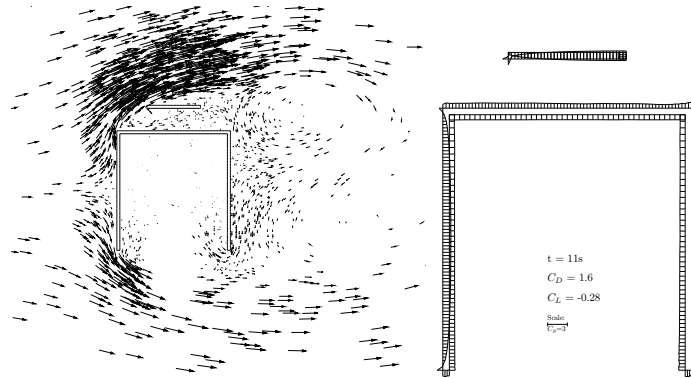
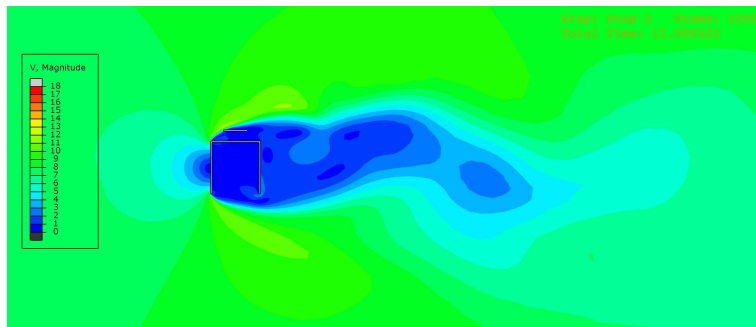
$t = 8s$



t = 9s



t = 10s

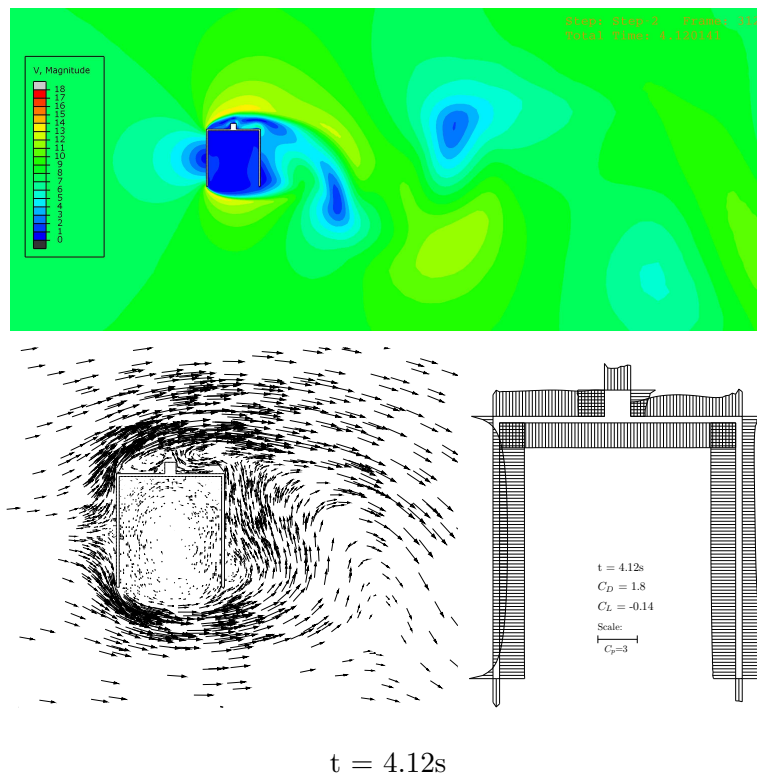


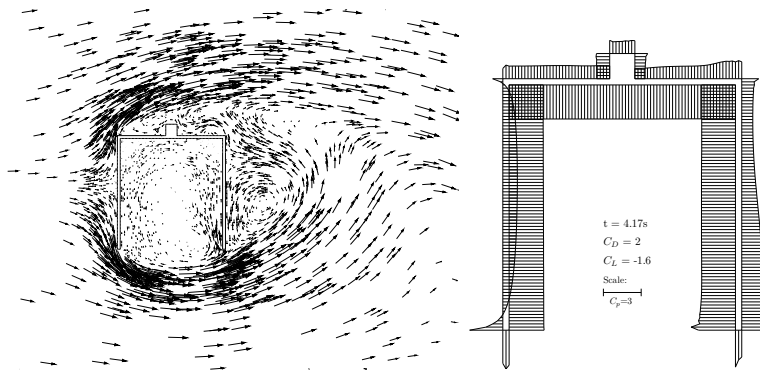
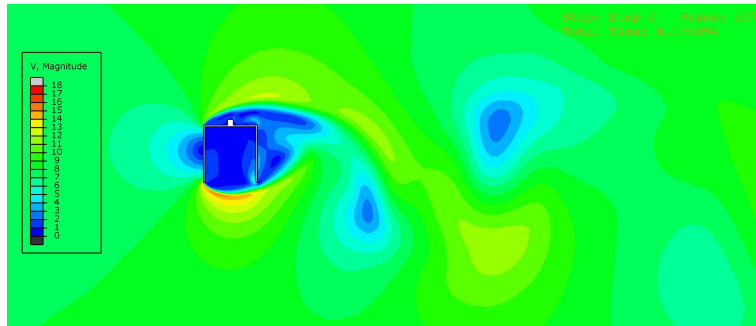
$t = 11s$

Appendix D

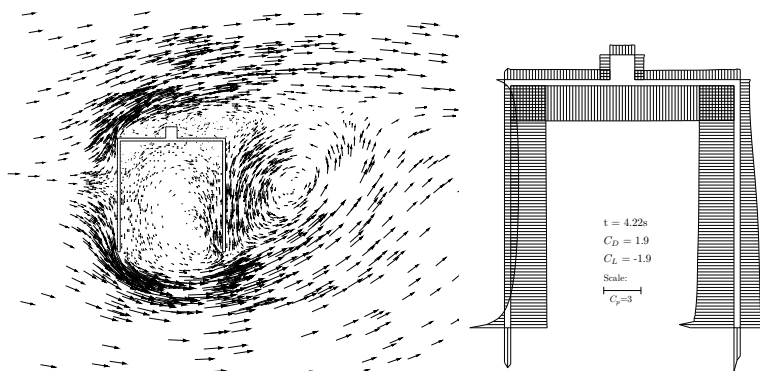
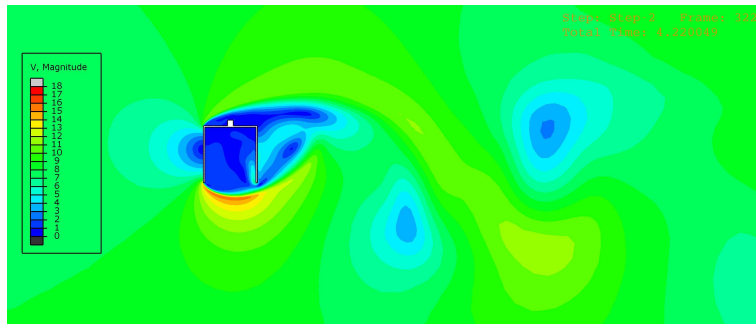
Plots - Square flap model

This appendix includes velocity contour plots, velocity vector plots and surface pressure plots for one full vortex shedding period.

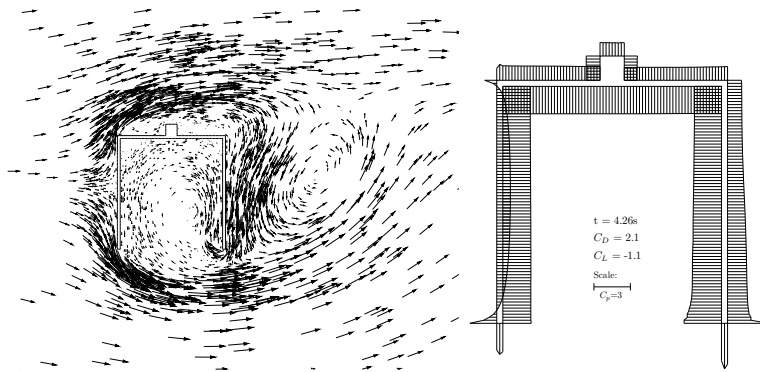
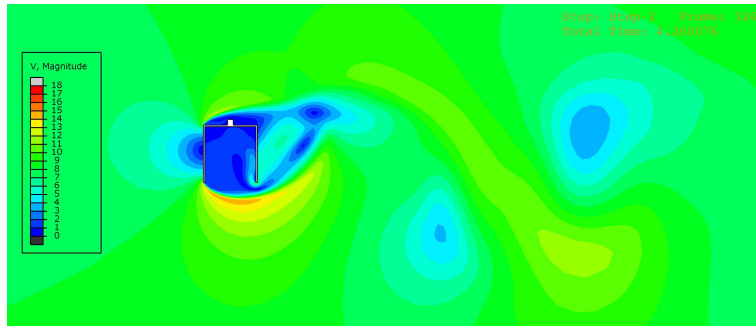




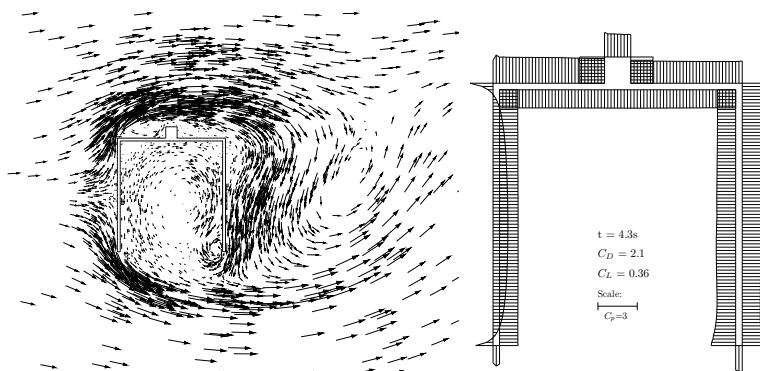
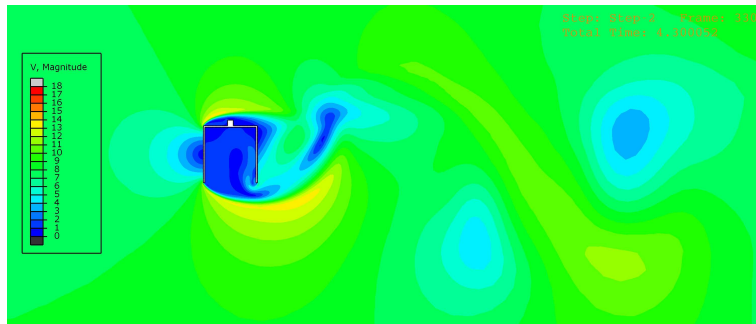
$t = 4.17s$



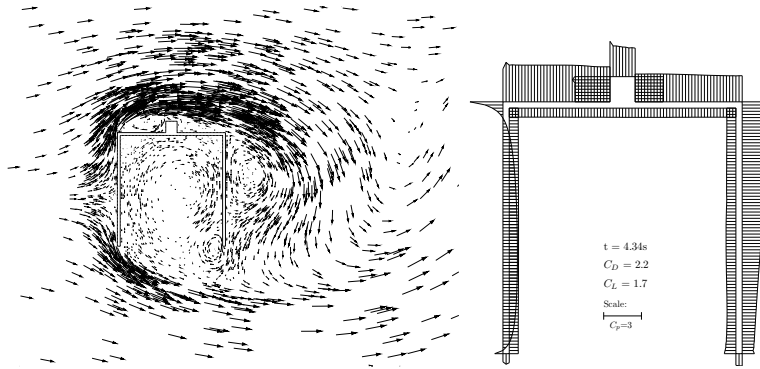
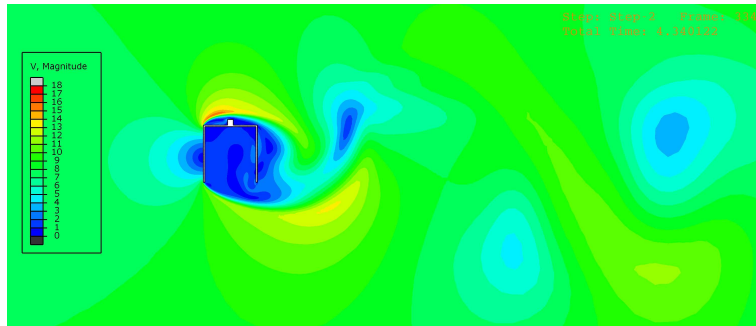
$t = 4.22s$



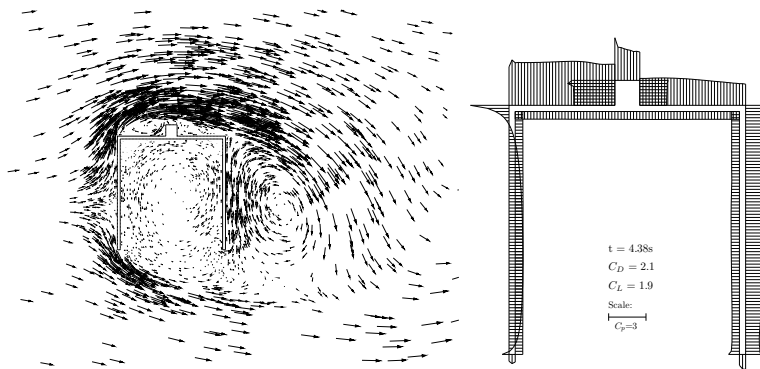
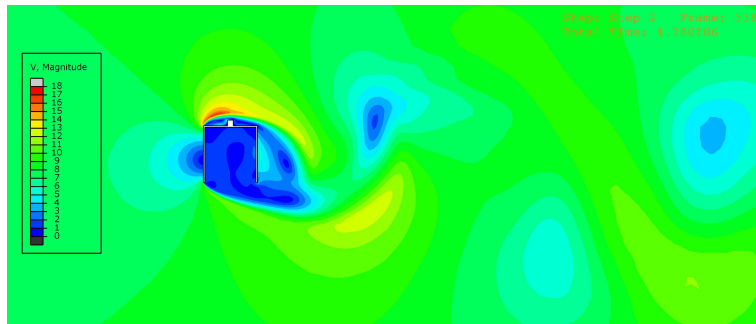
$t = 4.26s$



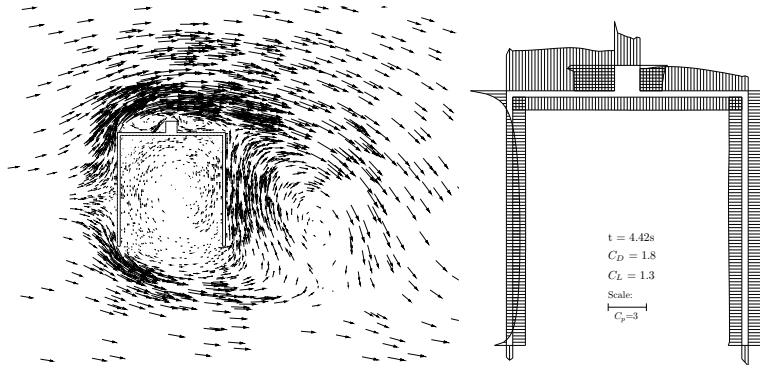
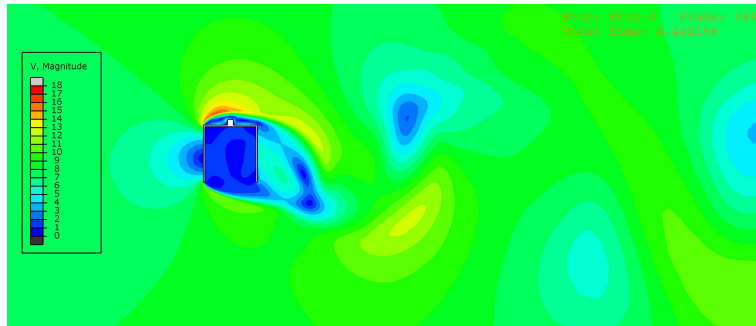
$t = 4.30s$



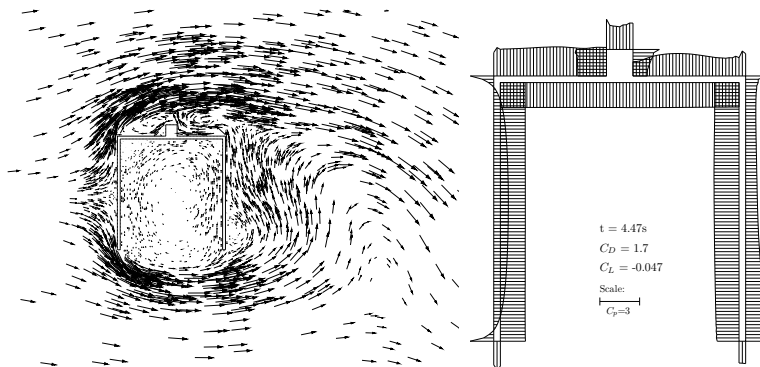
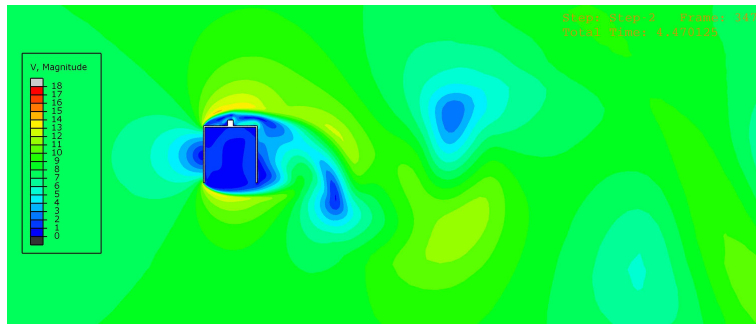
$t = 4.34s$



$t = 4.38s$



t = 4.42s



t = 4.47s

Appendix E

Matlab program

The code attached is the code for extracting results from the flat plate model. As the code was customized to the geometry, the code is slightly different for the other models.

Creating force vectors

```
%Reading data files
path='C:\abaqus_work\CFD turbulent flow flaps\node pressure flaps\';
model='flaps_plate_';

%4 column file: node number,x,y,z
nodes = dlmread([path 'flaps_plate_nodes.txt'],'', 0, 0);

%Node pressure at U-section nodes. 1st column is time, 1st row is node numbers
p_usemention = dlmread([path model 'usemention.rpt'],'', 2, 0);

%Node pressure at flat plate. 1st column is time, 1st row is node numbers
p_plate = dlmread([path model 'plate.rpt'],'', 2, 0);

while p_usemention(1,end)==0 %deleting zero data
    p_usemention(:,end)=[];
end

while p_plate(1,end)==0 %deleting zero data
    p_plate(:,end)=[];
end

%Creating matrices with the node coordinates around the section
usemention_coord = zeros(length(p_usemention(1,2:end)), 4);
for j=1:length(p_usemention(1,2:end))
    usemention_coord(j,:)=nodes((p_usemention(1,j+1)),:);
end
```

```

plate_coord = zeros(length(p_plate(1,2:end)), 4);
for j=1:length(p_plate(1,2:end))
    plate_coord(j,:)=nodes((p_plate(1,j+1)),:);
end

%The node coordinates are sorted by node number. Sorting the node
%coordinates by the geometry instead.

%U-section- Splitting the coordinates into 8 parts where part1 is the front
%and the rest is following a clockwise order

part1=zeros(400,4); %Creating zero matrices with approximate size
part2=zeros(400,4);
part3=zeros(400,4);
part4=zeros(20,4);
part5=zeros(400,4);
part6=zeros(400,4);
part7=zeros(400,4);
part8=zeros(20,4);

count1=1;
count2=1;
count3=1;
count4=1;
count5=1;
count6=1;
count7=1;
count8=1;

for i=1:length(usection_coord(:,1));
    if (round(usection_coord(i,2)*1000)==-190)
        part1(count1,:)=usection_coord(i,:);
        count1=count1+1;
    elseif (round(usection_coord(i,3)*1000)==200)
        part2(count2,:)=usection_coord(i,:);
        count2=count2+1;
    elseif (round(usection_coord(i,2)*1000)==190)
        part3(count3,:)=usection_coord(i,:);
        count3=count3+1;
    elseif (round(usection_coord(i,3)*1000)==-200) && (usection_coord(i,2)>0)
        part4(count4,:)=usection_coord(i,:);
        count4=count4+1;
    elseif (round(usection_coord(i,2)*1000)==180)
        part5(count5,:)=usection_coord(i,:);
        count5=count5+1;
    elseif (round(usection_coord(i,3)*1000)==190)

```

```

        part6(count6,:)=usection_coord(i,:);
        count6=count6+1;
    elseif (round(usection_coord(i,2)*1000)==-180)
        part7(count7,:)=usection_coord(i,:);
        count7=count7+1;
    elseif (round(usection_coord(i,3)*1000)==-200) && (usection_coord(i,2)<0)
        part8(count8,:)=usection_coord(i,:);
        count8=count8+1;
    end;
end

clear count1 count2 count3 count4 count5 count6 count7 count8;

%Deleting zero rows

while part1(end,1)==0;
    part1(end,:)=[];
end

while part2(end,1)==0;
    part2(end,:)=[];
end

while part3(end,1)==0;
    part3(end,:)=[];
end

while part4(end,1)==0;
    part4(end,:)=[];
end

while part5(end,1)==0;
    part5(end,:)=[];
end

while part6(end,1)==0;
    part6(end,:)=[];
end

while part7(end,1)==0;
    part7(end,:)=[];
end

while part8(end,1)==0;
    part8(end,:)=[];
end

```

```

%Sorting the part matrices by coordinate

part1=sortrows(part1,3); %sorting by increasing y
part2=sortrows(part2,2); %sorting bt increasing x
part3=flipud(sortrows(part3,3)); %sorting by decreasing y
part4=flipud(sortrows(part4,2)); %sorting by decreasing x
part5=sortrows(part5,3); %sorting by increasing y
part6=flipud(sortrows(part6,2)); %sorting by decreasing x
part7=flipud(sortrows(part7,3)); %sorting by decreasing y
part8=flipud(sortrows(part8,2)); %sorting by decreasing x

usection_coord=[part1;part2;part3;part4;part5;part6;part7;part8];

%sorting the p_usection matrix p_usection in the same way as usection_coord
temp_mat=zeros(length(p_usection(:,1)),length(p_usection(1,:)));
temp_mat(:,1)=p_usection(:,1);
for j=1:length(usection_coord);
    temp=find(p_usection(1,:)==usection_coord(j));
    temp_mat(:,j+1)=p_usection(:,temp(1,1));
end

while temp_mat(1,end)==0;
    temp_mat(:,end)=[];
end

p_usection=temp_mat;

clear temp_mat;

%Flaps plate- Splitting the coordinates into 4 parts where part1 is the front
%and the rest is following a clockwise order

part9=zeros(10,4); %approximate matrix sices
part10=zeros(50,4);
part11=zeros(10,4);
part12=zeros(50,4);

count9=1;
count10=1;
count11=1;
count12=1;

for i=1:length(plate_coord(:,1));

```

```

        if (round(plate_coord(i,2)*1000)==-90)
            part9(count9,:)=plate_coord(i,:);
            count9=count9+1;
        elseif (round(plate_coord(i,3)*1000)==285)
            part10(count10,:)=plate_coord(i,:);
            count10=count10+1;
        elseif (round(plate_coord(i,2)*1000)==90)
            part11(count11,:)=plate_coord(i,:);
            count11=count11+1;
        elseif (round(plate_coord(i,3)*1000)==275)
            part12(count12,:)=plate_coord(i,:);
            count12=count12+1;
        end;
    end

clear count9 count10 count11 count12;

%Deleting zero rows

while part9(end,1)==0;
    part9(end,:)=[];
end

while part10(end,1)==0;
    part10(end,:)=[];
end

while part11(end,1)==0;
    part11(end,:)=[];
end

while part12(end,1)==0;
    part12(end,:)=[];
end

%Sorting the part matrices by coordinate

part9=sortrows(part9,3); %sorting by increasing y
part10=sortrows(part10,2); %sorting bt increasing x
part11=flipud(sortrows(part11,3)); %sorting by decreasing y
part12=flipud(sortrows(part12,2)); %sorting by decreasing x

plate_coord=[part9;part10;part11;part12];

%sorting the p_plate matrix in the same way as plate_coord
temp_mat=zeros(length(p_plate(:,1)),length(p_plate(1,:)));
temp_mat(:,1)=p_plate(:,1);

```

```

for j=1:length(plate_coord);
    temp=find(p_plate(1,)==plate_coord(j));
    temp_mat(:,j+1)=p_plate(:,temp(1,1));
end

while temp_mat(1,end)==0;
    temp_mat(:,end)=[];
end

p_plate=temp_mat;

clear temp_mat;

%Creating directional vectors for the u-section
u_vector=zeros(length(usection_coord),2);
start=1;
stop=length(part1(:,1));
for i=start:stop;
    u_vector(i,:)=[1 0];
end
start=stop+1;
stop=start+length(part2(:,1));
for i=start:stop;
    u_vector(i,:)=[0 -1];
end
start=stop;
stop=start+length(part3(:,1));
for i=start:stop;
    u_vector(i,:)=[-1 0];
end
start=stop;
stop=start+length(part4(:,1));
for i=start:stop;
    u_vector(i,:)=[0 1];
end
start=stop;
stop=start+length(part5(:,1));
for i=start:stop;
    u_vector(i,:)=[1 0];
end
start=stop;
stop=start+length(part6(:,1));
for i=start:stop;
    u_vector(i,:)=[0 1];
end
start=stop;
stop=start+length(part7(:,1));

```

```

for i=start:stop;
    u_vector(i,:) = [-1 0];
end
start=stop;
stop=start+length(part8(:,1));
for i=start:stop;
    u_vector(i,:) = [0 1];
end

clear start stop;

%Creating directional vectors for the flaps_plate
plate_vector=zeros(length(plate_coord),2);
start=1;
stop=length(part9(:,1));
for i=start:stop;
    plate_vector(i,:) = [1 0];
end
start=stop+1;
stop=start+length(part10(:,1));
for i=start:stop;
    plate_vector(i,:) = [0 -1];
end
start=stop;
stop=start+length(part11(:,1));
for i=start:stop;
    plate_vector(i,:) = [-1 0];
end
start=stop;
stop=start+length(part12(:,1));
for i=start:stop;
    plate_vector(i,:) = [0 1];
end

clear start stop;

%The model with the flaps plate has different mesh size along the section.
%Creating an element length matrix for the section

u_length=zeros(length(usection_coord),1);
start=1;
stop=length(part1(:,1));
for i=start:stop;
    u_length(i)=0.005;
end
start=stop+1;
stop=start+length(part2(:,1));

```



```

for i=start:stop;
    u_length(i)=0.005;
end
start=stop;
stop=start+length(part3(:,1));
for i=start:stop;
    u_length(i)=0.005;
end
start=stop;
stop=start+length(part4(:,1));
for i=start:stop;
    u_length(i)=0.0033;
end
start=stop;
stop=start+length(part5(:,1));
for i=start:stop;
    %Mesh size is increasing gradually from 5mm to 10mm
    u_length(i)=0.005+0.005*(i-start)/(stop-start);
end
start=stop;
stop=start+length(part6(:,1));
for i=start:stop;
    u_length(i)=0.01;
end
start=stop;
stop=start+length(part7(:,1));
for i=start:stop;
    %Mesh size is decreasing gradually from 5mm to 10mm
    u_length(i)=0.01-0.005*(i-start)/(stop-start);
end
start=stop;
stop=start+length(part8(:,1));
for i=start:stop;
    u_length(i)=0.0033;
end

clear start stop;

%Creating an element length matrix for the plate

plate_length=zeros(length(plate_coord),1);
start=1;
stop=length(part9(:,1));
for i=start:stop;
    plate_length(i)=0.0033;
end
start=stop+1;

```

```

stop=start+length(part10(:,1));
for i=start:stop;
    plate_length(i)=0.005;
end
start=stop;
stop=start+length(part11(:,1));
for i=start:stop;
    plate_length(i)=0.0033;
end
start=stop;
stop=start+length(part12(:,1));
for i=start:stop;
    plate_length(i)=0.005;
end

clear start stop;

%The pressure matrixes, the vector matrixes and the area matrixes can now
%be combined to find force component in x or y
fx_usemention = zeros(length(p_usemention(2:end,1)), length(p_usemention(1,:)));
fy_usemention = zeros(length(p_usemention(2:end,1)), length(p_usemention(1,:)));
for j=2:length(p_usemention(1,:))
    fx_usemention(:,j-1)=u_vector(j-1,1)*u_length(j-1)*p_usemention(2:end,j);
    fy_usemention(:,j-1)=u_vector(j-1,2)*u_length(j-1)*p_usemention(2:end,j);
end

fx_plate = zeros(length(p_plate(2:end,1)), length(p_plate(1,:)));
fy_plate = zeros(length(p_plate(2:end,1)), length(p_plate(1,:)));
for j=2:length(p_plate(1,:))
    fx_plate(:,j-1)=plate_vector(j-1,1)*plate_length(j-1)*p_usemention(2:end,j);
    fy_plate(:,j-1)=plate_vector(j-1,2)*plate_length(j-1)*p_usemention(2:end,j);
end

U=8; %Wind inlet velocity
rho=1.225; %Air density
H=0.4; %Section height
zelements=4; %The number of z-direction elements included in the results
t= p_usemention(2:end,1); %time matrix

%Creating the force coeffecients matrices
C_D = zeros(length(t), 1);
C_L = zeros(length(t), 1);
for i=(1:length(t))
    %devides the sum by number of z-elements to find average force
    C_D(i)=(sum(fx_usemention(i,1:end))+sum(fx_plate(i,1:end)))...
    /(0.5*rho*H*U^2*zelements);

```

```

    C_L(i)=(sum(fy_usection(i,1:end))+sum(fy_plate(i,1:end)))...
    /(0.5*rho*H*U^2*zelements);
end

%Creating pressure matrices devided in x and y to use for surface pressure plots
px_usection = zeros(length(p_usection(2:end,1)), length(p_usection(1,:)));
py_usection = zeros(length(p_usection(2:end,1)), length(p_usection(1,:)));
for j=2:length(p_usection(1,:))
    px_usection(:,j-1)=u_vector(j-1,1)*p_usection(2:end,j);
    py_usection(:,j-1)=u_vector(j-1,2)*p_usection(2:end,j);
end

px_plate = zeros(length(p_plate(2:end,1)), length(p_plate(1,:)));
py_plate = zeros(length(p_plate(2:end,1)), length(p_plate(1,:)));
for j=2:length(p_plate(1,:))
    px_plate(:,j-1)=plate_vector(j-1,1)*p_usection(2:end,j);
    py_plate(:,j-1)=plate_vector(j-1,2)*p_usection(2:end,j);
end

```

Plotting of lift, drag and frequency spectrum

```

%Plotting C_D and C_L
temp=[C_D C_L];
plot(t,temp);
xlabel('Time');
box off
legend('C_D','C_L','Interpreter','latex','Location','SouthWest');
legend('boxoff');
axis([0 t(end)+0.2 min(C_L)-1 max(C_D)+0.5]); %% zoom in
%print('-depsc',[model 'drag_lift']); %saving to file

%Frequency analysis
% Parameters used for burg algorithm
ORDER = 100;          % order of AR model
FREQUENCY= 0:0.01:10; % vector of frequencies of interest
FS = 100;             % Sampling frequency = 100 Hz
del_time=2; %Not interested in data prior to this number of seconds
row=FS*del_time;

%LIFT

[power_lift,freq_lift] = pburg(C_L(row:end),ORDER,FREQUENCY,FS);

freq_max_lift=freq_lift(power_lift(:)==max(power_lift(200:end)));

plot(freq_lift,power_lift)
axis([0 5 0 max(power_lift)*1.2])

```

```

box off
xlabel('Frequency [Hz]')
ylabel('Power')
text(freq_max_lift*1.01,max(power_lift(200:end))*1.05,...
 ['$f_s$ = ' num2str(freq_max_lift)],'Interpreter','latex','FontSize',16)
%print('-deps',[model 'freq_lift_pburg_order_20']);

%DRAG
ORDER = 200;
C_D_diff=mean(C_D(row:end));
C_D=C_D-C_D_diff; %Adjusting data so that cd mean is at zero
[power_drag,freq_drag] = pburg(C_D(row:end),ORDER,FREQUENCY,FS);

plot(freq_drag,power_drag)
%axis([0 10 0 1.2])
box off
xlabel('Frequency [Hz]')
ylabel('Power')
%print('-deps',[model 'freq_drag_pburg_order200']);

C_D=C_D+C_D_diff; %Fixing C_D to original state

```

Fast Fourier Transform code In some cases the FFT frequency analysis was used instead of Burg's method.

```

FS = 100; % Sampling frequency = 100 Hz
del_time=2; %Not interested in data prior to this number of seconds
row=FS*del_time;

N=length(C_L(row:end)); %Number of data points
T=t(end)-del_time; %%total time in seconds
p = abs(fft(C_L(row:end)))/(N/2); %% absolute value of the fft
p = p(1:N/2).^2; %% take the power of positive freq. half
freq = [0:N/2-1]/T; %% find the corresponding frequency in Hz

%Find frequency with max power
a=[freq;p];
col=find(p==max(p(10:end)));
freq_max=freq(col);

plot(freq,p); %% plot
axis([0 5 0 1.2]); %% zoom in
xlabel('Frequency');
ylabel('Power');
box off
text(freq_max+0.1,p(col)+0.01,['$f_s$ = ' num2str(freq_max,3)],...
'Interpreter','latex','FontSize',16)

```

```
print('-deps',[model 'freq_lift_fourier']);
```

Surface pressure plotting The surface pressure plots were generated using the following code.

```
t=5; %requested point of time for plot
f=round(t*100+1);
norm=1/(0.5*1.225*8^2); %normalizing pressure according to this factor
factor=0.01; %in addition scaling according to this factor
scale=norm*factor;
hold on;
plot(usection_coord(:,2),usection_coord(:,3)); %plot section
plot([usection_coord(end,2) usection_coord(1,2)],...
[usection_coord(end,3) usection_coord(1,3)]); %plot section
fh = figure(1); % returns the handle to the figure object
set(fh, 'color', 'white'); % sets the color to white
axis off;
axis equal;

xy=zeros(length(usection_coord(:,1)),2);
a=1;
for i=1:length(usection_coord(:,1));
    plot([usection_coord(i,2) usection_coord(i,2)+px_usemention(f,i)*scale],...
    [usection_coord(i,3) usection_coord(i,3)+py_usemention(f,i)*scale])
    xy(a,:)=usection_coord(i,2)+px_usemention(f,i)*scale ...
    usection_coord(i,3)+py_usemention(f,i)*scale];
    a=a+1;
    %This part is to make pressure at corners to be plotted at both sides
    if i==(length(part1))
        plot([usection_coord(i,2) usection_coord(i,2)+py_usemention(f,i)*scale],...
        [usection_coord(i,3) usection_coord(i,3)-px_usemention(f,i)*scale])
        xy(a,:)=usection_coord(i,2)+py_usemention(f,i)*scale ...
        usection_coord(i,3)-px_usemention(f,i)*scale];
        a=a+1;
    elseif i==157
        plot([usection_coord(i,2) usection_coord(i,2)+py_usemention(f,i)*scale],...
        [usection_coord(i,3) usection_coord(i,3)-px_usemention(f,i)*scale])
        xy(a,:)=usection_coord(i,2)+py_usemention(f,i)*scale ...
        usection_coord(i,3)-px_usemention(f,i)*scale];
        a=a+1;
    elseif i==237
        plot([usection_coord(i,2) usection_coord(i,2)+py_usemention(f,i)*scale],...
        [usection_coord(i,3) usection_coord(i,3)-px_usemention(f,i)*scale])
        xy(a,:)=usection_coord(i,2)+py_usemention(f,i)*scale ...
        usection_coord(i,3)-px_usemention(f,i)*scale];
        a=a+1;
    elseif i==240
```

```

plot([usection_coord(i,2) usection_coord(i,2)+py_usection(f,i)*scale],...
[usection_coord(i,3) usection_coord(i,3)-px_usection(f,i)*scale])
xy(a,:)= [usection_coord(i,2)+py_usection(f,i)*scale ...
usection_coord(i,3)-px_usection(f,i)*scale];
a=a+1;
elseif i==292
plot([usection_coord(i,2) usection_coord(i,2)+py_usection(f,i)*scale],...
[usection_coord(i,3) usection_coord(i,3)+px_usection(f,i)*scale])
xy(a,:)= [usection_coord(i,2)+py_usection(f,i)*scale ...
usection_coord(i,3)+px_usection(f,i)*scale];
a=a+1;
    elseif i==292
plot([usection_coord(i,2) usection_coord(i,2)+py_usection(f,i)*scale],...
[usection_coord(i,3) usection_coord(i,3)-px_usection(f,i)*scale])
xy(a,:)= [usection_coord(i,2)+py_usection(f,i)*scale ...
usection_coord(i,3)-px_usection(f,i)*scale];
a=a+1;
elseif i==338
plot([usection_coord(i,2) usection_coord(i,2)-py_usection(f,i)*scale],...
[usection_coord(i,3) usection_coord(i,3)-px_usection(f,i)*scale])
xy(a,:)= [usection_coord(i,2)-py_usection(f,i)*scale ...
usection_coord(i,3)-px_usection(f,i)*scale];
a=a+1;
elseif i==390
plot([usection_coord(i,2) usection_coord(i,2)+py_usection(f,1)*scale],...
[usection_coord(i,3) usection_coord(i,3)+px_usection(f,1)*scale])
xy(a,:)= [usection_coord(i,2)+py_usection(f,1)*scale ...
usection_coord(i,3)+px_usection(f,1)*scale];
a=a+1;
elseif i==392
plot([usection_coord(1,2) usection_coord(1,2)+py_usection(f,1)*scale],...
[usection_coord(1,3) usection_coord(1,3)+px_usection(f,1)*scale])
xy(a,:)= [usection_coord(1,2)+py_usection(f,1)*scale ...
usection_coord(1,3)+px_usection(f,1)*scale];
a=a+1;
end
end

%Plotting the lines to mark the pressure contour
start=1;
stop=length(part1);
plot(xy(start:stop,1),xy(start:stop,2));
start=stop+1;
stop=start+length(part2);
plot(xy(start:stop,1),xy(start:stop,2));
start=stop+1;
stop=start+length(part3);

```

```

plot(xy(start:stop,1),xy(start:stop,2));
start=stop+1;
stop=start+length(part4(:,1));
plot(xy(start:stop,1),xy(start:stop,2));
start=stop+1;
stop=start+length(part5);
plot(xy(start:stop,1),xy(start:stop,2));
start=stop+1;
stop=start+length(part6);
plot(xy(start:stop,1),xy(start:stop,2));
start=stop+1;
stop=start+length(part7);
plot(xy(start:stop,1),xy(start:stop,2));
start=stop+1;
plot(xy(start:end,1),xy(start:end,2));
clear start stop xy;

xy=zeros(length(plate_coord(:,1)),2);
plot(plate_coord(:,2),plate_coord(:,3)); %plot section
plot([plate_coord(end,2) plate_coord(1,2)], [plate_coord(end,3) plate_coord(1,3)]);
a=1;
for i=1:length(plate_coord(:,1));
    plot([plate_coord(i,2) plate_coord(i,2)+px_plate(f,i)*scale],...
        [plate_coord(i,3) plate_coord(i,3)+py_plate(f,i)*scale])
    xy(a,:)= [plate_coord(i,2)+px_plate(f,i)*scale ...
             plate_coord(i,3)+py_plate(f,i)*scale];
    a=a+1;
    %This part is to make pressure at corners to be plotted at both sides
    if i==4
        plot([plate_coord(i,2) plate_coord(i,2)+py_plate(f,i)*scale],...
            [plate_coord(i,3) plate_coord(i,3)-px_plate(f,i)*scale])
        xy(a,:)= [plate_coord(i,2)+py_plate(f,i)*scale ...
                 plate_coord(i,3)-px_plate(f,i)*scale];
        a=a+1;
    elseif i==40
        plot([plate_coord(i,2) plate_coord(i,2)+py_plate(f,i)*scale],...
            [plate_coord(i,3) plate_coord(i,3)-px_plate(f,i)*scale])
        xy(a,:)= [plate_coord(i,2)+py_plate(f,i)*scale ...
                 plate_coord(i,3)-px_plate(f,i)*scale];
        a=a+1;
    elseif i==43
        plot([plate_coord(i,2) plate_coord(i,2)+py_plate(f,i)*scale],...
            [plate_coord(i,3) plate_coord(i,3)-px_plate(f,i)*scale])
        xy(a,:)= [plate_coord(i,2)+py_plate(f,i)*scale ...
                 plate_coord(i,3)-px_plate(f,i)*scale];
        a=a+1;

```

```

elseif i==78
    plot([plate_coord(1,2) plate_coord(1,2)+py_plate(f,1)*scale],...
        [plate_coord(1,3) plate_coord(1,3)+px_plate(f,1)*scale])
    xy(a,:)= [plate_coord(1,2)+py_plate(f,1)*scale ...
        plate_coord(1,3)+px_plate(f,1)*scale];
    a=a+1;
end

end

%Plotting the lines to mark the pressure contour
start=1;
stop=length(part9);
plot(xy(start:stop,1),xy(start:stop,2));
start=stop+1;
stop=start+length(part10);
plot(xy(start:stop,1),xy(start:stop,2));
start=stop+1;
stop=start+length(part11(:,1));
plot(xy(start:stop,1),xy(start:stop,2));
start=stop+1;
plot(xy(start:end,1),xy(start:end,2));
clear start stop;

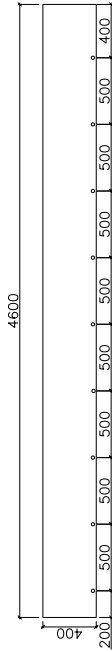
%Plotting a scale for Cp
x=-0.03;
y=-0.13;
plot([x x+3*factor],[y y], 'Color','black');
plot([x x],[y-0.3*factor y+0.3*factor], 'Color','black');
plot([x+3*factor x+3*factor],[y-0.3*factor y+0.3*factor], 'Color','black');
text(x,y-0.8*factor, '$C_p=3$', 'Interpreter','latex', 'FontSize',8);
text(x,y+1*factor, 'Scale:', 'Interpreter','latex', 'FontSize',8);

%Annotating time, Cd and Cl
text(-0.03,-0.03,['t = ' num2str(t) 's'],...
'Interpreter','latex','FontSize',12);
text(-0.03,-0.06,['C_D$ = ' num2str(C_D(f),2)],...
'Interpreter','latex','FontSize',12);
text(-0.03,-0.09,['C_L$ = ' num2str(C_L(f),2)],...
'Interpreter','latex','FontSize',12);
print('-deps',[model 't' num2str(f-1) '.eps']);

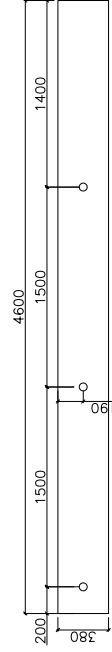
```


Appendix F

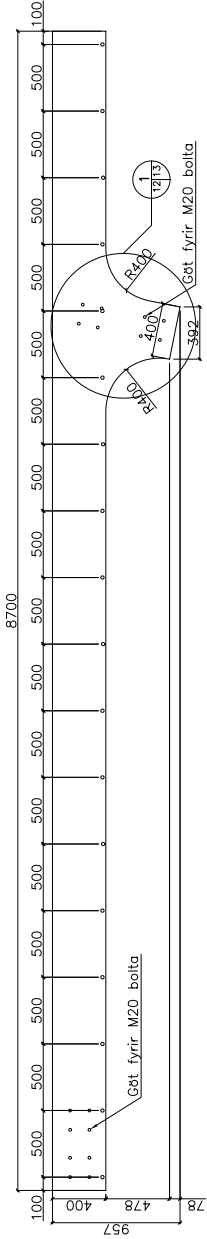
Drawings



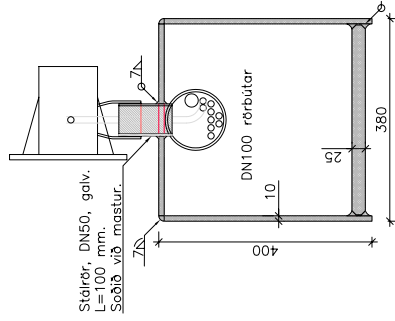
Nr. 1, 10mm stálplata, 2 stk.
Mkv. 1:20



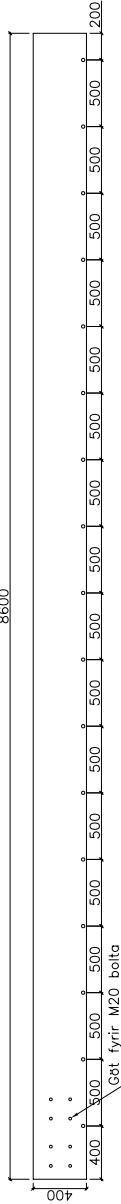
Nr. 2, 10mm stálplata, 1 stk.
Mkv. 1:20



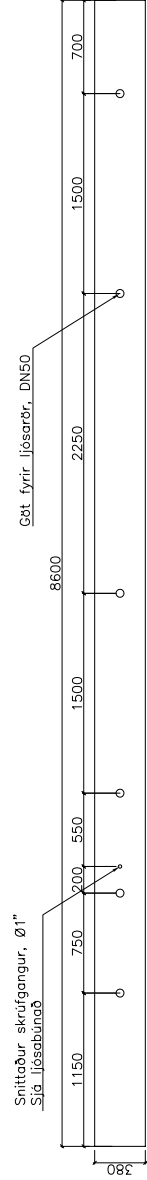
Nr. 3, 10mm stálplata, 2 stk.
Mkv. 1:20



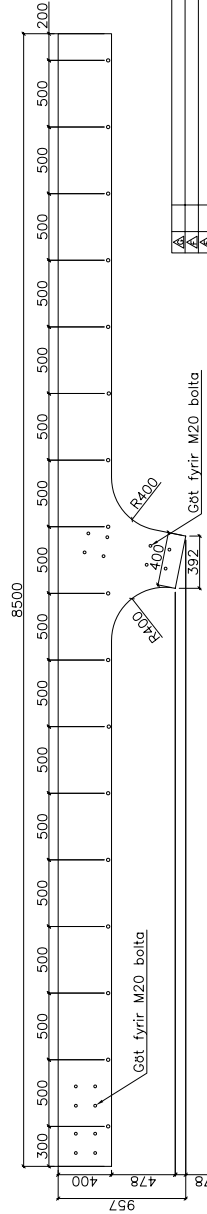
A Snið
10 | 12
Mkv. 1:5



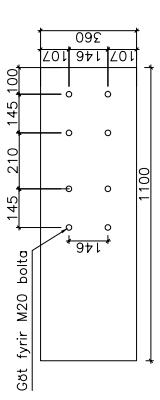
Nr. 4, 10mm stálplata, 1 stk.
Mkv. 1:20



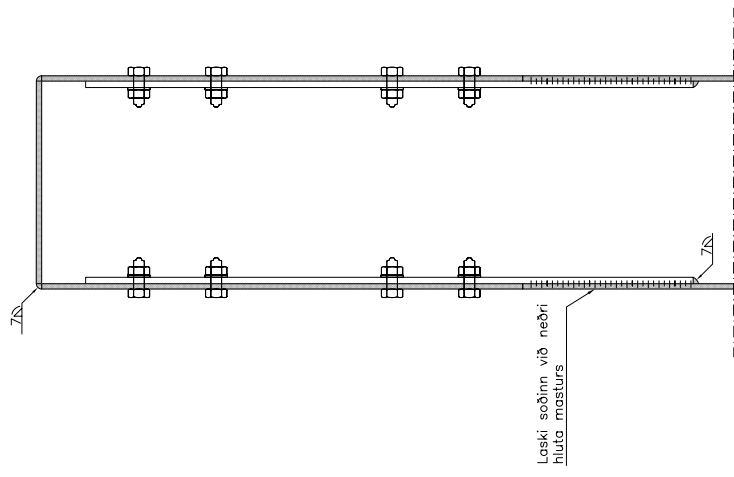
Nr. 5, 10mm stálplata, 2 stk.
Mkv. 1:20



Nr. 6, 10mm stálplata, 1 stk.
Mkv. 1:20

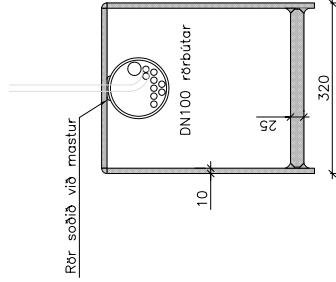


Nr. 3, 12mm stálplata, 2x3 stk.
Mkv. 1:10

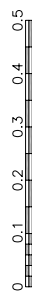


Löski sobinn við neðri hluta másturs

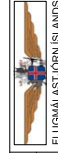
C Snið
10 | 12
Mkv. 1:5



B Snið
10 | 12
Mkv. 1:5



Smekkuþ mynd
smekkan 50%

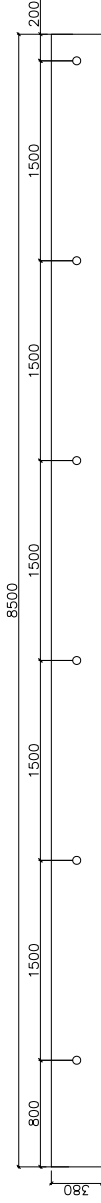


Meinir, röðugla, húsnæðing
03-137 AutocAD
KAV/ETA TEBAC
Fark. DE
Snið 525.0005, Fug. 525.0008

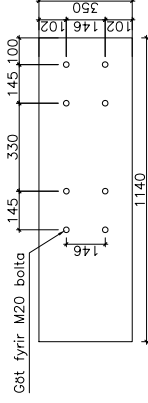
Adflugsljós við Reykjavíkflugvöll
Stálmástur
Form og útlit
Mástur 10
Útgáf. Mkv.:
20.12.2004

Mkv. 1:20
Mkv. 1:20
Mkv. 1:20
Mkv. 1:20

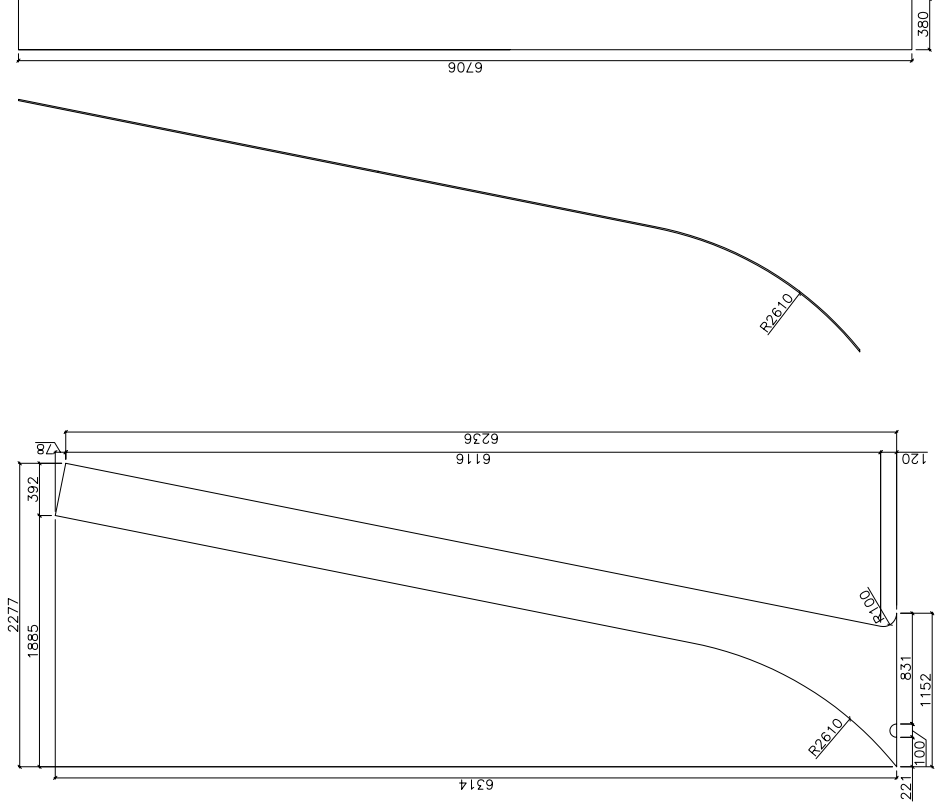
Stærð 13
Útgáf V-12
Tíðni Mkv. 1:20/10/5
Tíðni Mkv. 1:20/10/5



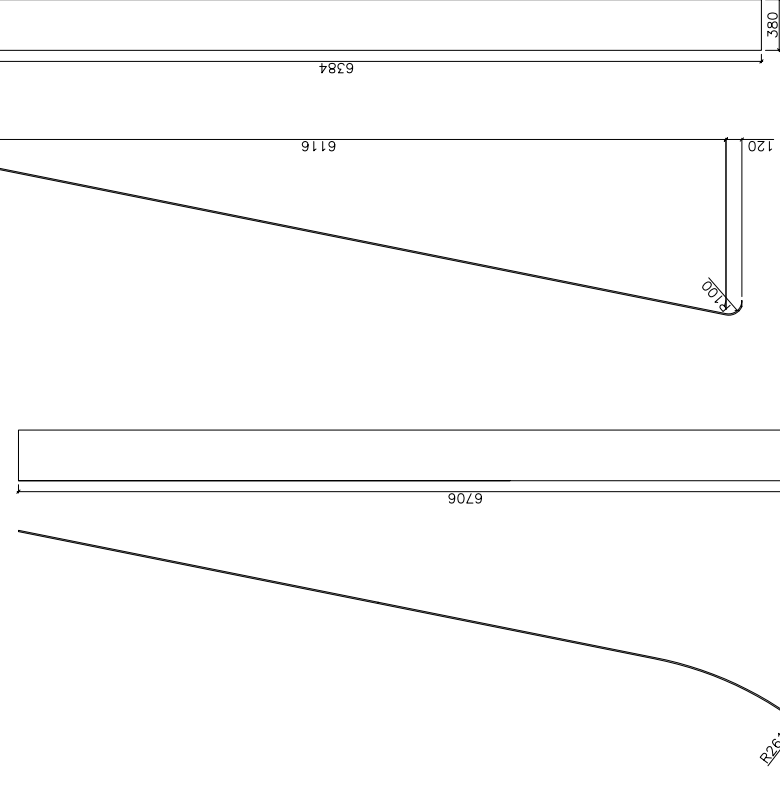
Nr. 9, 10mm stálplata, 1 stk.
Mkv. 1:20



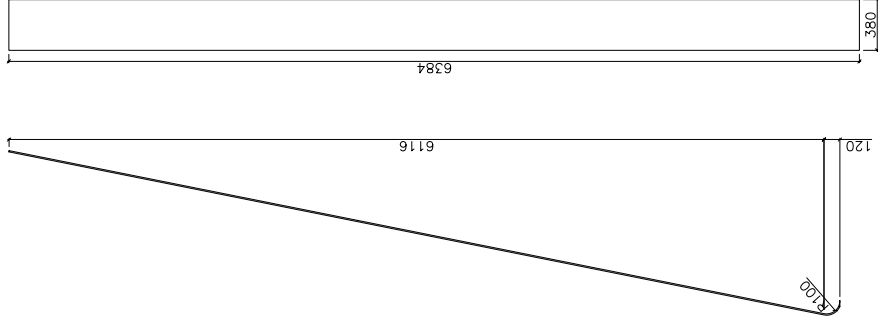
Nr. 10, 12mm stálplata, 2 stk.
Mkv. 1:10



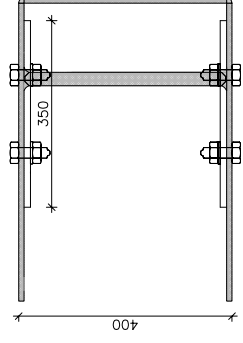
Nr. 11, 10mm stálplata, 2 stk.
Mkv. 1:20



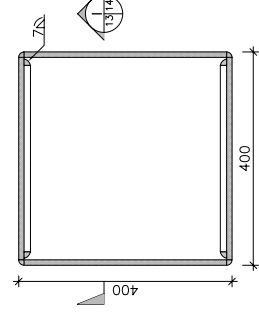
Nr. 12, 10mm stálplata, 1 stk.
Mkv. 1:20



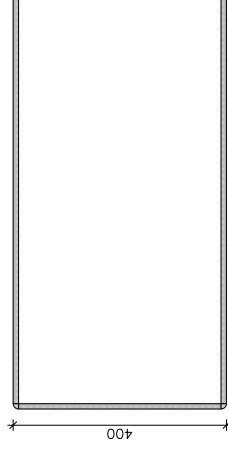
Nr. 13, 10mm stálplata, 1 stk.
Mkv. 1:20



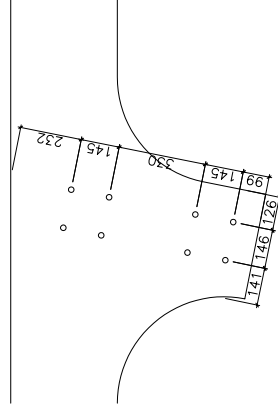
D Snið
10 13 Mkv. 1:5



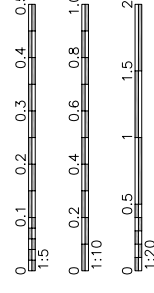
E Snið
10 13 Mkv. 1:5



F Snið
10 13 Mkv. 1:5



1 Deili
12 13 Mkv. 1:10



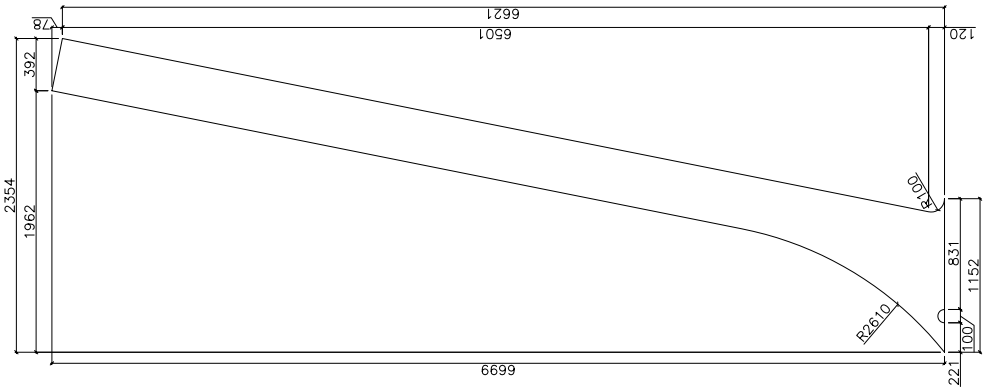
Smekkuþ mynd
smækun 50%

Wör	Stærð	Stærð	Stærð	Stærð	Stærð	Stærð	Stærð	Stærð	Stærð
Wör	03-137	AutoCAD	Handrit	1:5	1:10	1:20	1:50	1:100	1:200
Stærð	KA/BA	DB	DB	DB	DB	DB	DB	DB	DB
Stærð	DB	DB	DB	DB	DB	DB	DB	DB	DB
Stærð	DB	DB	DB	DB	DB	DB	DB	DB	DB
Stærð	DB	DB	DB	DB	DB	DB	DB	DB	DB
Stærð	DB	DB	DB	DB	DB	DB	DB	DB	DB

FJÖLHÖNNUN
FLOTTGÆTTI
VÉLFRÓÐA
Smi 525 5000 Fax 525 9300

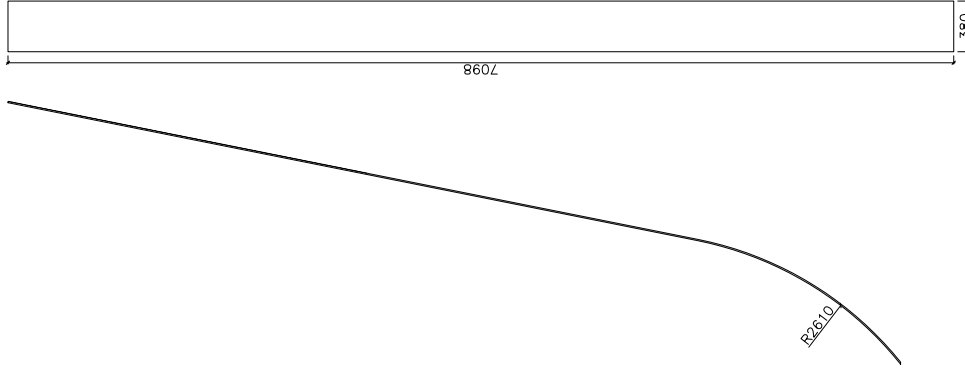
FLUGMALSTJÓRN ISLANDS
Flugmálstjórn Íslands
Hafnarstr. 15
101 Reykjavík

Aðflugsljós við Reykjavíkflugvöll
Stálsmstur
Form og útlit
Mstur 10
Útgáfa mánu.:
20.12.2004
Tímabil mánu.:
V-09-14.dag
Masta sk. V-09-10/5



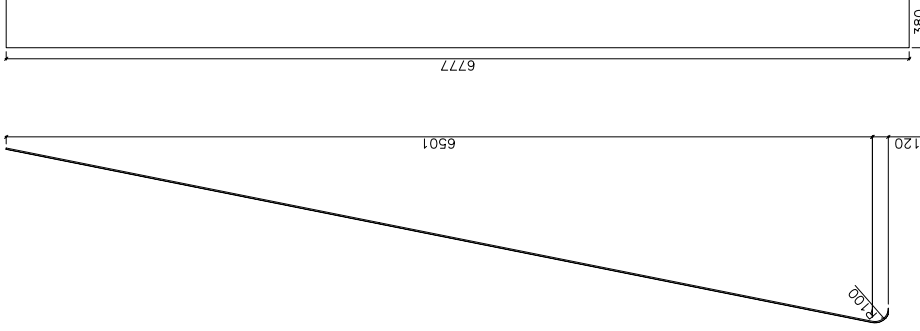
Nr. 15, 10mm stálpíata, 2 stk.
Mkv. 1:20

Snið 14 Mkv. 1:5



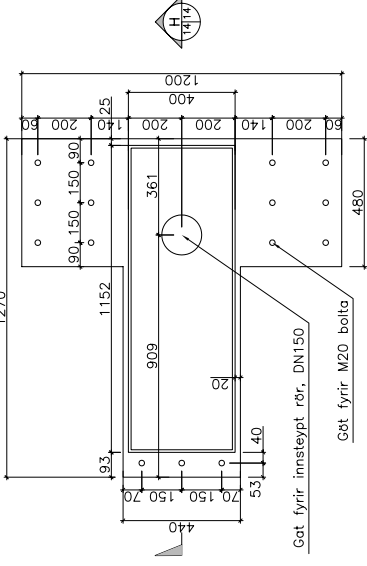
Nr. 16, 10mm stálpíata, 1 stk.
Mkv. 1:20

Snið 14 Mkv. 1:5

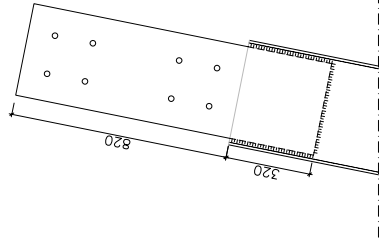


Nr. 17, 10mm stálpíata, 1 stk.
Mkv. 1:20

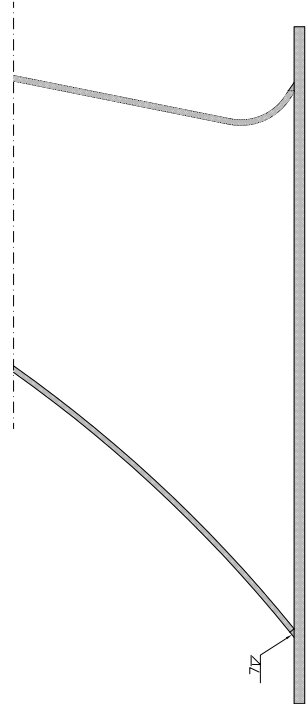
Snið 14 Mkv. 1:5



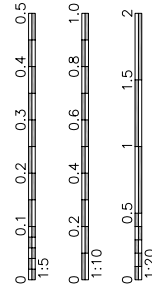
Nr. 14, undirstöður, 20mm stálpíata, 1 stk.
Mkv. 1:10



Snið 14 Mkv. 1:10



Snið 14 Mkv. 1:5



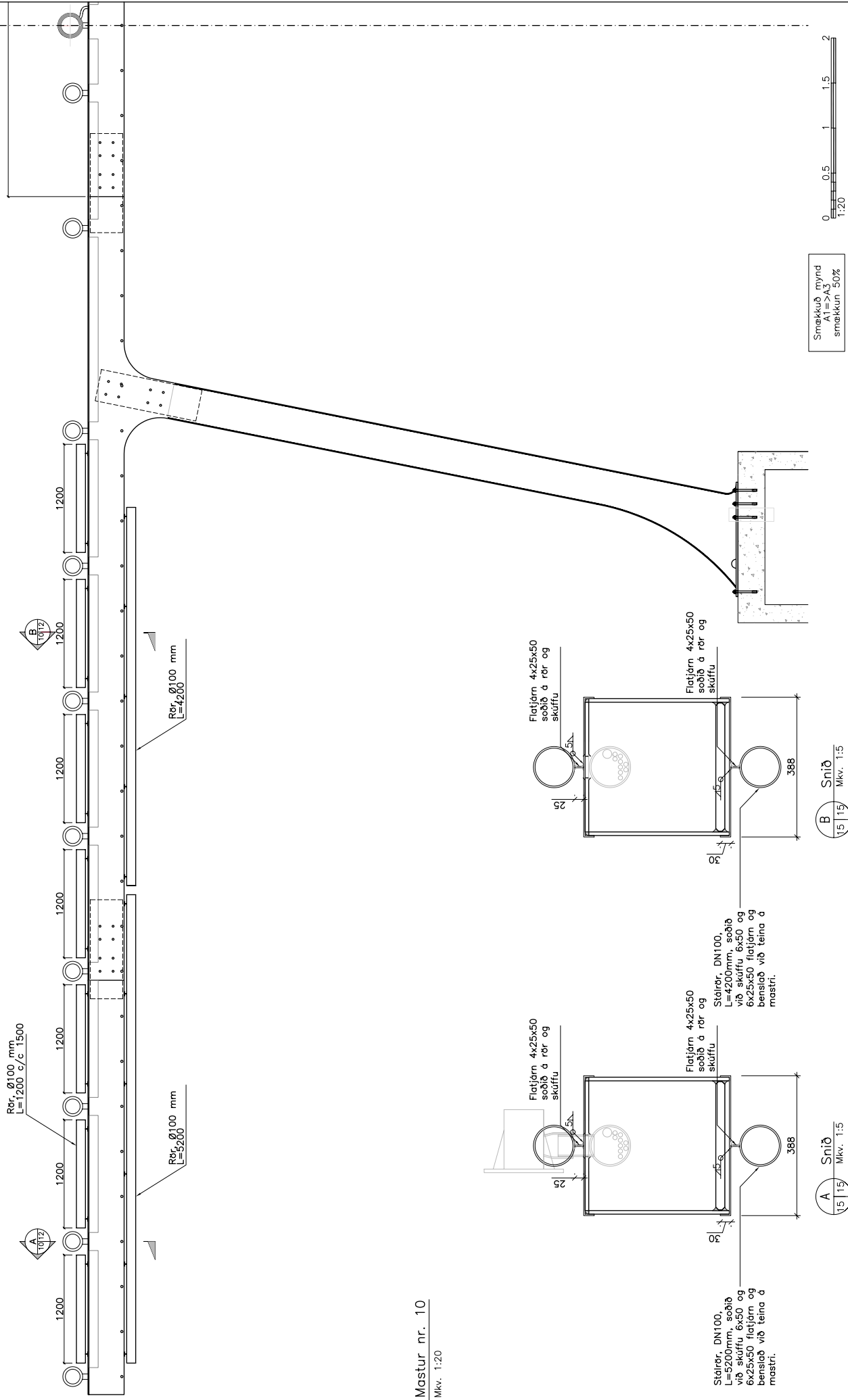
Smekkub mynd smækkun 50%

Wörk. númer	Wörk. nafn	Dagur	Stað
03-137	AutocAD		
KV/FA	DB		
Wörk. númer	Wörk. nafn	Dagur <td>Stað</td>	Stað



Wörk. númer	Wörk. nafn	Dagur <td>Stað </td>	Stað
15	Stálmestur		
	Form og úthitt		
	Mastur 10		
	Útgáfudagur	20.12.2004	
	Wörk. númer	V-09-14.dwg	
	Wörk. nafn	1:20	

Aðflugsljós við Reykjavíkflugvöll



Mastur nr. 10

Mkv. 1:20

Smekkub mynd
A1 => A3
smekkun 50%

Wörk: vélisgrá		Wörk: mynd
03-157		AUTOCAD
Wörk: vélisgrá	KV/BTA	DB/BTA
Wörk: vélisgrá	Þegar	Þegar
Smiðing: Snið		Þegar
Óp	15	15
Óp	15	15
Óp	15	15
Óp	15	15
Óp	15	15
Óp	15	15
Óp	15	15

FLUGMÁSTIÐRMI ÍSLANDS
Eskaniel: Örn Aronson Arnarson

FJÖLHÖNNUN
Staðhóla 27, 110 Reykjavík
Sími 525 0300 Fax 525 0388

Aðflugsljós við Reykjavíkurtúgvöll
Stálímstúr
Dempunaraðgerðir
Mastur 10

Stærð: 1:20
1:20/1:10
1:20/1:10